Energy Harvesting from Human Body, Motion and Surroundings

Ricardo Francisco Cruz Folgar

Dissertation submitted to the faculty of the Virginia Polytechnic Institute and State University in partial fulfillment of the requirements for the degree of

Doctor of Philosophy
In
Mechanical Engineering

Shashank Priya, Chair
Lei Zuo
Maury A. Nussbaum
Rolf Mueller
Alan T. Asbeck

July 24, 2019
Blacksburg, VA

Keywords: Energy Harvesting, Electromagnetic, Biomechanics, Wearable, Mobile, Piezoelectric, Resonance, Exoskeleton, Dual Harvester, Body Heat, Vibrations.

Energy Harvesting from Human Body, Motion and Surroundings

Ricardo Francisco Cruz Folgar

ABSTRACT

As human dependence on electronic devices grows, there is emerging need on finding sustainable power sources for low power electronics and sensors. One of the promising possibilities in this space is human body itself. Harvesting significant power from daily human activities will have transformative effect on wearables and implantables. One of the main challenges in harvesting mechanical energy from the human actions is to ensure that there is no effect on the body itself. For this reason, any intrusive mechanism will not have practical relevance. In this dissertation, novel non-intrusive energy harvesting technologies are investigated that can capture available energy from body, motion and surroundings.

Energy harvesting from body is explored by developing a wrist-based thermoelectric harvester that can operate at low temperature gradients. Energy harvesting from motion is investigated by creating a backpack and shoe sole. These devices passively store kinetic energy in a spring that is later released to a generator when it is not intrusive to the user kinematics. Lastly, energy harvesting from immediate surroundings is investigated by designing a two degree of freedom vibration absorber that is excited by electromagnetic fields found in common household appliances. These novel solutions are shown to provide consistent electrical power from wasted energy. Harvester design are extensively modeled and optimized device architectures are manufactured and tested to quantify the relevant parameters such as output voltage and power density.

Energy Harvesting from Human Body, Motion and Surroundings

Ricardo Francisco Cruz Folgar

GENERAL AUDIENCE ABSTRACT

Energy harvesting is the action to transform energy in the form of heat, relative motion, light, etc. into useful electrical energy. An example of an energy harvester is a solar cell which converts energy in the form of light to electricity. Our body consumes a considerable amount of energy to maintain our body temperature and achieve everyday movements, i.e., walking, jumping, etc. The purpose of this research was to fabricate, model and test wearable energy harvesters in the form of a backpack, a shoe sole, a watch, and a cantilever beam to charge mobile electronics on the go. Electrical energy is harvested from human motion by using the relative displacement between the human torso and a payload. Similarly, the ankle joint is used to produce electricity by using the relative rotation between the foot and shank. The difference in temperature between the ambient air and the human body is used to generate enough electricity to power a wrist watch. Finally, energy is harvested from everyday surroundings by using a cantilever beam which absorbs magnetic fields coming from power cords and able to power sensors.

ACKNOWLEDGEMENTS

First, I would like to thank my advisor Dr. Shashank Priya for giving me the opportunity to work with him, guide me and motivate me during my PhD work. Thanks for challenging me and giving me the freedom to pursue my research ideas.

I wish to thank Dr. Zuo, Dr. Nussbaum, Dr. Mueller and Dr. Asbeck for serving on my PhD committee, provide me with suggestions and valuable time to improve my work.

I also thank all of my colleagues, undergraduate researchers and staff in the CEHMS lab for their support and research collaborations. My friends in Blacksburg that I have met during my undergraduate and graduate studies. You all made me mentally reboot when I was stressed and overwhelmed.

I would like thank the financial support from the Mechanical Engineering Department at Virginia Tech, ICTAS, NSF I/UCRC, CERDEC and ARMDEC.

Finally, I wish to thank my parents, Ricardo Cruz Letona and Aracely Folgar, my sister Aida Cruz-Folgar, and my extended family which without their support I would not been here and able to accomplish my goals.

Gracias a todos!

TABLE OF CONTENTS

List of Figures

List of Tables

Chapter 1 Introduction

1.1 Definition of Energy Harvesting

Energy harvesting dates to windmills to mill grains or water wheels to utilize stream flow for grinding wood. An energy harvester converts freely available environmental energy (mechanical, thermal, magnetic, etc.) into useful electrical energy. This electrical energy could either be used immediately or stored in a battery to provide a constant energy output. Today, the internet of things (IoT) is driving the development of low power electronic devices that can operate for longer periods of time. All of these IoT devices currently rely on battery, however, in last several years battery energy density has saturated [1]. As a result of low power requirement and saturation in the performance of batteries, focus has shifted on developing energy harvesters that can enhance battery life or directly power devices.

Ideally the maximum amount of electrical energy that a harvester could harness is equal to the amount of the energy from a source. However, in practice, this conversion is much lower since multiple losses occur in a harvester (friction, heat, resistance, damping, etc.), as shown in the Figure 1.1.

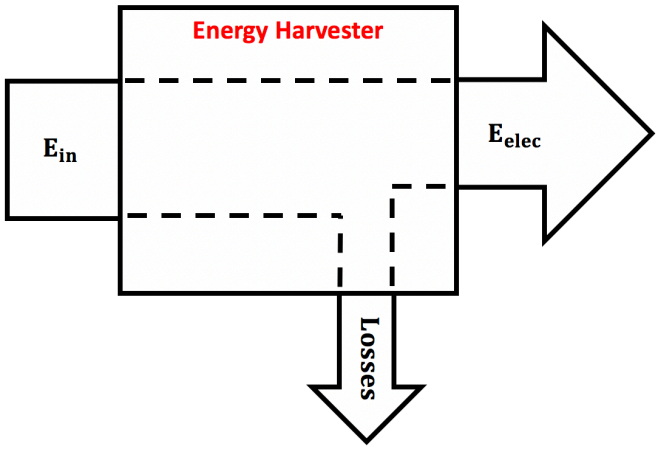

Figure 1.1- Representation of energy losses when engaging an energy harvesting system.

A simple representation of efficiency can be obtained by dividing the electrical energy output with the energy input as [2]:

$$\eta = \frac{E_{elec}}{E_{in}} \tag{1.1}$$

where η is efficiency and E is energy in Joules. This same formula can be applied to the electrical power generated, where the power input is given in Joules per second.

In order to maximize the output electrical power from an energy harvester, the maximum power theorem needs to be utilized. This theorem states that in order to obtain the maximum external power from a power source, the internal resistance of the source needs to be matched with an external resistance [2]. This theorem shows the condition for maximum power transfer and not the maximum efficiency, as shown in the electrical circuit in Figure 1.2.

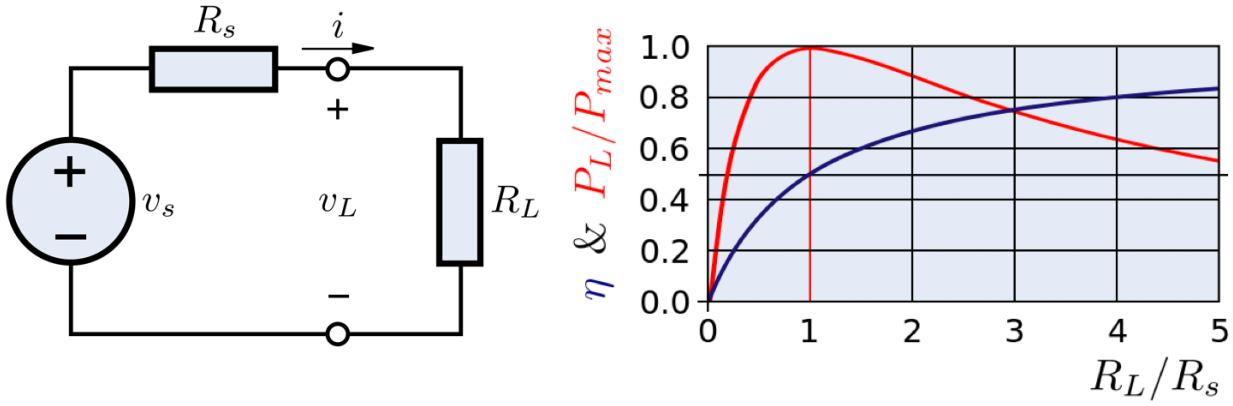

Figure 1.2- Efficiency and maximum power transfer as a function of ratio of load resistance to source resistance.

In Figure 1.2 the efficiency (η) is given by the ratio between output and input voltages as[2] :

$$\eta = \frac{V_L}{V_S} \tag{1.2}$$

where V_L is the load potential and V_s the source potential. The maximum power achieved in a system is obtained as [2]:

$$P_L = \frac{V_L^2}{R_L} \tag{1.3}$$

where R_L is the load resistance. The power generated from an energy harvester could be periodic or non-periodic; therefore, an average power is generally reported to provide fair comparison across multiple harvesters or multiple designs [3] :

$$P_{ave} = \frac{V_{RMS}^2}{R_L} \tag{1.4}$$

where V_{RMS} is the root mean square voltage. Other comparison metrics based on Eqn. 1.4 consists of dividing the average power over mass, volume, mass*volume or acceleration.

1.2 Overview of Energy Harvesting Techniques

Next, an overview of the basics of the energy harvesting systems is discussed to provide the underlying principles controlling the power generation.

1.2.1 Electromagnetic Induction

Electromagnetic induction is governed by Faraday's law of induction which states that any change in magnetic environment in a coil will induce an emf voltage in the coil, given as [3]:

$$V_{emf} = -N\frac{\Delta\Phi}{\Delta t} \tag{1.5}$$

where N is the number of turns in a wire, Φ is the magnetic flux through the wire (multiplication of the magnetic field B and a perpendicular area of the coil A), and *t* is time. Permanent magnet generators are built using Eqn. 1.5 by placing rotating magnets next to each other known as rotors between fixed coils or stators. Permanent magnet generators can be either radial or axial as shown in Figure 1.3.

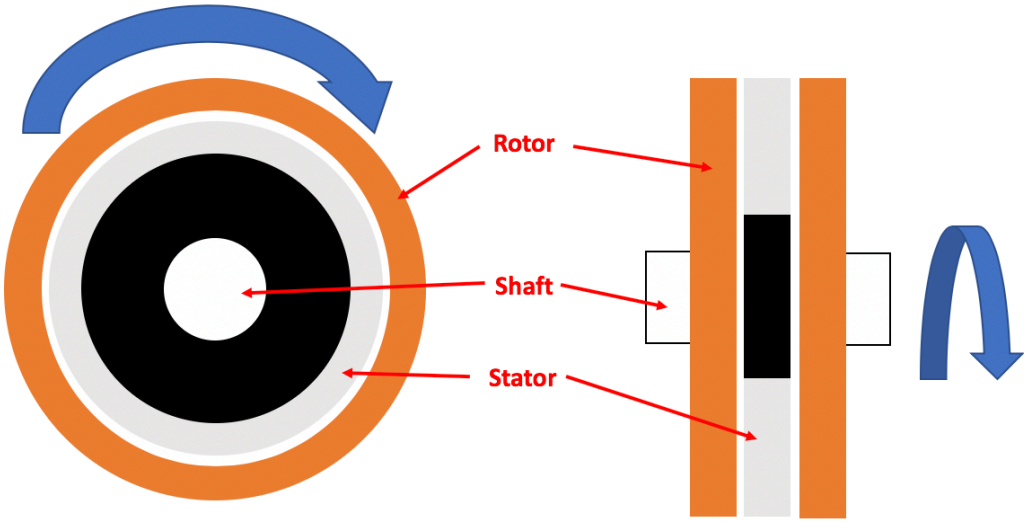

Figure 1.3- (Left) Radial permanent magnet generators. (Right) Axial permanent magnet generators.

Electrical power of a permanent magnet generator is governed by the equation [4]:

$$P = \frac{V_{emf}(t)^2}{R} \tag{1.6}$$

The maximum voltage of a permanent magnet generator can be calculated by simplifying Eqn. 1.6 [4]:

$$V_{max} = NB_{max}Aw_{max} \tag{1.7}$$

where w_{max} is the maximum angular velocity of the generator rotor. Using Eqn. 1.7 one can design for maximum voltage by maximizing each constant. However, when maximizing each of these constants one would have a bigger generator making it more intrusive for wearable applications.

The coils from the stator can either be connected in three phases where voltage waves overlap providing a more constant output or in a single phase consisting of a single voltage wave with a greater amplitude. The electrical voltage generated, either three phases or single phase, is often rectified to produce a unidirectional output. The resistance of the generator is matched to an external load to produce maximum power.

1.2.2 Piezoelectric Materials

Piezoelectric materials generate voltage when subjected to strain or vice-versa. In energy harvesting, piezoelectric materials are used to directly convert mechanical energy into electrical energy. There are two common modes commonly used for piezoelectric transducers: 31 mode and 33 mode. Piezoelectric transducers operating in 33 mode will generate voltage when compressed along the poling direction while the transducers operating in the 31 mode will generate voltage when compressed perpendicular to the poling direction. In a cantilever system, the piezoelectric transducer is operating in the 31 mode since a low thickness patch can be easily designed to be included on the high stress region.

1.3 Biomechanical Review and Terminology

Human walking consists of repetitive movements from two legs that provide both support and propulsion. The repetitive movements during walking are represented in an interval called the gait cycle as shown in Figure 1.4.

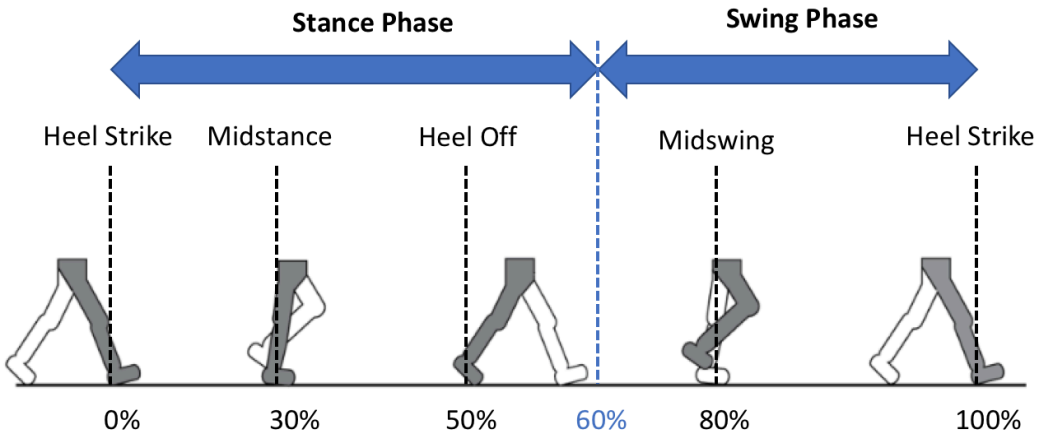

Figure 1.4- The gait cycle is divided into two phases: 1) the stance phase where the leading leg stays on the ground and 2) the swing phase when the leading leg is not touching the ground [5].

All the energy used during gait comes from nutrients in food. These nutrients power our musculoskeletal system providing the energy to move and perform physical activity. The mechanical power from a joint during human walking can be expressed with the formula [6]:

$$P = \tau * w \tag{1.8}$$

where P is mechanical power, τ is the net joint torque and w the joint angular velocity. One can also produce work during heel strike and the vertical COM fluctuation during walking. This can be calculated using the expression [6]:

$$P = F(v_f - v_i) \tag{1.9}$$

where F is the component of force along the direction of movement, v_i is the initial and v_f is the final velocity in the same direction. In order to properly compare energy from different subjects, Winter et al. [7] calculated the energy required during a single step and normalized it to subjects total weight as:

$$\frac{Work}{step} = total\ weight * [(phase_1 + \ldots + phase_n)] \tag{1.10}$$

where different phases during gait are based on negative and positive work performed at each joint in J/kg.

To estimate the amount of energy used during walking, the metabolic capacity of an individual is measured by finding the rate of O_2 consumption. In a lab setup, this is done by using a face mask on a subject which measures the volume and gas concentration of inspired and expired air [8]. To determine if an energy harvesting mechanism creates more power than the it consumes, Donelan et al. [9] defines the cost of harvesting as

$$COH = \frac{\Delta metabolic\ power}{\Delta electrical\ power} \tag{1.11}$$

where Δ*metabolic power* is the difference between the metabolic power of walking while generating electrical energy and walking without generating electrical energy, and $\Delta electrical\ power$ is the electrical power produced by the energy harvester.

1.4 Coupled, Semi-decoupled and Decoupled Energy Harvesters

A major component of Chapter 2 and 3 are the terminology coupled, semi-decoupled and decoupled energy harvesters. A coupled system is one that is bidirectionally connected, as a result, a person experiences the damping forces from an electromagnetic generator from all movements. A rack and pinion system connected to a generator is example of coupled system since damping from a generator will affect the dynamics of the system. A semi-decoupled energy harvester is a unidirectional harvester which generates power in one direction and is decoupled in the other by using a clutch bearing.

Chapter 2 and 3 focus on decoupled energy harvesters where input motion is not directly connected to generator when producing electrical power. These chapters demonstrate a solution for decoupling generator by first storing the input mechanical power in a spring and later releasing that mechanical power to a generator. In other words, an input rack winds a torsional spring and it only feels the stiffness and small damping forces coming from the spring. Later, the torsional spring releases the stored power to the generator without the user interference. As a result, one could potentially generate electrical power without increasing metabolic rate.

Figure 1.5 depicts different technologies that help in generating electric power and decreasing metabolic rate. The four quadrants in this figure represent: Undesirable, Harvesters, Decoupled Harvesters and Exoskeletons. The Undesirable quadrant consists of designs that consume power and increase metabolic rate. This would not be relevant for wearable applications. The second quadrant consists of all the Harvesters which can produce electrical power from human gait including rack and pinion, negative work, and smart materials harvesters. The fourth quadrant termed as Exoskeletons comprises of devices that help subjects in decreasing the metabolic rate including passive, quasi-passive and active exoskeletons. Finally,

the third quadrant presents the appropriate design for a biomechanical energy harvester since these devices would generate power while decreasing metabolic rate. In this dissertation, the decoupled harvesters are developed inspired by passive exoskeletons. These decoupled harvesters use springs as actuators and only harvest during negative work motions.

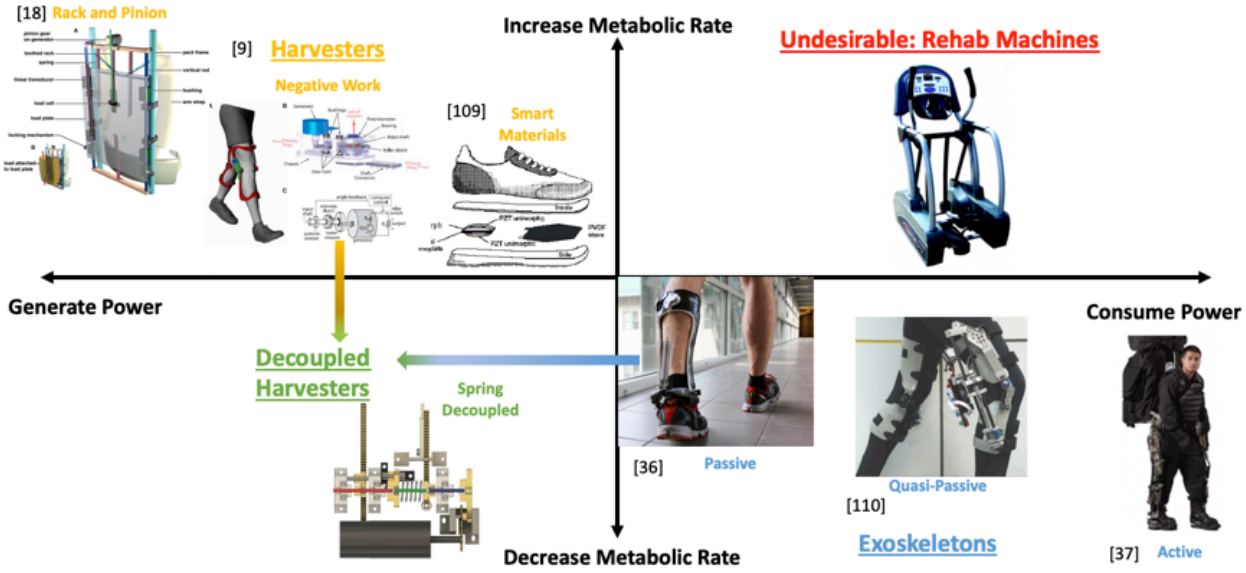

Figure 1.5- Metabolic Power vs. Electrical Power plot showing different technologies in each quadrant.

A more detailed explanation of the decoupled harvesters developed in this dissertation are presented in Chapter 2 on backpack energy harvester and Chapter 3 on shoe sole energy harvester.

1.5 Categorization of Energy Harvesting Technologies

In this dissertation, wearable energy harvesters are categorized into three different groups: energy harvesting from body, body motion and general surroundings.

1.5.1 Energy Harvesting from Body

Body energy harvesters are devices that harness energy from a static posture. These sources of energy include: body heat, blood pressure, exhalation, etc. The energy available from these devices can be enhanced by motion; however, movement is not needed to produce power.

For example, a thermal electric generator (TEG) produces electrical power from the difference in temperature between skin and ambient temperature. The electrical power produced will increase during motion since the TEG cold side temperature will be affected by external cooling.

1.5.2 Energy Harvesting from Motion

Motion energy harvesters harness energy from natural locomotion and body movements. Examples of energy sources from natural gait are joint rotation, heel strike, vertical motion movement, etc. When designing these devices, one needs to consider how intrusive a mechanism will be to the user; in other words, how it will affect their metabolic rate and walking patterns.

1.5.3 Energy Harvesting from Surroundings

These devices can harness energy from the immediate ambient. Most of the renewable energy generation can be placed in this category if modified for portability. For example, photovoltaic, wind turbines, etc. Other sources of energy in surroundings relevant for wearable applications are external vibrations, heat source and electromagnetic fields.

1.6 Dissertation Structure

Chapter 2 describes the design and development of a suspended backpack with decoupled energy harvester. This chapter discusses the benefits of decoupling the backpack compared to a semi-decoupled rack and pinion system. In addition, this chapter presents a new graphical representation for backpack energy harvesters.

Using a similar concept as that for the decoupled backpack in Chapter 2, design and development of a decoupled shoe sole energy harvester is presented in Chapter 3. The shoe energy harvester stores mechanical energy in the negative work timeframe of the gait and releases this energy during heel off.

In Chapter 4, a hybrid energy harvester is described that harnesses energy from the temperature difference between body and ambient. The harvester can also harness energy from arm swing motion. The harvester is enclosed in a wrist-watch like wearable electronic and uses combination of thermoelectric, thermomagnetic and piezoelectric technologies to capture the thermal and mechanical energy. The thermoelectric and thermomagnetic system is evaluated and optimized to provide high power density at low and high temperature differentials.

In Chapter 5, a magnetic field energy harvester is designed, modeled and fabricated to harvest power from high magnetic field sources, for example, powerlines and appliances. The novel design consists of a two degree of freedom system where isolation occurs in the secondary mass while maximum displacement occurs in the primary mass. The power generated is used to charge a drone battery and power sensors. Lastly, Chapter 6 summarizes the main findings in this dissertation and future work.

Chapter 2 Powering Mobile Devices Using a Decoupled Backpack Energy Harvester

2.1 Introduction

As soldiers become more dependent on advanced electronic devices, the weight carried by them continues to increase as they must carry the gadgets and external batteries. On average modern soldier carries around 100 pounds of equipment on a 72-hour mission, of which 16 pounds are batteries [10]. If a portion of this battery weight could be eliminated, soldiers would require less energy moving the equipment; therefore, making them less fatigued and more agile.

The strategies to harvest energy from human locomotion include heel strike, joint rotation and center of mass (COM) motion. To date, most of the biomechanical energy harvesters fail to address the effect of the harvester on the wearer. As a result, these coupled harvesters are not better than ordinary devices such as hand crank or peddle power generators.

Energy can be harvested due to the fluctuation of the body's COM, whose amplitude is approximately 5 cm [11] relative to an external mass or backpack. It is of major importance to notice that COM vertical displacement during gait cycle is highly dependent on walking speed and kinematics. According to Orendurff et al. [12], COM vertical displacement seen in their subjects changed from 2.74± 0.52 cm at 0.7 m/s to 4.83± 0.92 cm at 1.6 m/s. Gard et al. [13] concluded from their model that vertical motion of body comes from the foot roll-over shape, leg geometry (i.e. length) and step length. Another significant observation is that maximum relative displacement between a suspended backpack frame and body COM will be highly dependent on the spring used in the suspended frame as discussed in the next subsections. This chapter describes the suspended backpack mechanism including the combination that is needed to reach isolation. A decoupled energy harvester is modeled, built and compared to a semi-decoupled

harvester. The decoupled energy harvester showed 35% decrease in power generation while demonstrating an efficiency of 28% when compared to semi-decoupled harvester.

2.2 Review of Prior Backpack Harvester Technologies

A backpack energy harvester can comprise of two different technologies: 1) a suspended backpack frame that creates relative motion between a person's COM and oscillating mass and 2) an energy harvester which generates electrical power from the relative motion. The following subsections discuss the state-of-the-art suspended and energy harvesting backpacks.

2.2.1 Suspended Backpack Frame

While wearing a backpack at normal walking speed, a person's joints experience two external loads: 1) a static force or the dead weight of the backpack and 2) a dynamic or accelerative load caused by a person's COM vertical fluctuation. A representation of these forces is shown in Figure 2.1.

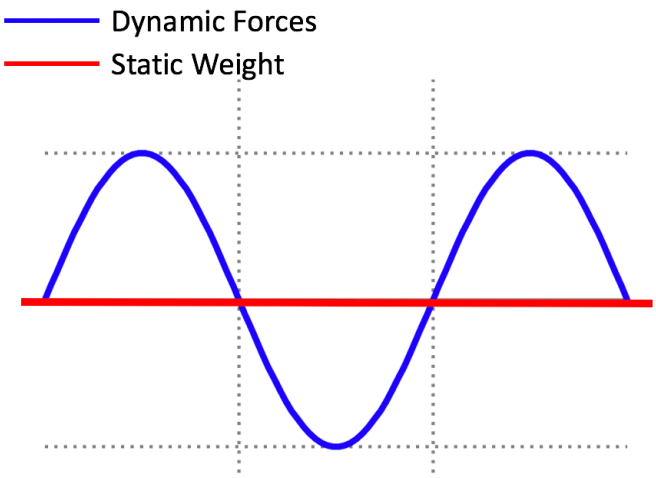

Figure 2.1- Simple representation of static and dynamic forces in a locked backpack.

Rome et al.[14] discovered that when suspending a bag on bungee cords the dynamic forces from wearing a backpack could decrease by 82% in peak accelerative condition. The accelerative forces are mainly reduced because the amount of displacement of the payload

relative to the frame is similar in magnitude and 180 degrees out of phase with the frame displacement relative to the ground. As a result, the researchers concluded that the metabolic rate was reduced by 6.2%. In other words, walking with a 27 kg backpack with a suspended frame would be equivalent to walking with a 21.7 kg locked backpack. Inspired by Rome et al.[14] study, several other interesting studies have been conducted on designing backpack harvester that results in reduction of metabolic rate ([15],[16],[17]).

2.2.2 Backpack Harvesters

Rome et al.[14] have shown that a suspended backpack could be an excellent mechanism to convert mechanical power to electrical power by using a generator with a pinion on the main frame and rack on the suspended frame [18]. From this study, the researchers concluded that as walking speed and payload increases the generated electrical power also increases. These findings demonstrate that electrical power is directly proportional to walking speed and payload. However, in this study the metabolic rate also increased when wearing the backpack energy harvester. This implies that after adding a conventional rack and pinion harvester the dynamics of the suspended system changed. As a result, multiple researchers have been focusing on decreasing the metabolic rate while harvesting higher power by reducing friction and damping. Efforts have also been placed on integration of different generators required to improve upon the prior state-of-the-art average power of 5.6 W at 5.6 km/hr with a 38 kg payload [18].

Yuan et al. [19] created a backpack energy harvester that generated an average power of 4.8 W at 5.6 km/hr with a 15 kg payload. They used a mechanical motion rectifier that incorporates a rack gear and a one-way clutch to convert bi-directional motion to a unidirectional rotation. Xie et al. [20] created an electromagnetic harvester based backpack which generated an

average power of 4.1 W at 5.6 km/h with a 15 kg load. Both these harvesters ([19], [20]) produce higher power density (W/kg) compared to the previously reported results.

Backpack harvesters using different harvesting technologies produce less power when compared to electromagnetic harvesters. Granstrom et al. [21] developed a backpack energy harvester by mounting flexible PVDF material in the shoulder straps of a backpack. They were able to harvest about 9.1 mW electrical power with a PVDF weight of 0.0035 kg. Feenstra et al. [22] developed a mechanically amplified PZT material which was integrated in a backpack shoulder strap and was found to generate an average power of 0.15 mW with a weight of 0.3 kg. Yang et al. [23], created a unique system where energy was harvested through triboelectric effects that generated a maximum power of 1.17 W with a total weight of 2 kg.

Another technology capable of generating power by the COM movement and does not require a user to wear a backpack is through electromagnetic induction. A common example is the work done by Saha et al. [24] where an induction generator comprised of two stationary magnets and two moving magnets housed in a tube and a coil generated an average of 2.5 mW from human body motion.

2.3 Mechanism Description

As noted in the above section, coupled energy harvesting mechanism comprising of a rack and pinion that is connected to a DC generator is normally utilized to maximize generated power. Other technologies such as piezoelectric, triboelectric and electromagnetic induction generate significantly lower power. However, coupled rack and pinion mechanisms are intrusive to human gait while smart material technologies have lesser impact on the wearer.

Regardless of the technology to harvest energy from human body, the effect on the human gait and kinematics should be the main priority. Section 2.3 explains how to design a

suspended backpack that is more comfortable for a user by developing the idea of a decoupled harvester. The design considers optimizing decoupled backpack energy harvester such that it can generate power with the same efficiency when compared to a semi-decoupled system. The three different configurations of a backpack energy harvester are shown in Figure 2.2.

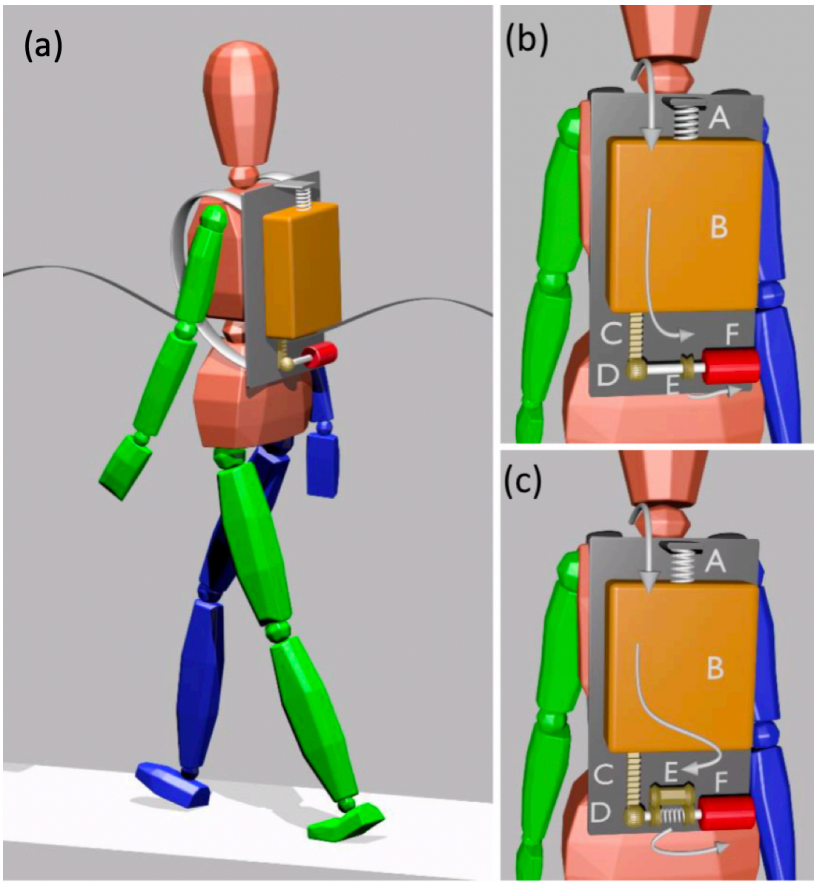

Figure 2.2- (a) A typical position during the gait cycle. The image shows the path traced by the center of mass of the body during walking. The pack mass and generator are connected by a rack and pinion therefore generating power in up and down movements. (b) The schematic of a semi-decoupled backpack harvester with a clutch bearing at E. The system only generates power during the downward movement of the backpack. (c) The schematic of a decoupled harvester with a locking and unlocking mechanism at E. The arrows indicate the direction of power flow.

2.3.1 Suspended Backpack

Suspension and comfortability to the user are two important parameters in design of human backpack harvester since there are both physiological and psychological concerns that

could potentially increase metabolic rate. A common suspended backpack system comprises of four different parts, as shown in Figure 2.3.

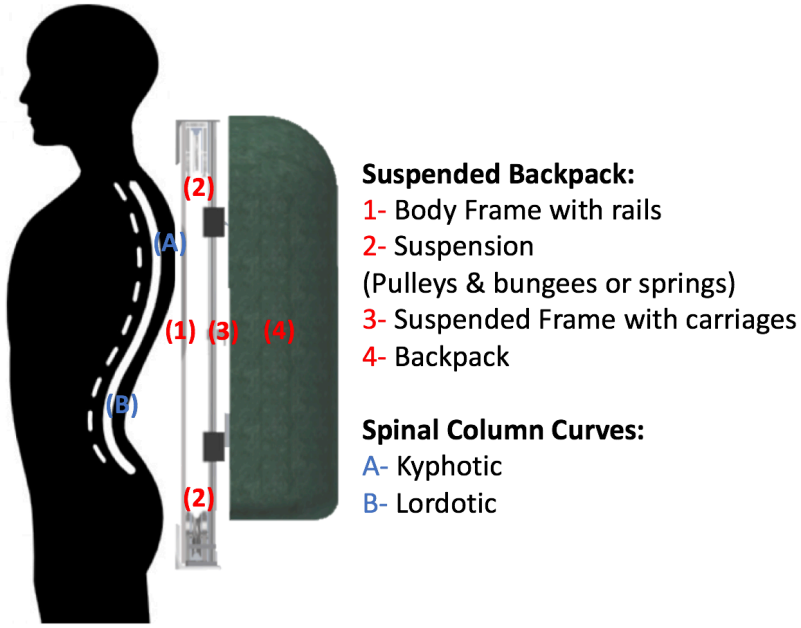

Figure 2.3- Parts of a suspended backpack and curves in the spinal column.

As shown in Figure 2.3, a usual suspended backpack is not the most convenient structure for user since the body frame does not adjust to its S-shaped vertebral column. As a result, the suspended payload is further away from the human center of mass and amplifies the moments created by the static and dynamic forces of the payload. This will also generate a change in the body posture of the wearer. In other words, a subject will flex his/her torso to compensate the greater moment generated by the backpack. Thus, a suspended backpack was designed in order to first model the dynamics presented by Rome et al. [14] and then use the model to create a more comfortable backpack that decreases the moment generated by the load, as shown in Figure 2.4.

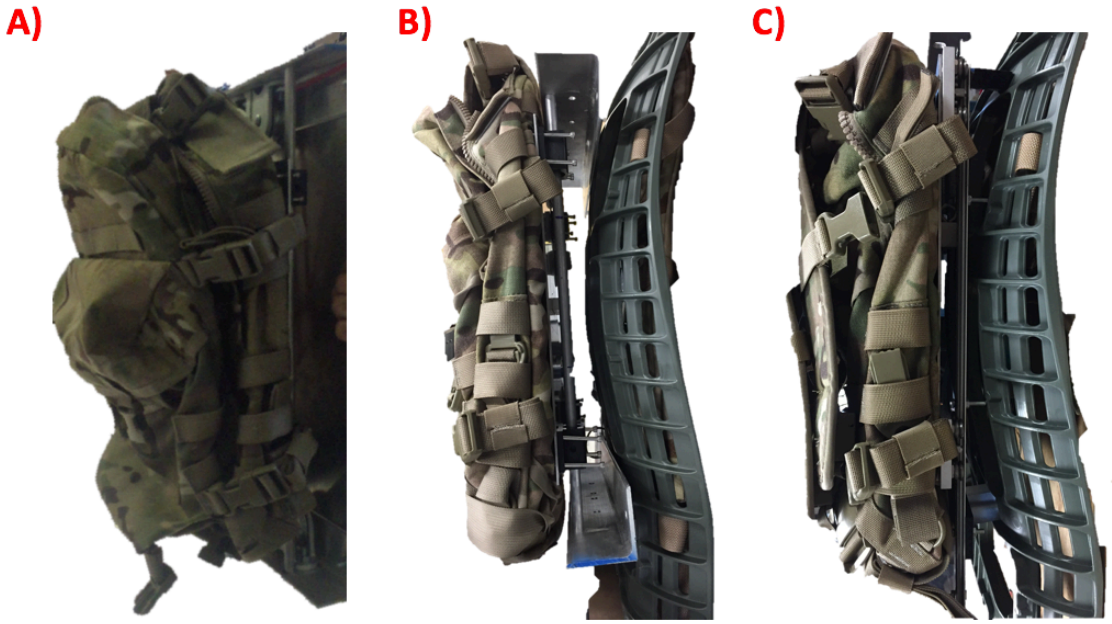

Figure 2.4- A) First iteration of the suspended backpack. B) Ergonomic backpack with belt adjustments. C) Closer to COM suspended backpack.

Figure 2.4A shows the first iteration of the suspended backpack where distance between body plate and suspended frame is sliding on aluminum tubes and four linear bearings. Figure 2.4B is the second iteration that comprises of the same sliding system but the body plate is changed to a frame that fitted the human spinal column. The nature of the spinal cord led the kyphotic curves of the column create distance between backpack plate and body frame of 1.8 in. while the lordotic had a distance of 2.5 in. This implies that closest one could get to the body COM while not disturbing the linear motion of the backpack is when the backpack frame is mounted on top of the kyphotic curve. For this reason, in Figure 2.4C, the sliding system was changed to carriages with guide rails which were attached as close as possible to the body frame, and as a result, the distance changed to 1.2 in. and 1.8 in. The components used to produce the frame, as shown in Figure 2.4C, are listed in Table 2.1.

Table 2.1- Major components of the suspended backpack are shown in Figure 2.3C.

No. of Items	Major Item Description
1	Springs (stiffness according to load)
1	US Army Backpack
2	Steel Guide Rails (McMaster Carr: 9374T4)
2	Support Rails (McMaster Carr: 9374T5)
4	Roller Carriage (McMaster Carr: 9374T1)
1	Molle II Rucksack Frame
1	Molle II Enhanced Shoulder Straps
1	Aluminum Plate
1	1x1-in. L-Bracket

2.3.1.1 Benchtop experimental system

Gait variability between each stride have been discussed in literature ([25],[26]). Prior research has shown that different subjects have preferable walking stride amplitude and frequency. When walking in their preferable gait cycle, cadence muscles activate differently from stride-to-stride as shown by muscle activation measurements conducted using surface electromyography (EMG) [25]. In order to properly model the vibration dynamics of a suspended backpack one needs to evaluate it while isolated from the human body. Therefore, a small benchtop suspended backpack was built and tested on a long stroke shaker (APS 113) as shown in Figure 2.5.

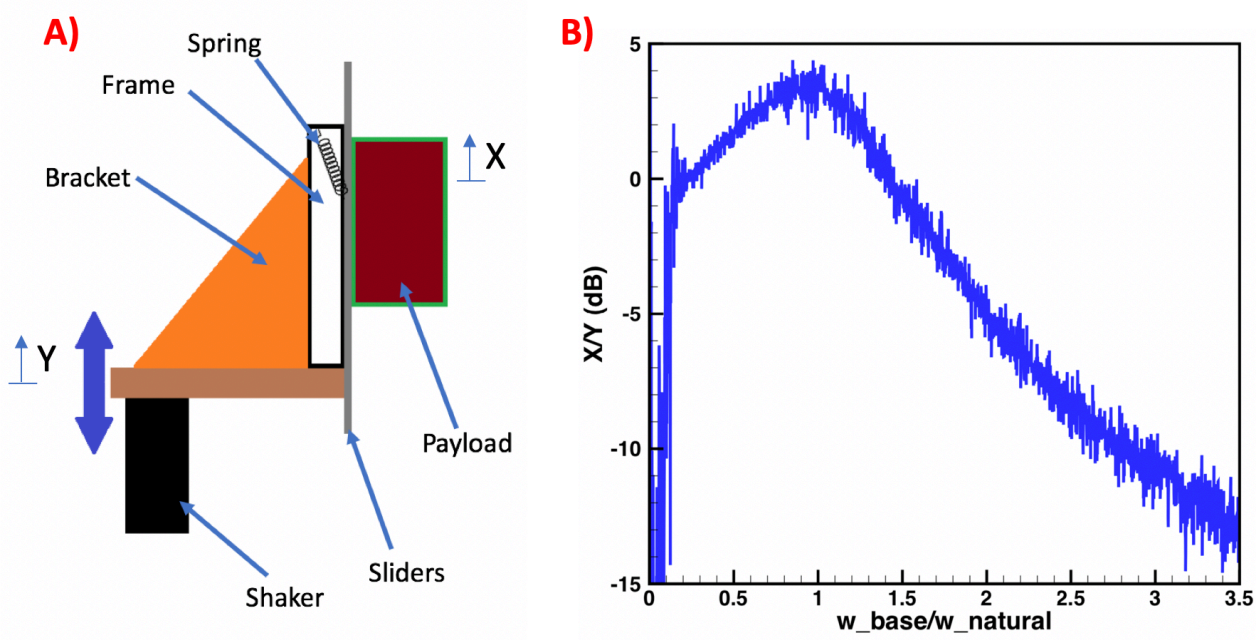

Figure 2.5- A) Schematic of small-scale suspended backpack. B) Plot describing normalized displacement vs. frequency.

Figure 2.5B shows the plot between the relative displacement of the shaker and payload vs. the ratio of the frequency of base excitation and natural frequency of the system. From this plot one can conclude that the suspended backpack system behaves as a one degree of freedom (DOF) system commonly known as a base excitation system.

2.3.1.2 Suspended Backpack Walking Model

It is well-expected observation in biomechanical field that human walking can be simply represented through an inverted pendulum model ([27], [28]). However, this model does not present the GRFs experience during the gait cycle but it provides a closed waveform of the displacement produced by the body COM.

To properly display GRFs, Adamczyk et al. [29] and Whittington et al. [30] have shown experimentally and theoretically that human GRF can be properly identified when introducing a rolling foot. As a result, the walking model is based on the inverted pendulum approach in combination with a rolling foot. Force and leg length profile are also incorporated in the model

to generate the desired heel strike, toe-off GRFs and COM displacement that results in a smoothened absolute sine wave comparable to the anthropomorphic COM vertical displacement. The vibrational system is governed by the equation of motion given as [31]:

$$m\ddot{x} + c(\dot{x} - \dot{y}) + k(x - y) = 0 \tag{2.1}$$

where y(t) is the input displacement from the COM of the human. A simple representation of a base excitation is shown in Figure 2.6 where each line *z* represents damping ratio [31]:

$$z = \zeta = \frac{c}{c_{critical}} = \frac{c}{2\sqrt{km}} \tag{2.2}$$

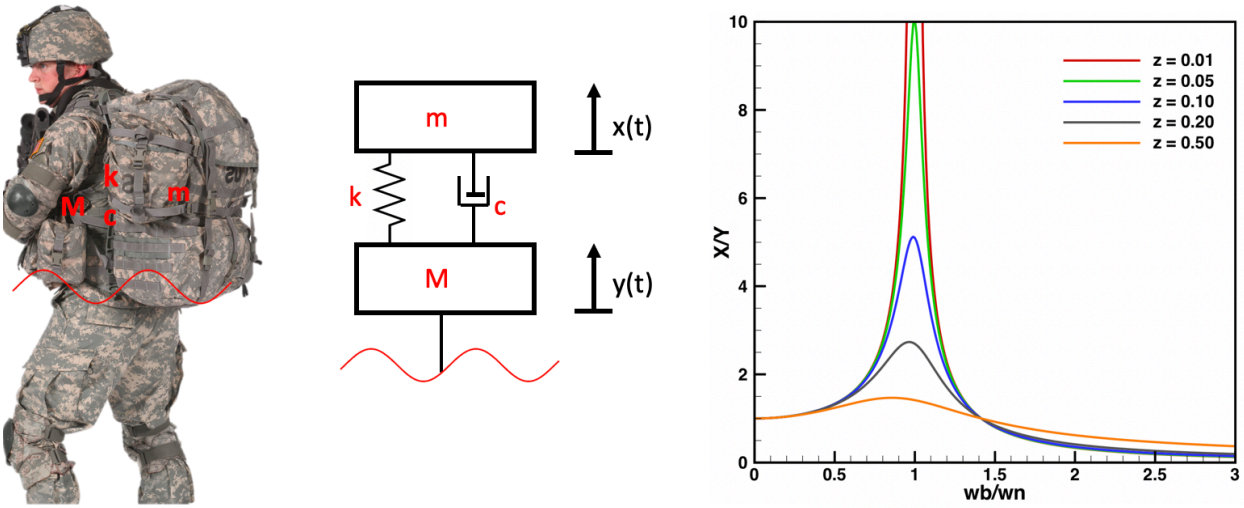

Figure 2.6- Representation of the base excitation model with a human soldier and displacement areas of interest. When wb/wn is greater than $\sqrt{2}$ the bag will reach the isolation region.

With this model, the concept of isolating the backpack motion from the body frame by using springs/bungee cords suspension can be verified. An optimal natural frequency could make walking easier by reducing the dynamic load that is experienced. Three different scenarios of the model representing different backpack displacement are shown in Figure 2.7.

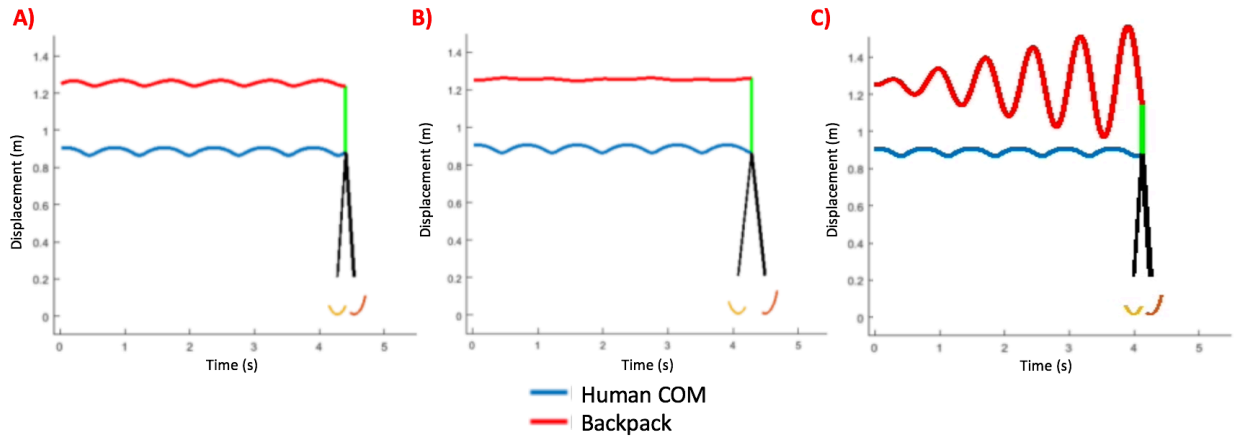

Figure 2.7- A) Model of human walking with a locked backpack, B) isolated backpack and C) backpack under resonance.

From the suspension, the effective ground reaction forces for a locked backpack and an isolated backpack can be calculated. Y-axis in Figure 2.8 shows non-normalized force which includes static and dynamic forces from the weight of the person and backpack. GRFs were calculated using the position of the bag with respect to the angle of the foot and hip.

$$GRF = [(m_b * g) - (\Delta s_i + k * (s_i - (y_b - y_h)) - c * \dot{y_b}] * \sin\left(cos^{-1}\left(\frac{x_f - x_h}{L}\right)\right) \quad (2.3)$$

where Δs_i is the initial spring displacement, k is the spring constant, s_i is the length of the spring, y_b is the vertical position of the bag, y_b is vertical position of the leg, y_h is the vertical position of the hip, c is the damping coefficient, x_f is the position of the foot, x_h is the position of the hip and L is the leg length. Figure 2.8 reveals that a smaller spike in force value at heel strike could be achieved when isolating a suspended backpack.

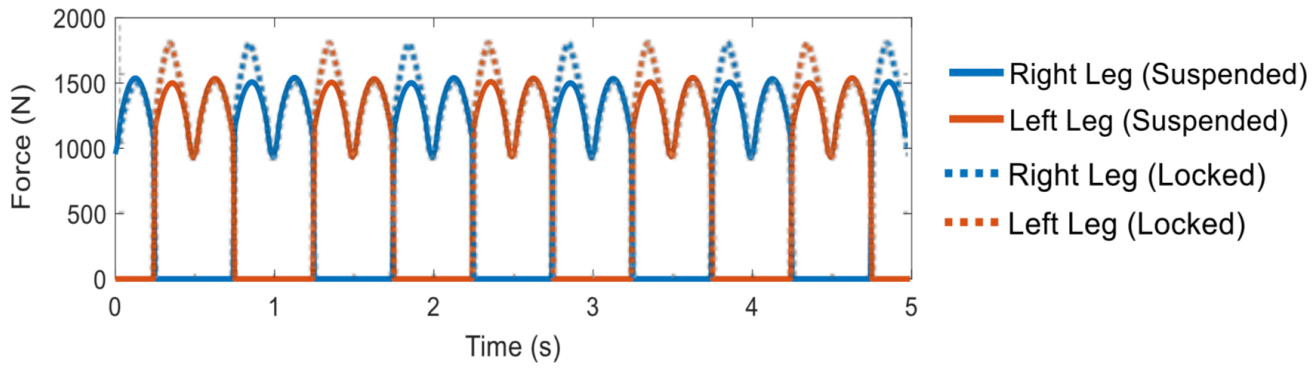

Figure 2.8- Modeling comparison of GRFs of an isolated, suspended and locked backpack mechanisms.

Lastly, the model shows that there are two factors which needs to be considered when selecting a stiffness for a suspended backpack: 1) the desired stiffness needs to mitigate oscillations and 2) the initial rest extension of the spring. This results in a balancing act between the two paraments, as low stiffness would reduce oscillation but backpack would be hanging down too low from the COM, as shown in Figure 2.9.

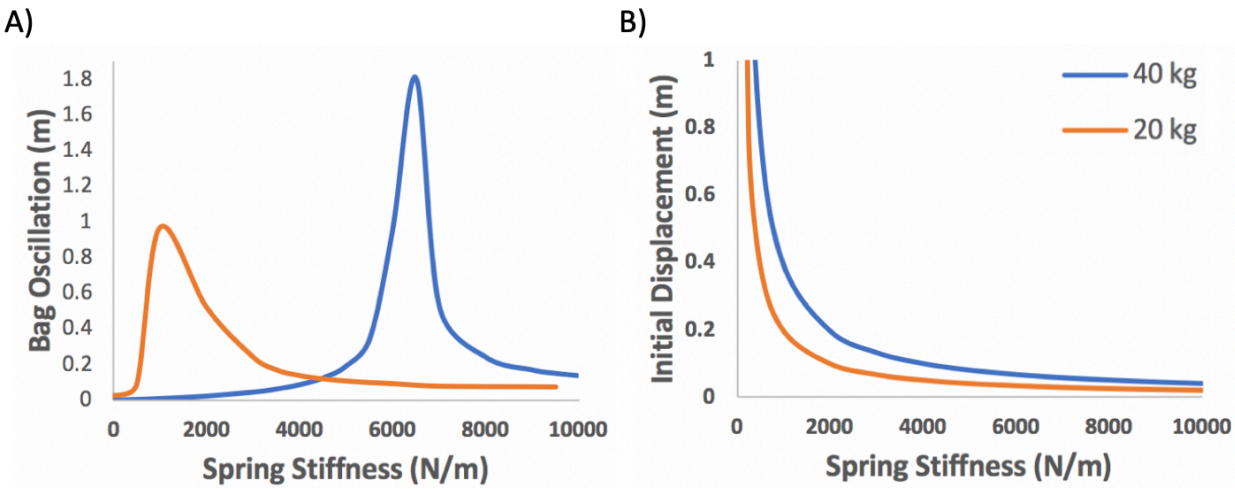

Figure 2.9- A) Dynamic oscillation of backpack vs. stiffness. B) Initial static spring displacement vs spring stiffness.

Further, if mass of the backpack is lowered then the resonance peak shown in Figure 2.9A will move to the left of the plot. When walking frequency (input frequency) changes from 1

Hz to 1.5 Hz, the resonance displacement amplitude decreases. As a result, in order for a suspended backpack to completely mitigate dynamic forces, spring stiffness needs to be adjusted according to the walking frequency of a person and change in mass of the payload.

2.3.2 Design Strategy for a Decoupled Backpack Harvester

A decoupled backpack harvester system behaves as a suspended backpack by mitigating dynamic forces while generating electrical power from relative motion. To achieve this condition, a spring is used as a mechanical energy storage mechanism. The stored energy is released to a generator at a later time where it will not be intrusive to the wearer. A representation of a spring decoupled mechanism is shown in Figure 2.10.

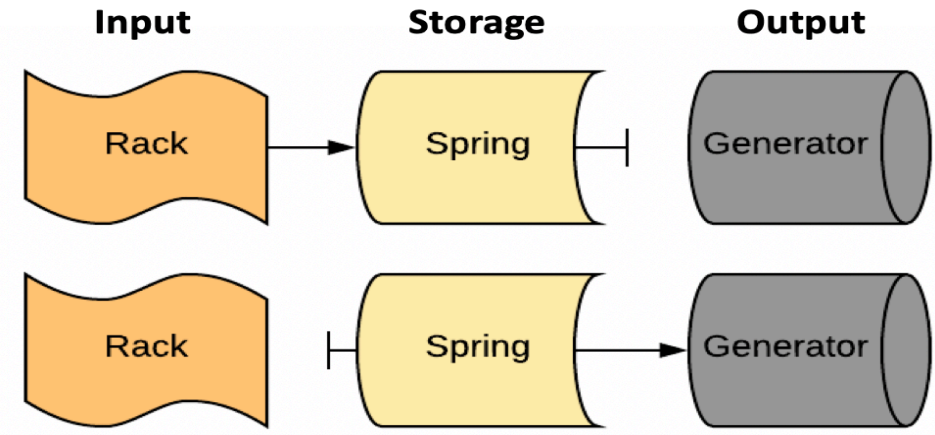

Figure 2.10- The first row represents the step when the energy harvester stores the energy in a mechanical spring while the second row represents the time when the spring unwinds to the generator while disconnecting the input.

To accomplish the system shown in Figure 2.10, one needs to first disconnect the storage spring from releasing to generator while the input rack stores the energy passively to the torsional spring. This is accomplished by using a one-way clutch from the rack to the spring and a locking lever mechanism which holds the spring from immediately releasing. In the second

row, the one-way clutch will disconnect the rack from the spring while a locking lever will open and release the stored energy to the generator.

2.3.3 Optimized Decoupled Mechanism

The decoupled energy harvester comprises of clutches, locking and unlocking mechanism, gearbox and a generator as shown in Figure 2.11. The rack is fixed to the suspended backpack and oscillates with the backpack. During a downward stroke, the locking rack locks onto clutch C while clutch A winds the torsional spring. During an upward stroke, clutch A freewheels while clutch B prevents the torsional spring from winding back to the input. Towards the end of the upward stroke, the unlocking lever opens the locking rack, thereby channeling the stored torque to the generator through a gearbox. The gearbox enhances the angular rotation of the generator and hence inducing the emf voltage. A semi-decoupled harvester, on the other hand, consists of similar arrangement except that the torsional spring, and locking and unlocking mechanism are not present.

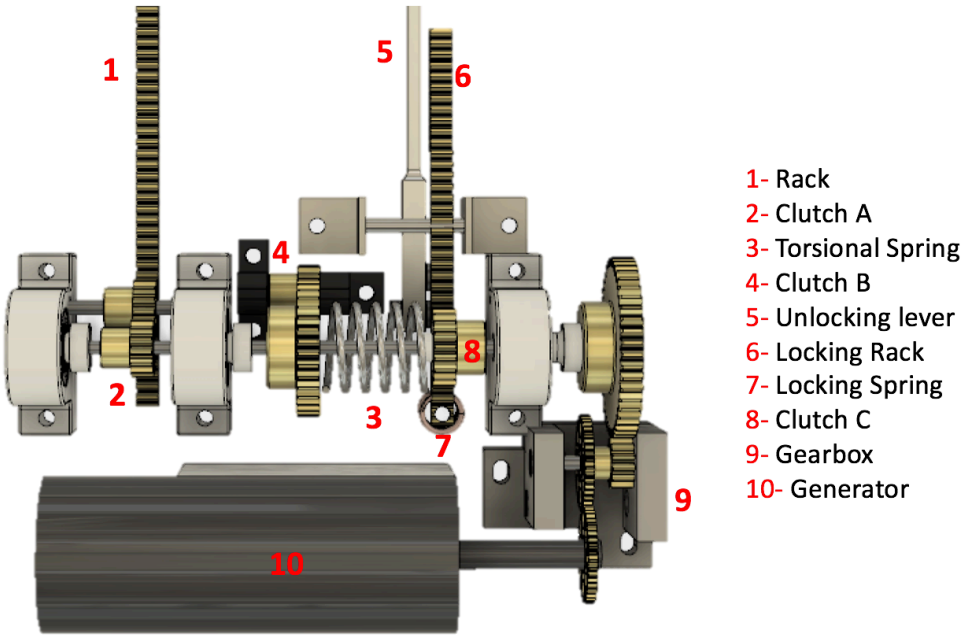

Figure 2.11- Top view of decoupled backpack harvester.

The decoupled system shown in Figure 2.11 utilizes the torsional spring and the locking mechanism shown in Figure 2.12 to provide decoupling. For the system to work properly, the disengaging roller is optimally placed under the rack pivot which depends on the initial static displacement of the backpack. The spring and length of the rack was calculated so that it could properly hold the torque of the torsional spring while at the same time it would be easy to release. As the slider goes down the torsional spring, winding occurs. As the slider goes up, the locking rack is moved against the spring therefore releasing the mechanical energy stored in the torsional spring. In case, an upward movement does not release the energy, the torsional spring will keep on winding and the slider will have a second chance to release during the upward stroke. If this still does not release the torsional spring, the bag will stop moving downwards since it cannot go against the torsional spring force and will only move in the upward stroke in order to release and go back to the starting position.

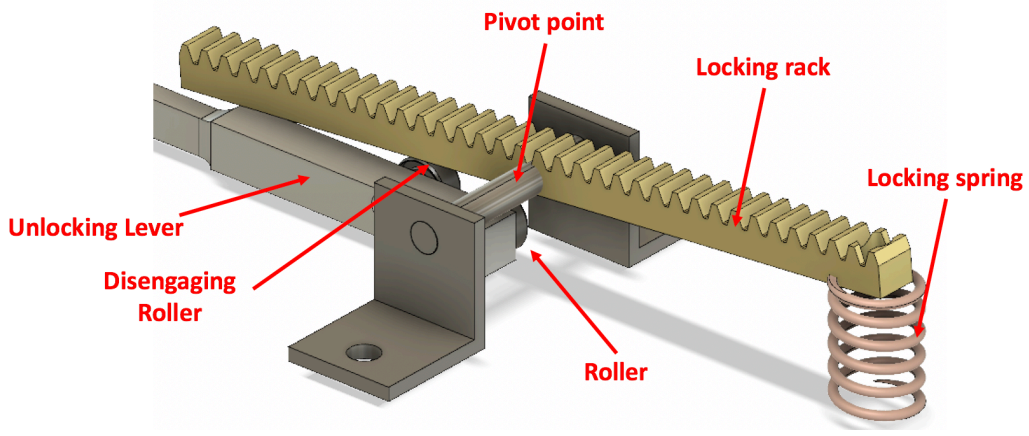

Figure 2.12- Engaging and disengaging mechanism that makes the backpack decoupled.

The only condition when the proposed design can depart from the predictions is at resonance. Here the resonance is avoided in the design as it would be highly uncomfortable to the user. At resonance, the high amplitudes of the bag would make the slider move upwards too much, and thus as a result, during the downward stroke the rack will be open while moving down

until it crosses the pivot point. A free body diagram (FBD) of the locking rack is shown in Figure 2.13.

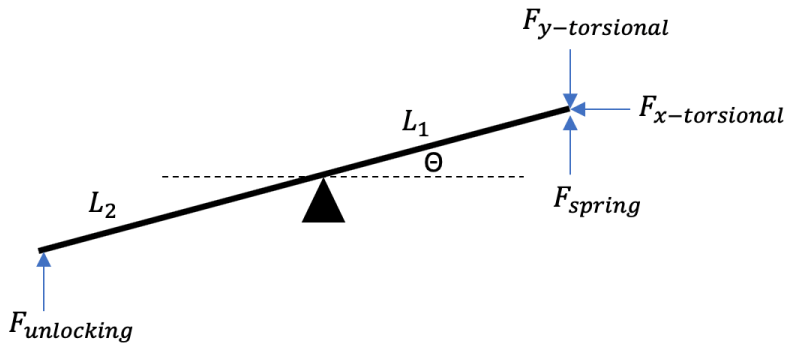

Figure 2.13- Free body diagram (FBD) of locking and unlocking sub-assembly.

In Figure 2.13, the length of the engaging and disengaging mechanism L is defined as

$$L = L_1 + L_2 \tag{2.4}$$

When the backpack goes in downward motion, $F_{y-torsional}$ and $F_{x-torsional}$ will be a nonzero force. The locking spring force F_{spring} will be greater than $F_{y-torsional}$ so the engaging pawl does not open. While the angle Θ needs to be close to zero so the $F_{x-torsional}$ does not affect the overall sum of torques around the pivot point. At this point, $F_{unlocking} = 0$. When the backpack moves upwards, $F_{unlocking} > 0$ and equal to the mass times the relative acceleration of the backpack. Since $L_2 > L_1$ the torque from the unlocking system around the pivot point will be greater than the one from F_{spring}; therefore, unlocking the torsional spring without effort.

2.4 Backpack Harvester Modeling

2.4.1 Governing Equations

The decoupled backpack harvester is modeled as a spring mass damper system excited by support motion. In the downward stroke, the clutch A (Figure 2.11) allows the rack to wind the torsional spring by an angle governed by pinion radius and relative displacement. As the generator

is not present in this stroke, the only damping comes from the guiding rails and springs. The damping of the linear and torsional spring is represented as *c* and *s*, respectively. The linear spring stiffness, radius of pinion, torsional spring stiffness, mass and pinion inertia are denoted by *k*, r_1, *q, m* and I_1. The relative displacement of the bag is denoted by y_r such that $y_r = y - y_b$, where y and y_b are absolute displacement of the payload and base displacement. Similar representation is followed for the pinion rotation angle θ_1. The governing equations for backpack forces and moments at the input pinion for a downward stroke are derived as

$$m\ddot{y_r} + c\dot{y_r} + ky_r + F = -m\ddot{y_b} \tag{2.5}$$

$$I_1\ddot{\theta_1} + s\dot{\theta_1} + q\theta_1 = Fr_1 + s\dot{\theta_b} + q\theta_b \tag{2.6}$$

where *F* is the force acting on the mass at the interface between rack and pinion due to the torsional spring. The energy absorbed by the torsional spring in the downward stroke is the energy potentially available for harvesting. Thus, the condition at which the energy absorbed by the torsional spring is maximum is determined by maximizing the energy with respect to the torsional spring stiffness, q. Using this condition, the maximum value of energy that can be extracted from the harvester is determined by the average energy in the torsional spring over half cycle

$$PE_{rot} = \frac{1}{2}Fr_1\theta_r = \frac{1}{4}q\theta_r^2 \ , \tag{2.7}$$

where θ_r is the relative angular displacement. Assuming the base excitation motion is in the form $y_b = Y_b \sin(wt)$ one can solve for the amplitude of Y_r

$$Y_r = \frac{\sqrt{K^2 + C^2w^2}}{\sqrt{K^2 + C^2w^2 - 2KMw^2 + M^2w^4}}\, Y_b \tag{2.8}$$

where $M = \frac{m+I_1}{r_1^2}$, $C = \frac{c+s}{r_1^2}$ and $K = \frac{k+q}{r_1^2}$. Dividing the amplitude of the vertical relative motion by the radius of the gear one gets θ_r.

The rotational energy, PE_{rot} , is differentiated with respect to q and equaled to zero to determine the optimal q as

$$\frac{\delta}{\delta q} PE_{rot} = 0, \tag{2.9}$$

$$q_{opt} = kr_1^2 \sqrt{(1-\Omega^2)^2 + 4\zeta^2\Omega^2} \tag{2.10}$$

where Ω is the ratio of driving frequency to the resonant frequency and ζ is the mechanical damping ratio. Hence, by knowing the linear spring stiffness, radius of pinion, damping ratio and the operating frequency, one can determine the required torsional spring stiffness using Eqn. 2.10. During the downward stroke, Eqns. 2.5 and 2.6 can be used to describe the motion; however, in the upward stroke the same equations can be used to describe the system by setting q and s equal to zero. The upward stroke releases the mechanical energy stored in the torsional spring to the generator. The combined inertia of generator, shaft and the gear are denoted as I_g. The gear box has a gear ratio, g, which is the ratio of the angular velocity of the driving gear to that of the driven gear. Rotational angle of the generator is denoted by θ_r and the generator damping coefficient is denoted by b. The governing equation of motion for the generator is given as

$$I_g\ddot{\theta}_r + b\dot{\theta}_r + qg^2\theta_r = 0 \tag{2.11}$$

The generator damping coefficient b are determined using the speed constant K_s, torque constant K_t, internal and external resistances (R_i and R_l), and the rotational speed $\dot{\theta}_r$ as [32]

$$b = \frac{K_t}{K_s(R_i + R_l)} \tag{2.12}$$

Here the torque constant, K_t and K_s have the units of Nm/A and rad/Vs respectively. The generator response to the input in the form of initial angle θ_0 at the torsional spring is determined using Eqn. 2.11. The voltage developed by the generator is given by

$$V = \frac{\dot{\theta}_r R_l}{K_s(R_l + R_i)}. \tag{2.13}$$

The power from the generator is determined using the voltage given by Eqn. 2.13 and the load resistance R_l as $P = V_{rms}^2/R_l$. The power input to the harvester is determined from the total force and relative velocity of the bag. The average power input (P_{in}) is obtained by integrating the product total force and relative velocity. The total force consists of the sum of the spring force $F_k = ky_r$, damping force $F_c = c\dot{y_r}$ in upward and downward strokes, and the force at the torsional spring $F_q = qy_r/r_1^2$. The overall efficiency of the backpack harvester can be calculated by dividing RMS electrical power over RMS mechanical input power.

The semi-decoupled energy harvester which generates electrical energy in the downward direction is governed by the equation

$$M\ddot{y_r} + C\dot{y_r} + ky_r = -C_b\dot{y_b} - M\ddot{y_b} \tag{2.14}$$

where $M = m + \frac{I_3}{(gr_1)^2}, C = c + \frac{b}{gr_1^2}$, and $C_b = \frac{b(1-g)}{(gr_1)^2}$. In upward motion, the governing equation can be obtained by using Eqn. 2.14 and setting $g^{-1} = 0$. Eqn. 2.14 is obtained by using the relation between the rotation rate of the generator and the absolute velocity, $\dot{y} = g(\dot{y_b} + r_1\dot{\theta}_r)$. The reaction force at the generator onto the frame is given by $F_f = \mathrm{b}\dot{\theta}_r/r_1$. The voltage developed by the generator is given by Eqn. 2.13; however, the generator rotation rate is solved separately in downward and upward strokes. The average power input in the case of a semi-decoupled harvester is determined as:

$$P_{in} = \frac{1}{T}\int_0^T (F_k + F_c + F_f)\dot{y_b}\, dt \tag{2.15}$$

A two-way coupled energy harvester, harvesting energy in upward and downward directions, is governed by Eqn. 2.14. The generator rotation rate is used to evaluate the power

developed by the fully coupled harvester from Eqn. 2.13. The average power is calculated by using Eqn. 2.15 that is in turn used to estimate the efficiency of the harvester. These methods are later used to compare the performance of the fully coupled, semi-decoupled and decoupled harvesters.

2.4.2 Simulations

The power generated by both semi-decoupled and decoupled harvesters is simulated using the method developed in the Section 2.4.1. The parameters used in the simulation are listed in Table 2.2. A backpack load of 12.8 kg and a linear spring with rate of 0.5 N/mm are selected for simulation. The support motion to the backpack is determined by assuming leg length and step length as listed in Table 2.2 resulting in an amplitude of 12 mm and the pack vertical frequency of 2.2 Hz corresponding to the walking speed of 4 mph. The mechanical damping ratio is assumed to be 0.1 for simulations. A torsional spring of stiffness 0.07 Nm/rad is selected using Eqn. 2.9. As both harvesters have boundary conditions changing in each half cycle, the system is nonlinear and the equations are simulated using MATLAB Simulink.

Table 2.2- List of attributes of the harvester for simulations.

Parameter	Value
Backpack mass (kg)	12.8
Linear spring stiffness (N/m)	0.50
Leg length (m)	0.78
Step length (m)	0.40
Walking speed (mph)	4.00
Torsional spring stiffness (Nm/rad)	0.07
Generator torque constant (mN m/A)	35.0
Generator internal resistance (Ω)	16.0
Pinion radius (mm)	5.50

The relative acceleration and voltage developed by the semi-decoupled harvester across 40 Ω external resistance is shown in Figure 2.14A and Figure 2.14B. It can be noticed that the acceleration is asymmetric due to the one-way clutch A. As the clutch is used in both semi-decoupled and decoupled harvesters, the two harvesters possess similar negative accelerations.

However, the displacement in decoupled harvester is limited by the torsional spring. As the pack moves down, the resistance offered by the torsional spring in decoupled harvester increases the upward acceleration thereby reducing the net force on the person. A plot of displacement as a function of time for three speeds is shown in Figure 2.14C. It can be observed that unlike the acceleration, the displacement is relatively continuous. A plot of the voltage developed by the harvester in decoupled configuration for quarter turns of the spring is shown in Figure 2.14D. Additionally, the voltage output over one second is shown in the plot. As the frequency of oscillation is experimentally observed to be close to 2 Hz, the actual plot of voltage would have another similar voltage pulse in the second half of the plot. Thus, for sufficient input turns the voltage from the generator would not drop to zero. It can be observed that the voltages generated from semi-decoupled and decoupled harvesters are similar in order; however, the upward acceleration in decoupled harvester due to a spring decreases the net force on the person. The experimental results of two harvesters are discussed in the next sections. Moreover, the input power to the backpack would give a better estimation of power expended by the person.

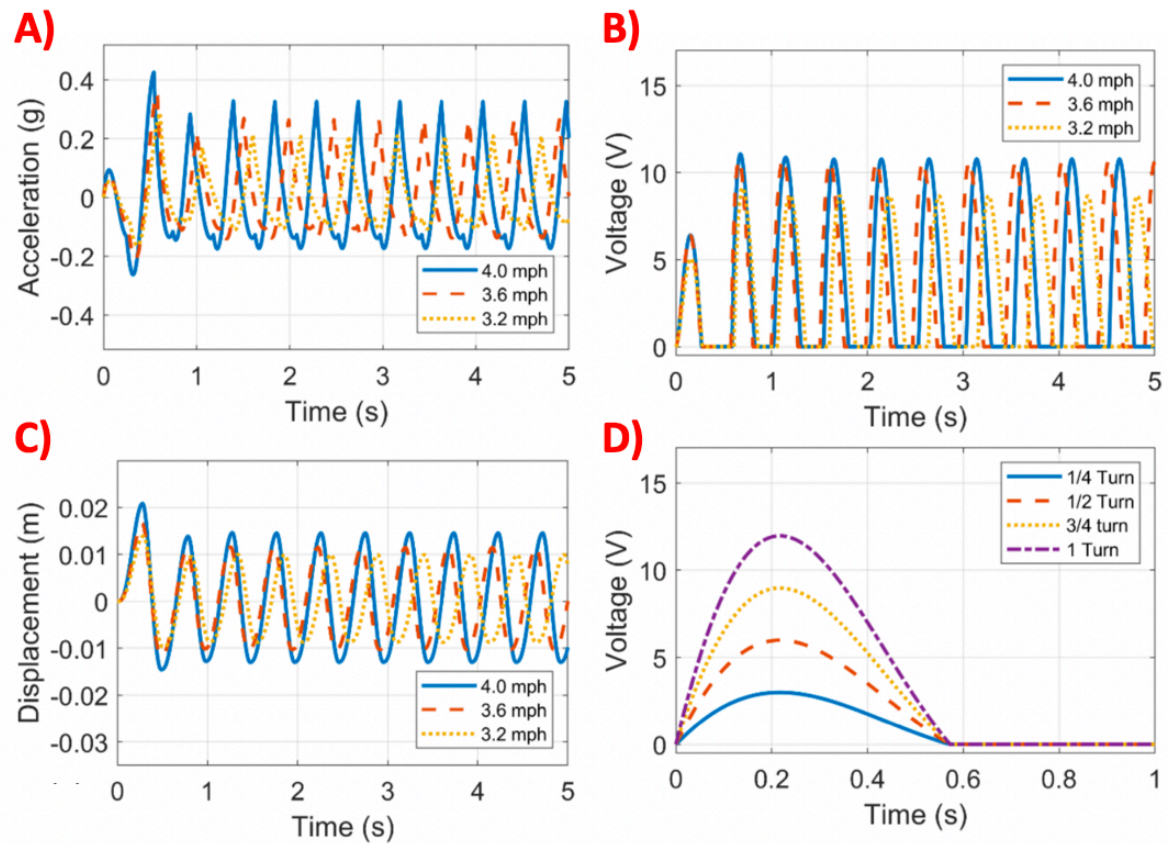

Figure 2.14- Simulation results of semi-decoupled and decoupled backpack harvesters. A) The relative acceleration of the backpack for an input displacement of 12 mm as a function of time in the case of semi-decoupled harvester. B) The voltage developed by the semi-decoupled harvester. As the upward stroke does not perform work, the generator voltage is zero. C) The displacement of the pack mass as a function of time and walking speed in the case of decoupled harvester. D) The voltage developed by the generator for four quarter turns corresponding to the displacement shown in C) for 4 mph speed.

The power absorbed by the decoupled harvester is estimated by following the procedure described above. The power input to the backpack and output from the harvester are estimated to be 5.70 W and 1.58 W respectively. This results in an efficiency of 27.7%. It may be noted that the power levels are estimated for an input base velocity of 0.5 m/s corresponding to a base amplitude of an inch.

In these simulations, the damping ratio is kept at 0.1 across all the three configurations. The other two configurations are semi-decoupled and fully coupled harvester. A Simulink model

of the semi-decoupled backpack harvester is shown in Figure 2.15A. If the clutch in Figure 2.15A is removed, the same model acts as a fully coupled harvester.

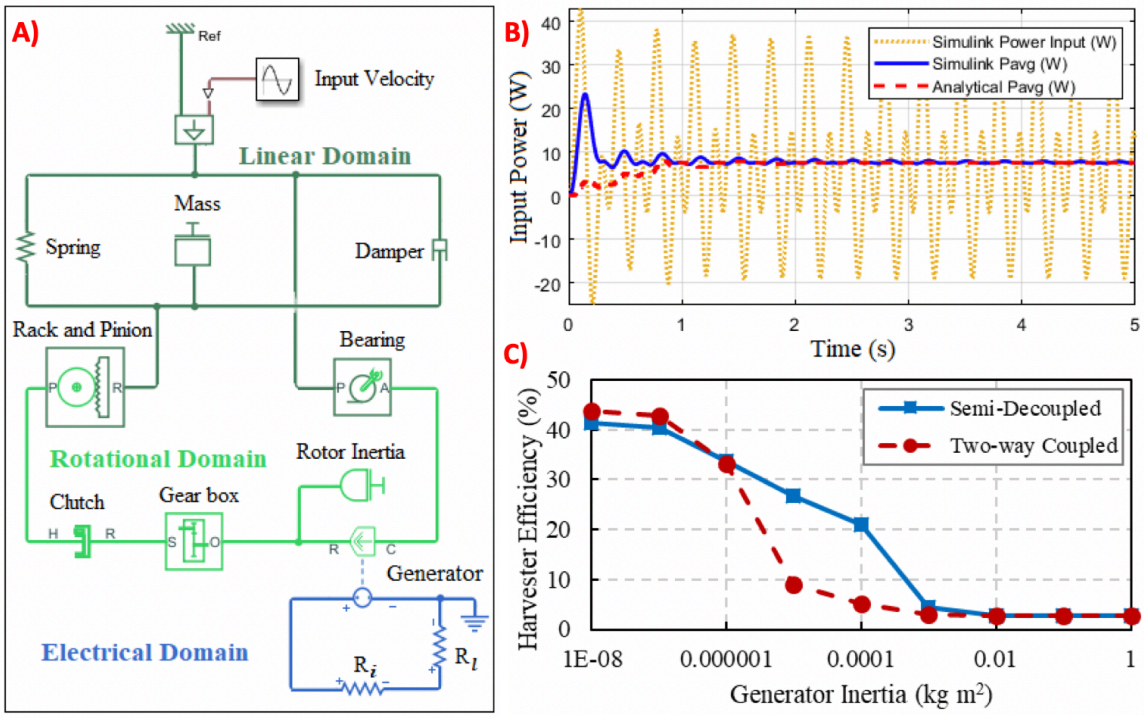

Figure 2.15- A) A Simulink model of the semi-decoupled backpack energy harvester arranged into three categories – linear, rotational and electrical. B) The comparison of power input to the semi-decoupled backpack harvester obtained from Simulink and the proposed analysis. C) The comparison of efficiency of semi-decoupled harvester with that of a two-way coupled harvester. The semi-decoupled harvester outperforms the two-way coupled harvester at the selected generator inertia of 1e-5 kg m^2.

The model consists of three domains: linear, rotational and electrical domains. The linear domain entails a payload mass, linear spring, damper and a rack. The across-variable is velocity and the through-variable is force. The rotational domain consists of pinion, clutch, gearbox and generator arranged as shown Figure 2.15A. The torque at the two-port generator in rotational domain is proportional to the current in the electrical domain through the torque constant. The electrical domain consists of internal and external load resistances. It can be observed from

Figure 2.15A that when the generator is resting on the frame, the input base velocity of the generator is same as that of the spring, and damper. However, the input force is distributed between the three components. The total instantaneous input power and the average input power are compared with the analytical input power estimated using Eqn. 2.15 in Figure 2.15B. It can be observed that the estimated average power (7.56 W) closely matches with that computed in Simulink. Similarly, the power output from the harvester is estimated to be 2.26 W, however, the useful power across the load resistance is 2.01 W resulting in a conversion efficiency of 26.8%. It can also be identified that the decoupled harvester absorbs 24% less input power maintaining the same efficiency for the given speed and mass. A similar analysis is adopted to estimate the power input and output of a fully coupled backpack harvester. This two-way fully coupled harvester is obtained from the model shown in Figure 2.15A by removing the clutch and shorting the H-R terminals. It is noticed that the output power generated by the fully coupled harvester is 0.49 W while the input power is 4.84 W resulting in a poor efficiency of 9%. It is further observed that the generator inertia plays a significant role in generated power and hence the efficiency. A plot of conversion efficiency for both semi-decoupled and fully coupled harvesters as a function of generator inertia is shown in Figure 2.15C. It should be noted from Figure 2.15C that fully coupled harvesters have higher efficiencies only below a certain value of the generator inertia. In this analysis, the semi-decoupled harvester outperforms the fully coupled harvester above a generator inertia of 1e-6 kg m^2. For the selected generator inertia of 1e-5 kg m^2, as the fully coupled harvester has less conversion efficiency, the experiments are performed only on the semi-decoupled harvester and the decoupled backpack harvester. The experimental results of the two backpack harvesters are discussed in the next section.

2.5 Methods

Three different subjects between the age of 25-30 years were asked to wear a backpack energy harvester and walk on a treadmill at 1.6, 2.4, 3.2 and 4 mph with two different weights of 10.5 kg and 12.8 kg. Once the test was completed, a resting break of 15 minutes was given while adjustments were made to decouple the energy harvester. Finally, the same test was repeated with the decoupled energy harvester.

2.5.1 Data Acquisition and Processing

The backpack energy harvester was instrumented with a load cell, displacement sensor and accelerometers as shown in Figure 2.16C. All the sensors were connected to a data acquisition system with a sampling rate of 25000 Hz.

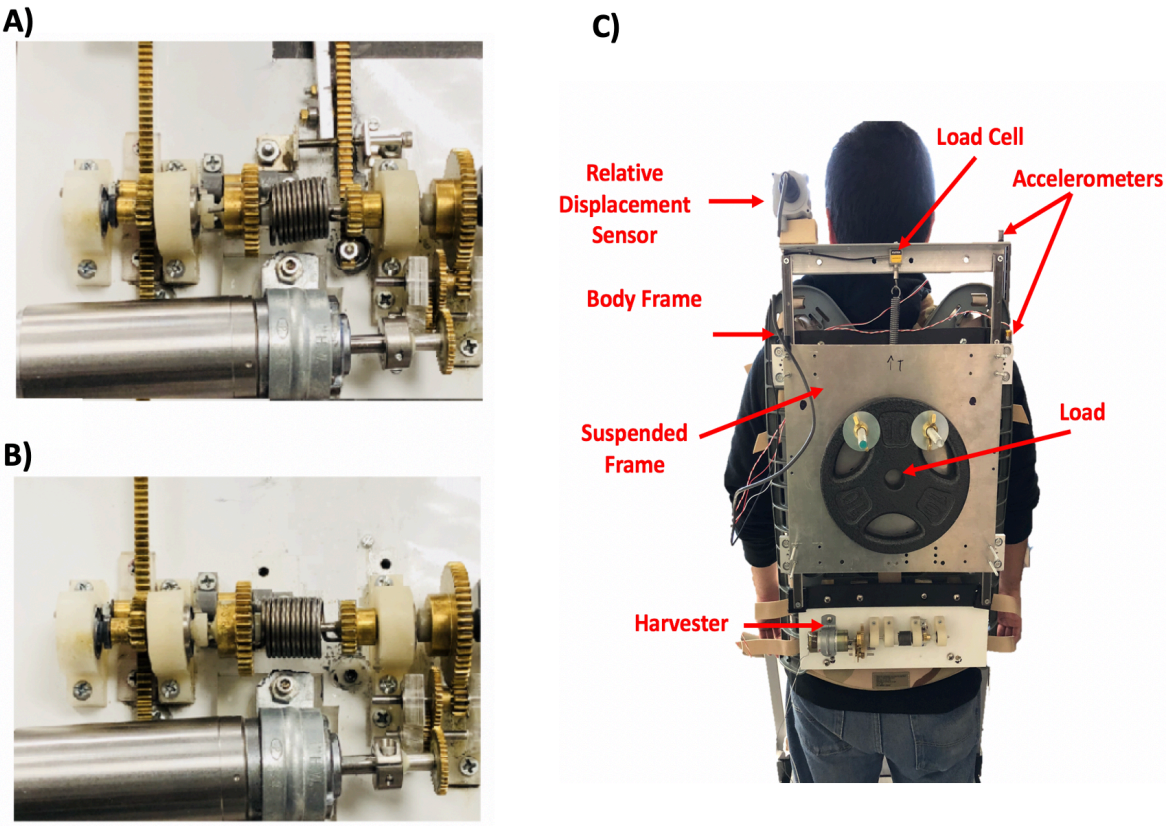

Figure 2.16- A) Decoupled energy harvester. B) Semi-decoupled energy harvester. C) Arrangement of sensors to measure displacement, forces and power.

Redundancy in the testing set up is used to double check the data collected. For example, the relative displacement sensor data could also be acquired from the accelerometer data. The data processing consisted of first using a bandpass Butterworth filter on the frame accelerometer with 0.5 Hz and 5 Hz as the limit frequencies, since walking frequencies should not be outside this range. A fast Fourier transform (FFT) was applied to the frame accelerometer and the frequency with higher amplitude was noted as the dominant walking frequency. The COM displacement and load displacement was acquired by integrating twice each accelerometers data. The subtraction between the bag displacement and frame displacement was confirmed with the relative displacement sensor data. Harvested power was measured from the output of the generator. The force at spring support, natural frequency of the system, walking speeds were all determined. This same procedure was used for both decoupled backpack harvester and semi-decoupled backpack harvester.

2.6 Experimental Results

The performance of the semi-decoupled and decoupled harvester is evaluated by three subjects walking on a treadmill. As the output across the three subjects from both harvesters is observed to be within 20%, the results from only one subject are presented. The selected speeds are 3.2 mph, 3.6 mph and 4 mph. The spring constants used are 0.5 N/mm and 2.2 N/mm while the suspended mass used are 10.5 kg and 12.8 kg. A torsional spring rate of 0.08 Nm/rad is selected using Eqn. 2.9 for the selected spring and mass ranges. The input pinion radius is 5.5 mm. Additionally, a gear box that enhances the speed by 20.7 times the input pinion is included. For comparison and maximum efficiency, the generator is driven only in the downward stroke in both harvesters. Moreover, the suspended mass and walking speeds are kept constant between

the two configurations for comparison. An optimal load resistance of 40 Ω is selected for all the tests.

The differences in step length and gait cycle among the three subjects resulted in marginal changes in the performance of the harvesters. Nevertheless, it is observed that the semi-decoupled harvester generates more power compared with the decoupled harvester. However, the relative displacement and the reaction force amplitudes are larger in semi-decoupled harvester. The voltage output from both semi-decoupled and decoupled harvester at 3.2 mph for 12.8 kg load is shown in Figure 2.17A. The acceleration response of the suspended payload mass is shown in Figure 2.17B. It may be noted that the downward acceleration is lower when the mass is moving up while the upward acceleration is higher when the mass is moving down. This is attributed to the use of one-way clutch that freewheels when the mass moves upwards. The relative displacement measured from the displacement sensor is plotted in Figure 2.17C. The relative displacement of the pack mass is almost 50% higher in the semi-decoupled harvester. This is attributed to the direct winding of the generator in the semi-decoupled harvester and the torsional spring stiffness in the decoupled harvester. As the pack mass moves down against the torsional spring in the decoupled harvester, the relative displacements are smaller. Similar explanation is applicable for the response from the force sensor. The plot in Figure 2.14D shows the force measured by the load cell at the top support position. The force is lower than the gravitational force as it includes the force along the spring and does not reflect the support reaction forces. It may be noted that the average force levels in both semi-decoupled and decoupled harvester are similar but the oscillatory amplitude of the force is larger in the semi-decoupled harvester while it is smaller in decoupled harvester. The average electrical power output, voltage, force and displacements are shown in Table 2.3 and 2.4.

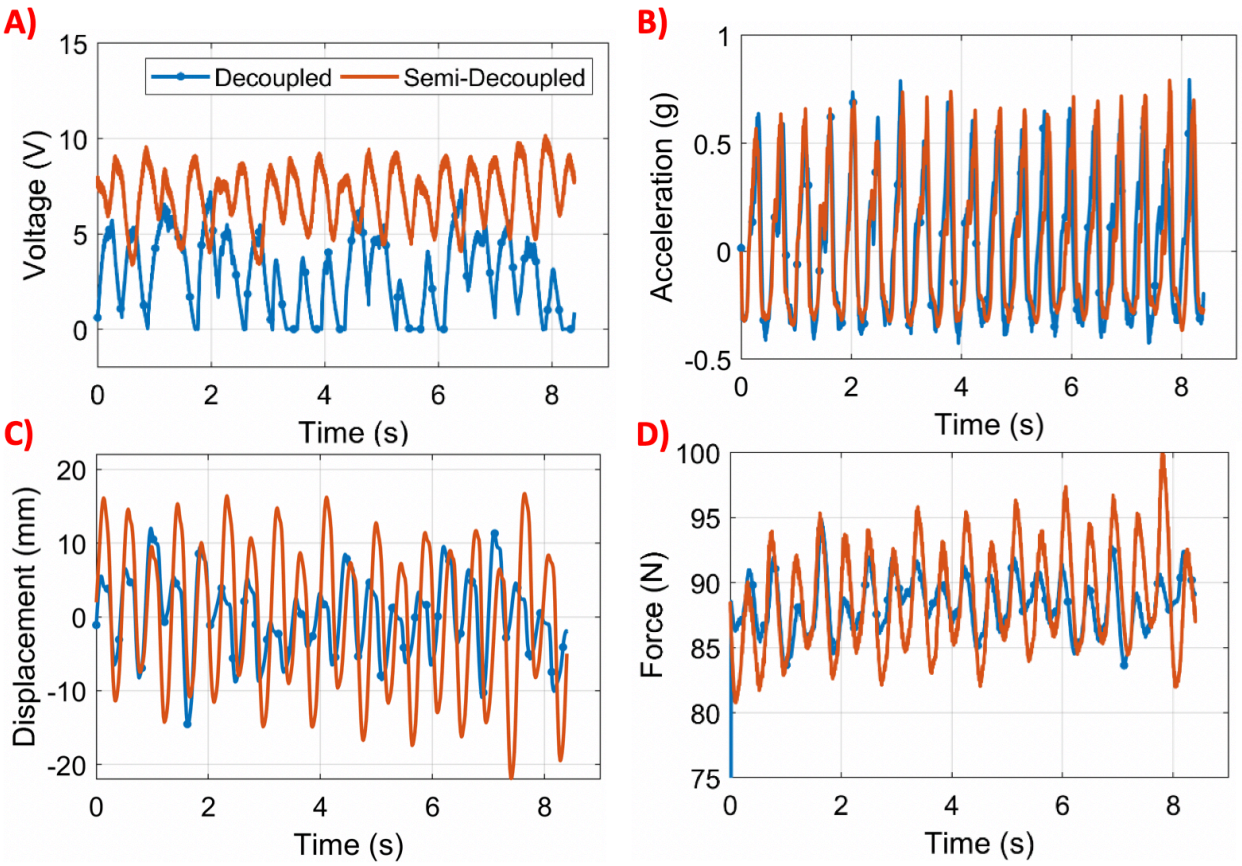

Figure 2.17- A) Voltage developed by the semi-decoupled and the decoupled harvesters for 12.8 kg mass at 4 mph speed as a function of time. The generator is driven only in one direction resulting in unidirectional output. B) The acceleration of the suspended mass as a function of time. The positive accelerations are higher when the mass is lower indicating the energy absorption. C) The relative displacement in both semi-decoupled and decoupled harvester. The displacements in decoupled harvester are 50% smaller than that in semi-decoupled harvester. D) The force measured by the load cell mounted at the top support point. It can be noted that the average force in both semi-decoupled and decoupled harvester is similar but the amplitude of oscillatory force is lower in decoupled harvester.

Table 2.3- Comparison of semi-decoupled and decoupled harvester output at 10.5 kg mass.

Parameter	Semi-decoupled Harvester			Decoupled Harvester		
Speed (mph)	3.20	3.60	4.00	3.20	3.60	4.00
Displacement RMS (mm)	5.88	6.59	7.68	3.50	3.60	4.37
Force RMS over mean (N)	2.84	3.30	3.79	1.49	1.57	2.17
Voltage RMS (V)	4.23	5.40	6.26	2.44	3.42	3.53
Average Power out (W)	0.45	0.73	0.98	0.15	0.29	0.31
Average Power in (W)	1.25	2.19	3.27	0.37	0.87	1.15

Table 2.4- Comparison of semi-decoupled and decoupled harvester output at 12.8 kg mass.

Parameter	Semi-decoupled Harvester			Decoupled Harvester		
Speed (mph)	3.20	3.60	4.00	3.20	3.60	4.00
Displacement RMS (mm)	8.65	10.63	10.95	4.25	7.54	9.05
Force RMS over mean (N)	3.28	4.28	4.55	1.68	3.05	3.85
Voltage RMS (V)	7.13	8.14	9.27	3.57	5.72	7.48
Average Power out (W)	1.27	1.65	2.15	0.32	0.82	1.40
Average Power in (W)	3.35	5.52	7.44	0.82	2.67	5.11

The voltage response from the harvesters at three speeds is measured and shown in Figure 2.18A. It can be observed that the voltage from the semi-decoupled harvester does not drop to zero due to the rotational inertia of the generator. However, the voltage from the decoupled harvester drops to zero as the torque is released only towards the end of the upward stroke. At lower speeds the decoupled harvester with higher mass can have lower performance than the semi-decoupled harvester with lower mass as shown in Figure 2.18B. Nevertheless, the difference in RMS voltage between the semi-decoupled and decoupled harvesters decreases with the walking speed as shown in Figure 2.18B. The power from the semi-decoupled and decoupled harvesters at 4 mph (1.8 m/s) with 12.8 kg pack mass is 2.15 W and 1.40 W respectively. In

terms of specific power, the semi-decoupled harvester provides 0.17 W/kg and the decoupled harvester exhibits 0.11 W/kg as shown in Figure 2.18C. A comparison of the power output from by harvesters with that published in the literature is shown in Table 2.5.

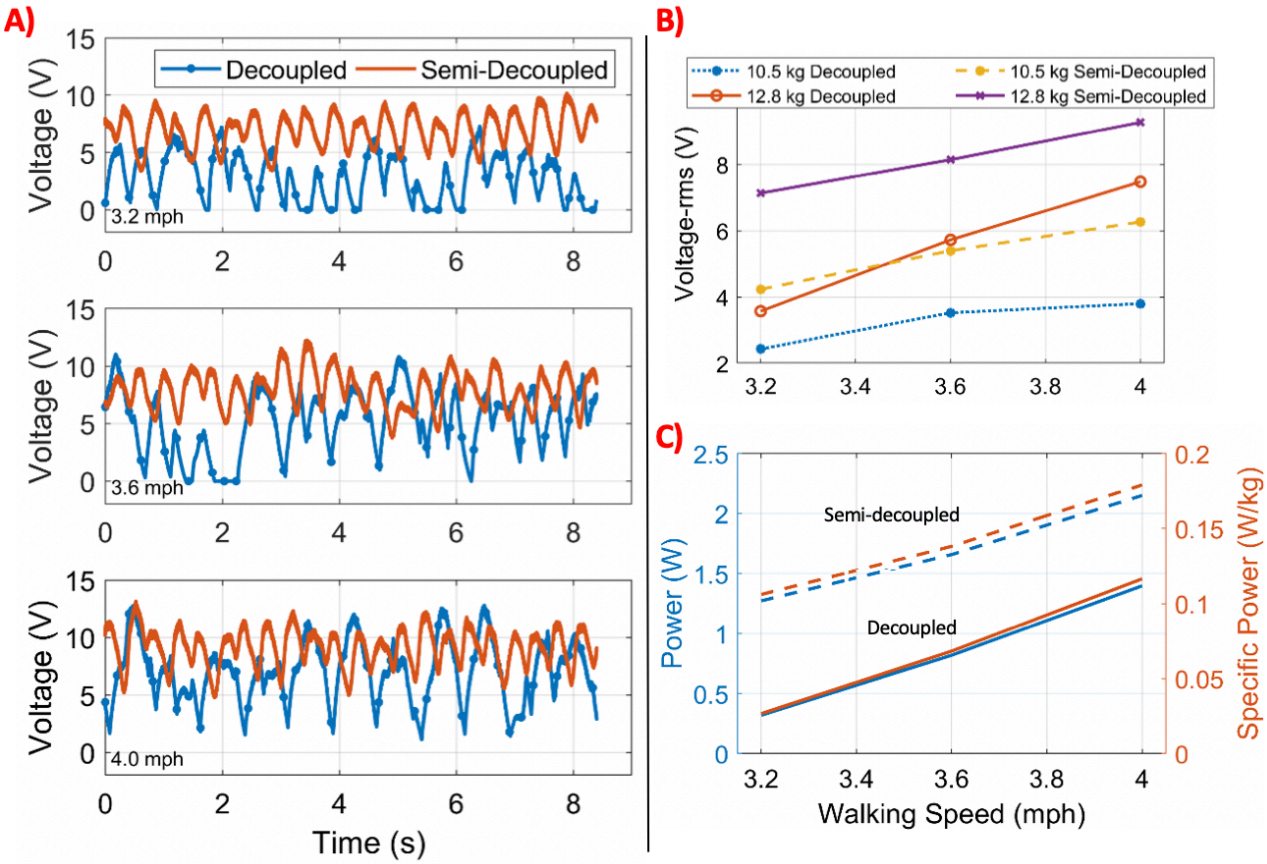

Figure 2.18- A) Voltage from semi-decoupled and decoupled harvesters at three speeds, 3.2 mph (1.4 m/s), 3.6 mph (1.6 m/s) and 4.0 mph (1.8 m/s). The minimum value of the voltage in semi-decoupled harvester is non-zero due to the inertia of the rotating elements. The minimum value of the voltage in decoupled harvester increases with walking speed. B) The rms voltage as a function of walking speed at two different loads. It can be observed that the difference in voltage decreases with walking speed. C) The power and specific power are plotted as a function of walking speed. It is observed that the difference in specific power of semi-decoupled and decoupled harvester decreases with the walking speed.

Table 2.5- Comparison of backpack energy harvester performance with the published literature.

Reference	Mass (kg)	Speed (mph)	Average Output Power (W)	Average Input Power (W)
Rome et al. [18]	29	4	3.71	12.15
Xie et al. [20]	15	3.5	4.1	-
Yuan et al. [19]	13.6	3.5	Subject A: 3.20	-
			Subject B: 2.50	-
This work	12.8	4	Decoupled: 1.40	5.11
			Semi-decoupled: 2.15	7.44

It must be emphasized that the input power to the harvester in the case of decoupled harvester is 5.11 W while in the case of the semi-decoupled harvester is 2.33 W more for the same speed and payload mass. The efficiency of conversion for both decoupled and semi-decoupled harvesters is close to 28%. The distinctive advantage of a decoupled harvester is the decrease in the input power by 31% while maintaining the same efficiency. By improving the efficiency of the harvester, a decoupled backpack harvester can be designed to draw less power from the person compared to a semi-decoupled harvester. As the response from the decoupled harvester depends on the specific time of release of the torsion spring, the performance depends on the walking speed with the existing torque release mechanism. Experimentally, the oscillatory amplitudes of force at the spring support and the relative displacement of the pack mass are observed to be lower in the decoupled harvester.

2.7 Representation of Backpack Energy Harvesters

Power vs. velocity curves at different backpack masses show that as the velocity of the human and the weight of the bag increases a higher electrical power can be harvested [18]. Unfortunately, these graphical plots are not informative since humans use more energy to walk faster; therefore, more energy can be harvested from their motion. On the other hand, a heavier

bag when suspended would generate a greater mechanical power since mechanically power can be defined as [18]:

$$P_{mechanical} = F * v \tag{2.16}$$

where F incorporates the weight and accelerative force of the bag and v is the bag velocity. Thus, as the mechanical power increases in the system a greater electrical power can be harvested. For this reason, a new representation of results needs to be created to accurately represent the suspended backpack vibration system by including velocity, power, mass and spring stiffness. In this section, a new semi-decoupled mechanism was built which only generates power in the down stroke direction by using a clutch bearing (Figure 2.19).

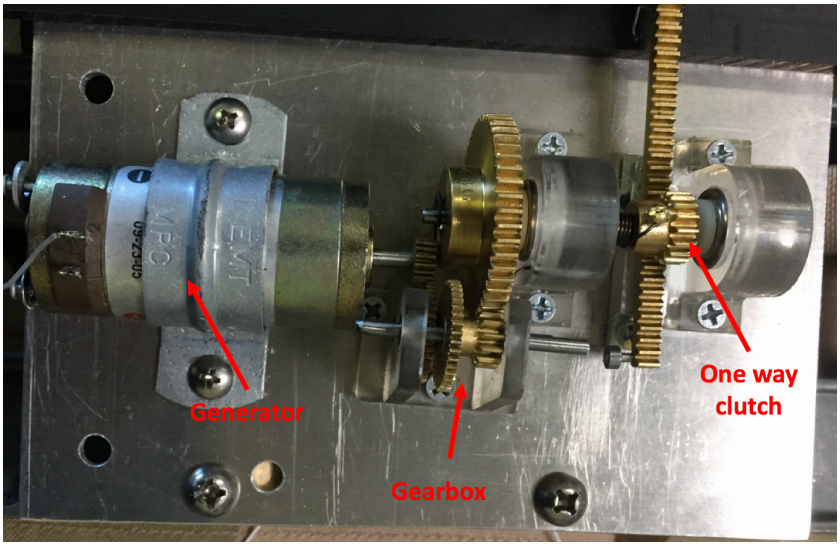

Figure 2.19- Semi-decoupled backpack harvester contains a gearbox with ratio 1:25 for amplification of power.

Four different subjects walked on a treadmill using a semi-decoupled electromechanical backpack energy harvester at four different speeds of 1.8, 2.4, 3.2 and 4 mph. Each subject walked with a combination of mass and spring stiffness. Different weights were used since a low stiffness spring is not able to carry high loads. In order to compare all the data, a new plot is created by normalizing average acceleration force

$$F_{norm} = \frac{F_{rms\_acc}}{Weight} \tag{2.17}$$

where the acceleration forces of the backpack are divided by its weight for easily comparison and plotted against the spring and mass combination or natural frequency of the system. The experimental data is shown in Figure 2.20.

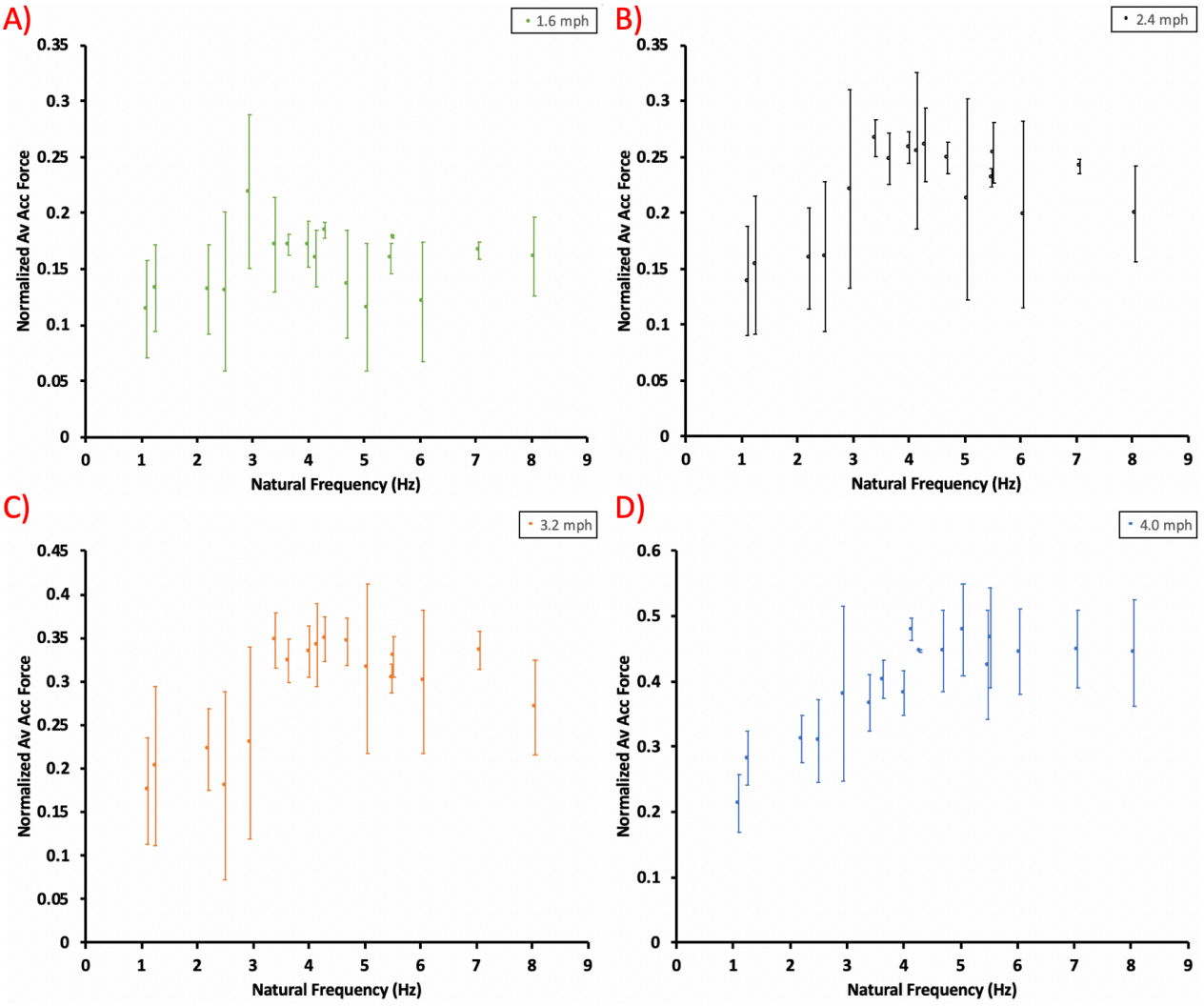

Figure 2.20- Maximum normalized forces when walking at 1.6 mph, 2.4 mph, 3.2 mph and 4 mph around a natural frequency of 3.00 Hz, 3.40 Hz, 4.29 Hz and 5.00 Hz respectively. The resonance in the system is dependent of the walking frequency of the wearer.

To find the best natural frequency, spring and mass combination, to harvest energy while reducing forces. The output power density of the harvester at different natural frequencies is plotted in Figure 2.21. In this figure, power density is calculated by dividing the RMS power generated by the mechanism over the mass of the suspended payload.

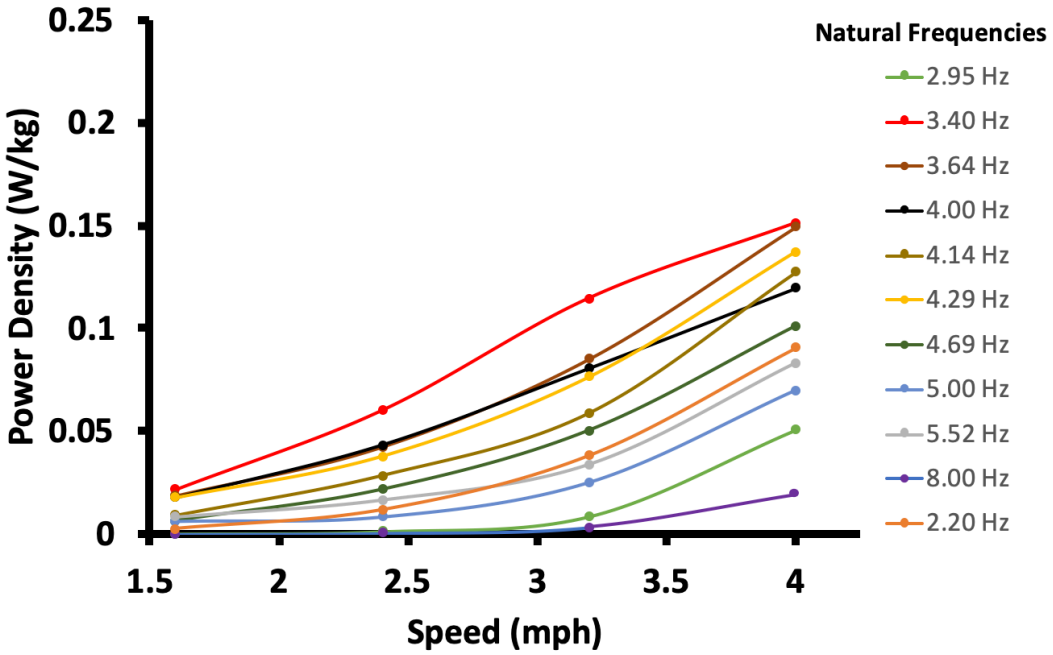

Figure 2.21- Power density of semi-decoupled backpack energy harvester at different natural frequencies and walking speeds.

By comparing Figure 2.20 and 2.21, it can be observed that a maximum power per kilogram occurs at natural frequency of 3.4 Hz for the four different speeds. However, at 3.4 Hz there is a high accelerative force acting on the wearer at all the speeds. This same phenomenon occurs at all high electrical power levels; therefore, one can conclude that for a common rack and pinion mechanisms high power output comes with increase in metabolic rate. If one wants to mitigate accelerative forces a low natural frequency backpack is desired. At higher natural frequencies above the resonance frequency as shown in Figure 2.20, the accelerative forces of the bag acting on the wearer is constant since at this stage the backpack will behave as a locked mechanism. This figure also confirms that the system is a one degree of freedom isolator as

shown in classical vibration theory by Inman [31]. From Figure 2.20, three points at 3.2 mph can be examined: resonance, isolation and locked backpack. At a walking speed of 3.2 mph this occurs at natural frequencies of 4.3 Hz, 1.1 Hz and 8.0 Hz, respectively.

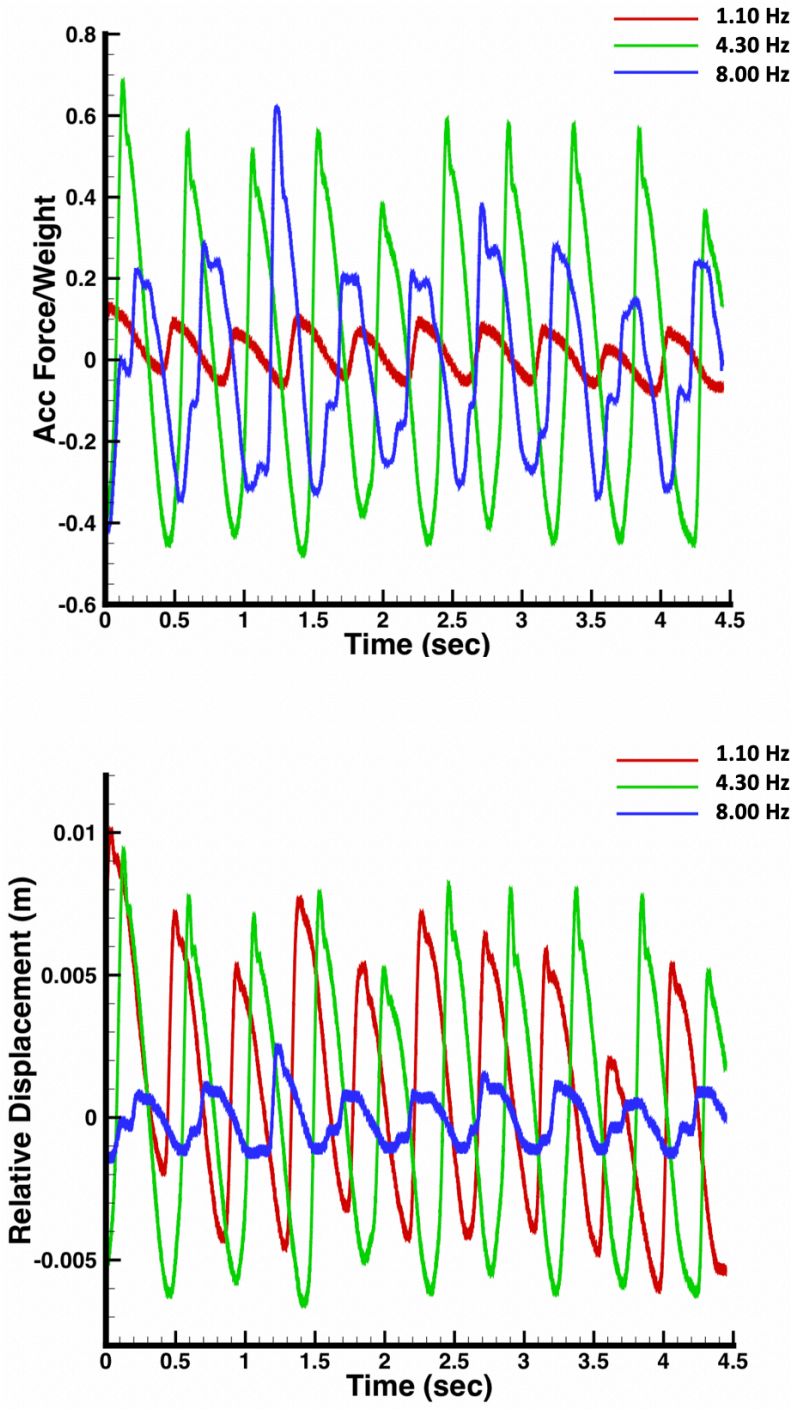

Figure 2.22- (Top) Force ratio of backpack under three different natural frequencies. (Bottom) Relative displacement between bag and frame at the same natural frequencies.

As shown in Figure 2.22, at a low natural frequency (1.10 Hz) the backpack energy harvester shows a higher relative displacement and small normalized force amplitude. In this case, the payload is still while the frame movement creates the high relative displacement. On the contrary, an energy harvester backpack under resonance (4.30 Hz) has the highest relative displacement and normalized force amplitudes. Furthermore, a locked or high natural frequency backpack (8.00 Hz) when compared to a low natural frequency system (1.10 Hz) will increase the forces on the wearer while relative displacement will be the lowest.

Chapter 3 Powering Mobile Devices Using a Decoupled Shoe Sole Energy Harvester

3.1 Introduction

During gait, the relative motion between each body segment can be used to harvest energy. Compared to different body joints, the ankle joint segments produce the most biomechanical power per step ([33], [34]). For this reason, this is a potential location where a higher amount of electrical energy could be harvested by placing an energy harvester. At the ankle joint, it has been shown that a mechanical spring could lower metabolic rate by helping fulfill functions of the calf muscles and Achilles tendon [35]. This chapter focuses on the development and testing of a decoupled ankle harvester which can reduce metabolic rate by winding a spring during the negative work of the ankle, thereby, helping the calf muscles and Achilles tendons. The mechanical energy stored in a spring is released to a generator during the heel off event.

3.2 Literature Review

In this section, different types of lower limb exoskeletons which are meant to help users restore lost functions or reduce their metabolic rate are examined. In addition, different energy harvesting mechanisms and technologies are reviewed for human lower extremities.

3.2.1 Lower Limb Powered Exoskeletons

Powered exoskeletons have been the focus of commercial entities. They normally run on lithium ion batteries or power cables. One of the most commonly known technology is Berkley's Lower Extremity Exoskeleton (BLEEX) which was designed to endure and strengthen lower limbs to support heavy payloads [36]. Large corporations such as Honda, Raytheon and Lockheed Martin have also been developing their own exoskeletons to support lifting of heavy payloads or for medical use to help patients to walk. Nonetheless, exoskeleton technology is limited by the power supplied to the actuators. The robotic exoskeleton will pause to work once the battery runs out of charge.

3.2.2 Lower Limb Pseudo-Passive Exoskeletons

These are also known as quasi-passive exoskeletons. They still utilize batteries but require minimal power to correct anomalies of a user when doing a task. The batteries are normally used to power sensors and not to provide actuation. The most commonly known pseudo-passive exoskeleton was developed in MIT [37]. This exoskeleton consisted of ankle and hip springs which stored energy during extension and released the stored energy during flexion. A variable knee damper was also included which controlled the dissipated energy at fitting levels through the gait cycle [37]. However, they found that this pseudo-passive exoskeleton increased the metabolic cost of the user by about 10%, but also noted that an exoskeleton without the pseudo-passive elements would increase the metabolic rate even more.

3.2.3 Lower Limb Passive Exoskeletons

Passive exoskeletons do not require any electrical power, which implies that they do not possess actuators or sensors. As a result, they store and relocate mechanical energy with gears, springs, clutches and dampers. These passive components must be ideally placed in order to

engage and disengage correctly during operation. An example of a passive exoskeleton is the work done by Collins et al.[35], where a clutch mechanism is used in order to wind a spring during the foot flat gait cycle phase and releasing it during heel off. As a result, their research showed a decrease in soleus activity and biological ankle moment. It is worth mentioning that the reduction of metabolic rate when wearing this device was due to the passive exoskeleton mechanism and the use of lightweight materials.

3.2.4 Foot Strike Energy Harvesters

The foot can harvest energy during the heel strike phase of gait. Many prior researchers ([38],[39],[40],[41],[42],[43]) have tried to harvest this energy using smart materials such as PZT/PVDF. The magnitude of power harvested varied from 0.35 mW to 90.3 mW depending upon the mechanical amplification system and material configuration. However, the higher is the electrical power generated by foot strike using smart material based mechanisms, the bulkier is the system. Recently, researchers have attempted to utilize triboelectric effects in order to generate power from the foot ([44],[45],[46],[47],[48],[49],[50]). Xie et al.[51] amplified the foot strike with a trapezoidal slider mechanism which drove a gear train into a microgenerator. Two springs were employed to exert a restoring force that enables the harvester to move to its original position. The power produced from this heel strike device was 1.39 W at 5 km/hr.

3.2.5 Knee Energy Harvesters

Knee brace energy harvesters use the relative angular motion between the femur and shank in order to generate electrical energy. Donelan et al. [9] showed that by using a one-way clutch one could only harvest energy during extension motion of the swing phase; therefore, assisting the knee flexor muscles in decelerating the knee. They concluded that by using a one-way clutch and only harvesting energy during the decelerating swing phase, subjects generated about 4.8 W of electricity with a 5 ± 21 W increase in metabolic cost when compared to a traditional knee harvester which generate 7.0 W with an 18± 21 W increase in metabolic cost. However, their average metabolic power was found to increase by almost 60 W when compared to a subject walking without the knee brace harvester. Pozzi et al. [52] demonstrated that PZTs could also be used for knee energy harvesting by using a moving hub which carry PZT inside an outer ring with inner plectra. This design was later improved by Kuang et al. [53] producing 5.8 mW.

3.2.6 Ankle Motion Energy Harvesters

Ankle energy harvesters use the relative angular motion between shank and foot to produce electrical energy. Most of the technologies for knee energy harvesting can be used for the ankle or any other rotational joint (Section 3.2.5). The ankle energy harvesting is dominated by electromagnetic induction harvesters ([54],[55],[56]) which produces greater power when compared to smart material systems. Electromagnetic induction systems can be constructed into two different architectures: 1) a magnet which moves along a stationary coil or 2) multiple magnets stack levitating between stationary magnets. This second configuration produces a higher output power and it has been shown to generate up to 8.5 mW in a shoe sole [57].

3.3 Foot Biomechanics Review

In a human being, flexion and extension describes most of the angle movement between two body parts. For hands and feet, the terms used to describe these movements are dorsiflexion and plantarflexion. Dorsiflexion refers to the motion between the foot and front of the leg, while plantarflexion refers to the movement between the foot and back of the leg. For a typical human ankle motion, power and torque curves are shown in Figure 3.1.

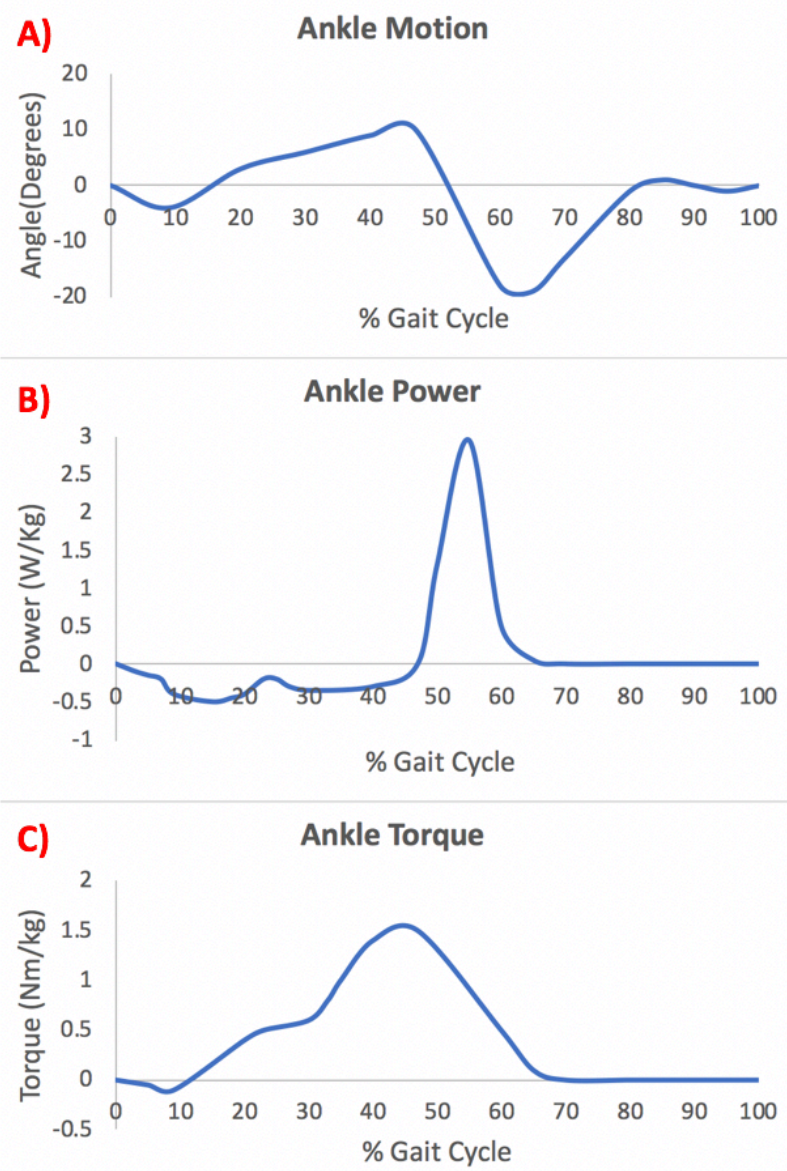

Figure 3.1- A) Ankle motion where positive degrees means dorsiflexion and negative means plantarflexion. B) Ankle power where negative power refers to downward COM movement and positive upward COM movement. C) Ankle torque where negative is the plantarflexion torque and positive is the dorsiflexion torque [6].

Figure 3.1B shows that most of the power production occurs in the positive region. This is the optimal region to increase energy harvested, however, it is not the region to aim as here muscles are acting as actuators to move the body. The region energy harvesters should aim is the negative power region since in this region muscles are acting as clutches to keep the body

balanced. The desired negative power region is between 9% to 47% of the gait cycle. Between 0% to 8%, negative energy is produced but muscles are still moving the joints to go from heel strike to foot flat. Mentiplay et al. [58] showed that when walking at different speeds the human body changes velocity and ankle range of motion in both dorsiflexion and plantarflexion regions, as shown in Figure 3.2. In other words, when walking at different speeds an energy harvester which is coupled to the ankle joint will experience different angular range of motion and velocities.

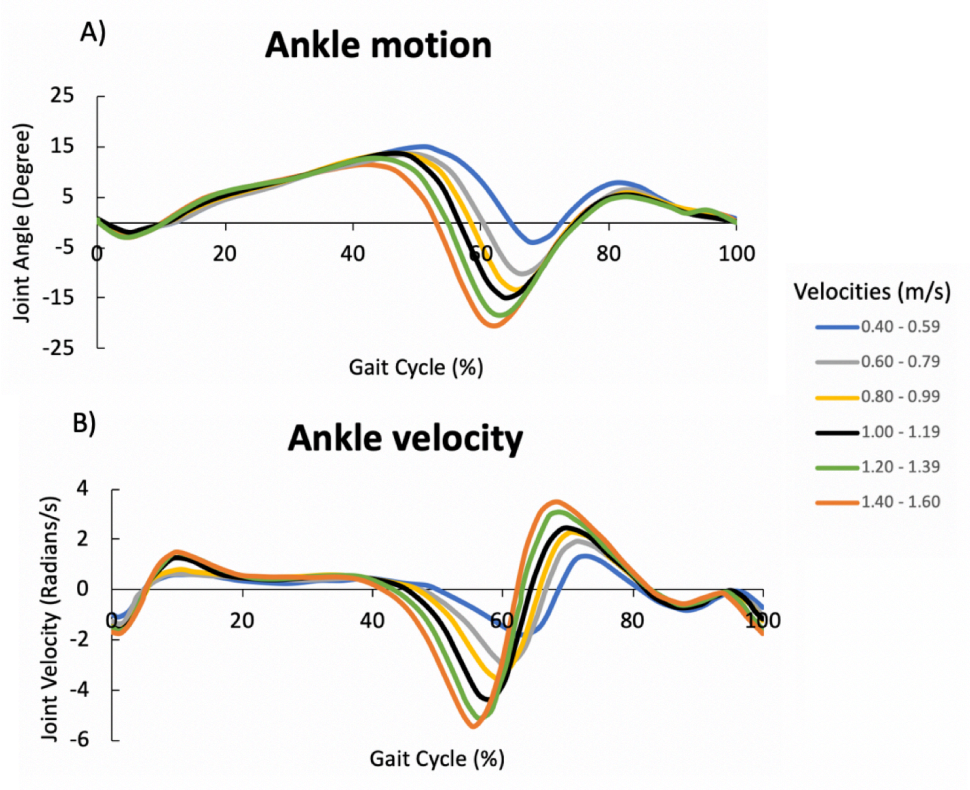

Figure 3.2- Ankle motion and velocity data derived by Mentiplay et al. [58]. Positive angles and joint velocity represent dorsiflexion while negative values represent plantarflexion.

3.4 Decoupled Mechanism Description

Making a harvesting device which both generates energy and reduces metabolic cost is challenging because high power harvesters comprise of big DC motors and metal gearbox that

are known to be heavyweight components. Therefore, it is necessary to look at apparel that one uses every day and harvester can be integrated within this apparel. This chapter describes an ankle motion decoupled energy harvester which is located within the shoe sole and harvests energy from the single limb support of the stance phase.

The decoupled ankle harvester consists of a torsional spring which is wound at foot when its flat and until heel-off of the stance phase, Figure 3.3. The torsional spring is held by weight applied to an engaging lever, and released at heel off by two compression springs as shown in Figure 3.4.

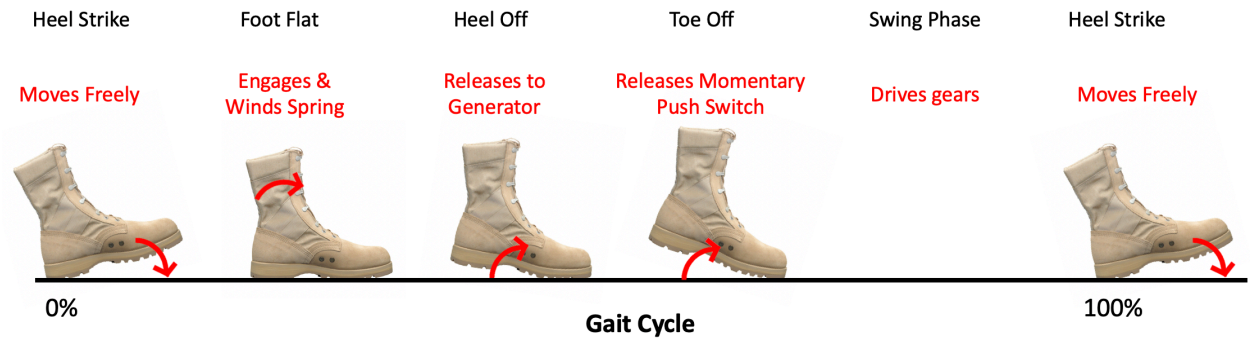

Figure 3.3- Description of when the decoupled mechanism stores and releases energy during the gait cycle.

Figure 3.4A illustrates the other major parts of the in sole mechanism. This includes lateral gearbox to amplify the ankle motion, clutch A which holds the spring from not winding back, and clutch B which releases the mechanical energy stored in the torsional spring into the medial gearbox that spins the small generator. The engaging pawl is activated during the heel strike event and released during the heel off event with the use of two locking springs. The stiffness of the locking springs was picked to be 240 kN/m since McMahon and Greene [59] showed that a stiffness range of 160–320 kN/m will make runners 2-3% faster while not changing their gait movements. Kerdok et al.[60] have shown that a compliant rebound would provide a reduction in metabolic rate. The lateral gearbox is connected to a timing belt which is driven by the shank

rotation from the ankle joint as shown in Figure 3.4B. In order to not harvest energy during the swing motion, a momentary push switch is needed to be included in the frontal part of the sole so that the generator is connected electrically when the foot is on the ground and is disconnected during the toe off event.

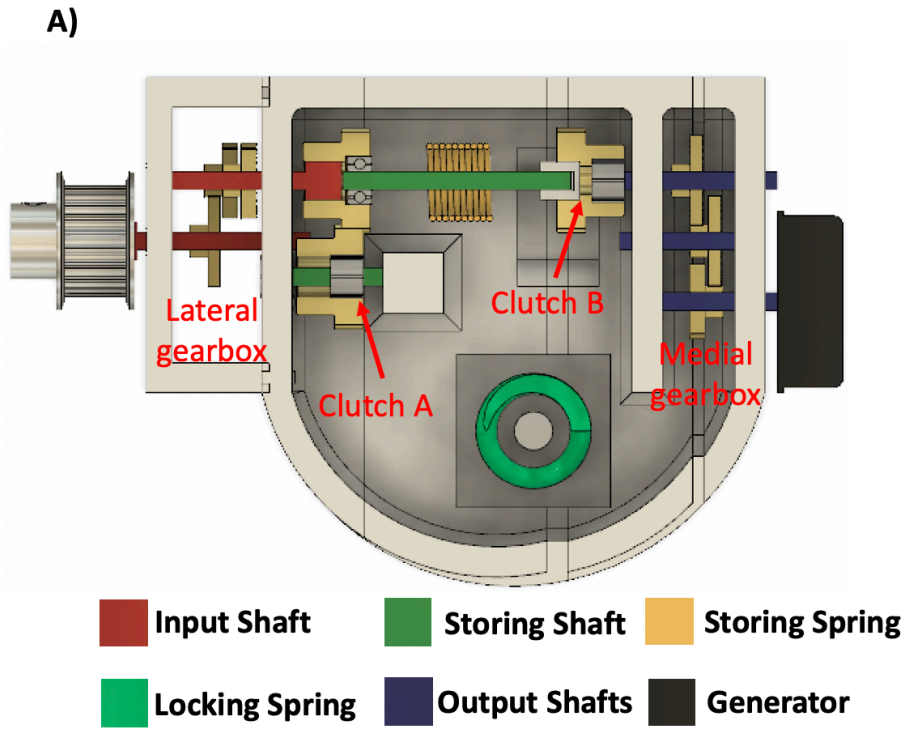

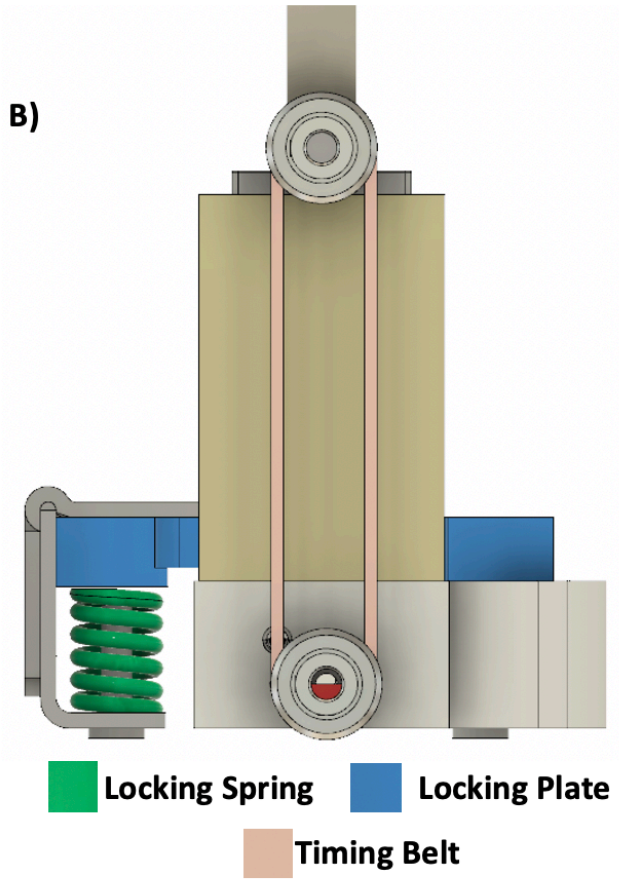

Figure 3.4- A) Major components of the decoupled boot harvester. B) Lateral view of the housing and timing belt that translates ankle motion rotation to the sole.

The complete assembly of the sole harvester is shown in Figure 3.5 in three different views along with full assembly. The figure presents a generator and gearbox that is extruded medial and lateral, respectively. This permits more space for the inner gears, engaging rack and spring assembly inside the heel sole.

Figure 3.5- Right back and left views from boot harvester excluding timing belt assembly, and full assembly of the energy harvester.

Since the weight of the components is critical to not increase metabolic rate and to not alter walking patterns, the design was built so that the total mass of the harvester was evenly separated into left and right side, as shown in Figure 3.6A. By comparing the total mass of the harvester (555.0 grams) to the original weight of the heel material in boots (82.8 grams), the amount of extra weight of the device is found to be 472.2 grams. This is in the range of the passive exoskeletons built by Collins et al. [35], 408 grams to 503 grams, for a shoe size of 8 and 13, respectively.

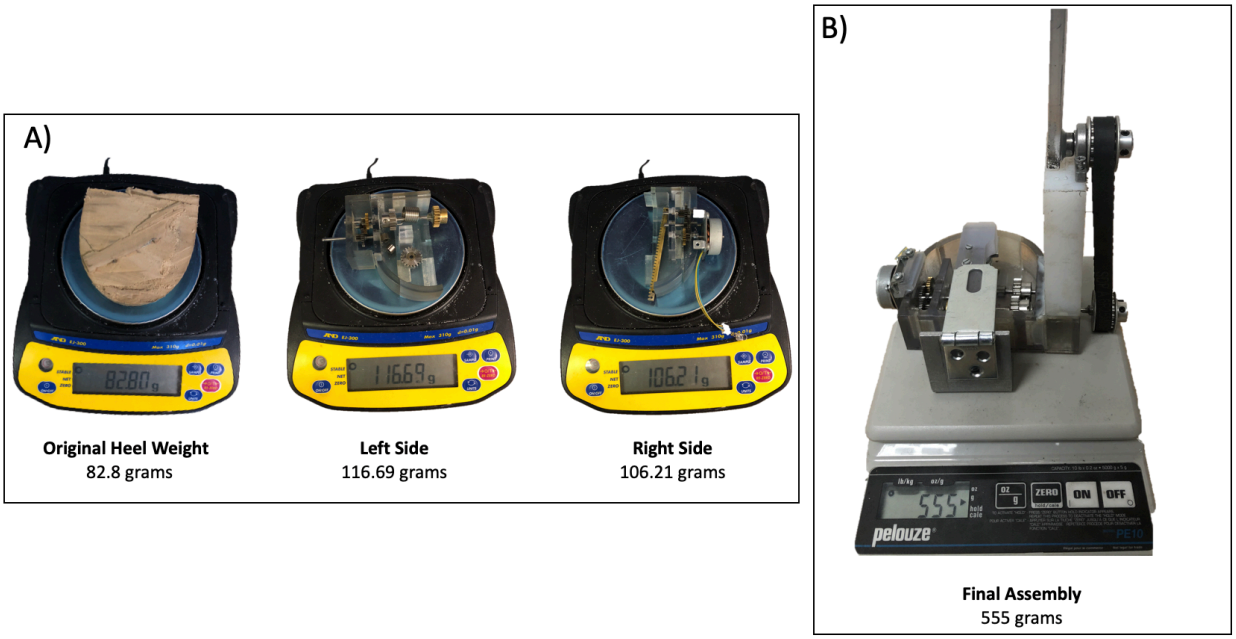

Figure 3.6- A) Weight of original heel materials and left/right sides of harvester. B) Total weight of assembly.

3.5 Methods

A bench top testing rig was developed to evaluate the torque needed to wind up a torsional spring in a decoupled harvester. Data from a semi-decoupled harvester, which generates electrical energy only in dorsiflexion motions, and a decoupled energy harvester were compared to analyze the performance features.

3.5.1 Experimental Setup

A benchtop setup was designed to control the torque and speed of moving the heel harvester at the desired degrees for semi-decoupled and decoupled mechanisms. From these tests the torque needed to wind different torsional springs, power and efficiency for a semi-decoupled and decoupled harvester were recorded. Figure 3.7 and 3.8 display the different components used in the benchtop setup for each of the systems.

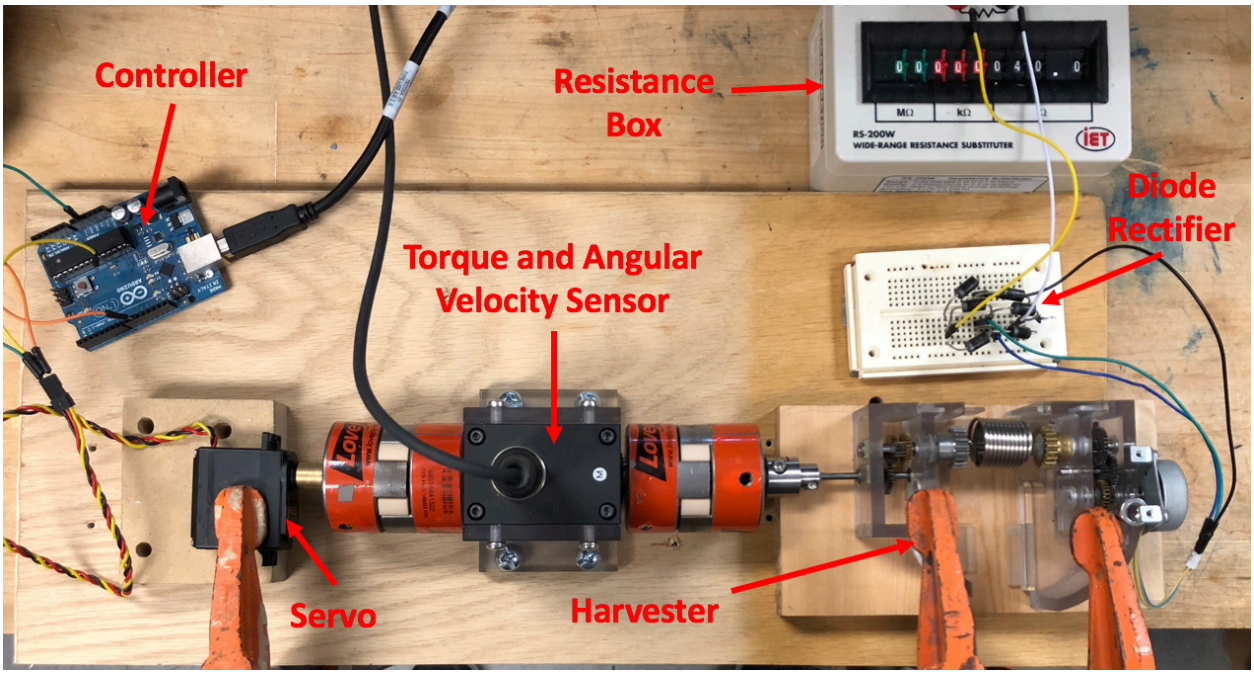

Figure 3.7- Benchtop setup for spring torque and average output power for semi-decoupled harvester.

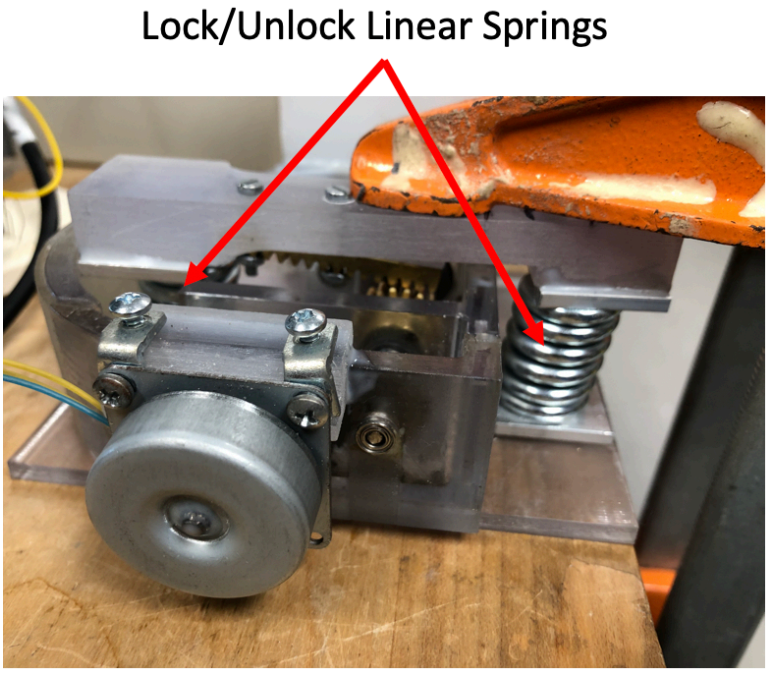

Figure 3.8- The benchtop test for the decoupled harvester had the same components shown in Figure 3.7 and locking/unlocking springs to store/release the energy in the torsional spring.

3.6 Experimental Results

Electric generators were benchmarked using a similar setup as shown in Figure 3.7, where the servomotor was changed to a DC motor and harvester was changed to an electric generator. The specific motor constants were found for six different electromagnetic harvesters. The characteristics of the selected generator are shown in Table 3.1.

Table 3.1- Selected generator parameters.

Parameter	Units	Value
Voltage constant	V/rad/s	0.065
Optimal resistance	Ohms	100
Torque constant	A/Nm	1.04
Rotor Inertia	Kg m^2	9.77E-04
Internal resistance	Ohms	38

Using the benchtop setup shown in Figure 3.7, the maximum torque generated by the spring without a gearbox is shown in Figure 3.9. Above 2.5 turns, 14.85 radians, the spring started to deform, therefore, a gearbox that amplified the number of turns below 2.5 was needed. From the slope in Figure 3.9, one can see that the spring stiffness is ~0.026 $\frac{Nm}{rad}$ compared to the manufacturer value of 0.027 $\frac{Nm}{rad}$. Section 3.7 describes the way to calculate the optimal stiffness of the spring in the desired assembly.

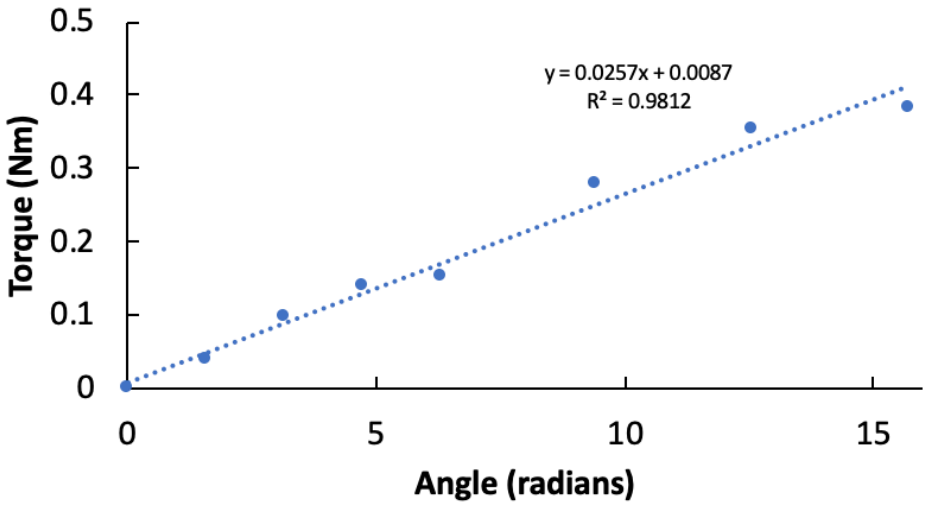

Figure 3.9- The torque vs. angle curve behaved linearly.

Despite the fact that it might take a long time to wind a spring at a specific angle or torque level, when released the energy stored in a spring is released immediately, as shown in Figure 3.10. For this reason, a gearbox is needed before a torsional spring to wind the spring as much as possible therefore increasing the torque. Moreover, a gearbox is also added after the torsional spring in order to increase the inertia of the output generator.

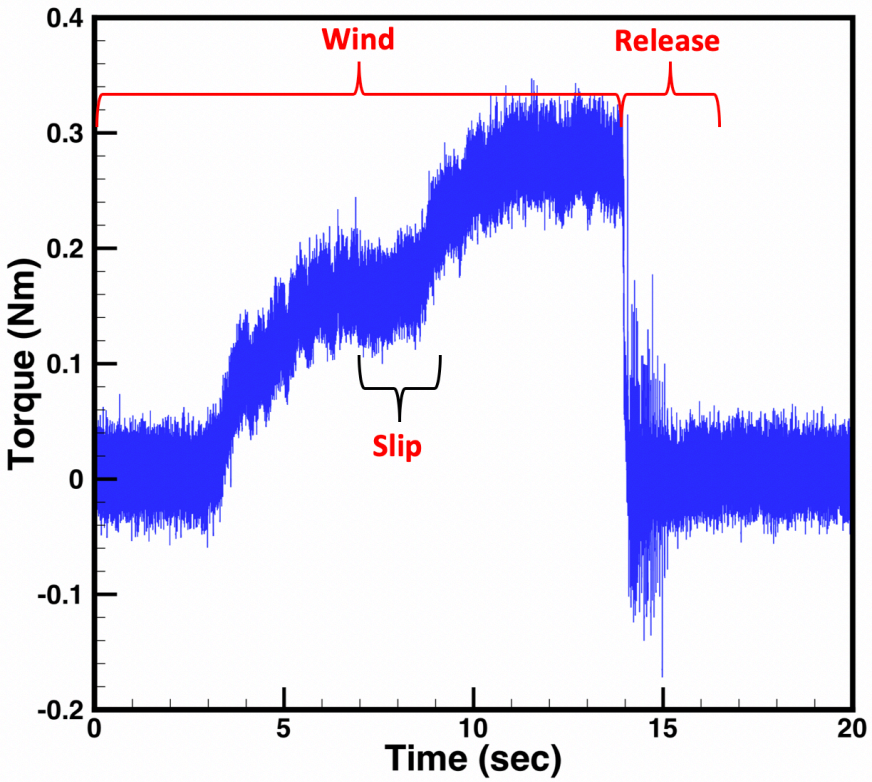

Figure 3.10- Torsional spring when wound 1.5 turns. In this figure one can see that the torque is not constant since slippage occurred when winding by hand. At the desired torque, the torque stored in the spring is immediately released in ~0.5 seconds when compared to the time it took to wind ~9.5 seconds.

Using the experimental setup shown in Figure 3.7, a semi-decoupled energy harvester with a clutch bearing was used to record the power generated at different walking speeds, as shown in Figure 3.11. Angular velocities and angles at different speeds used in this setup are shown in Figure 3.2 where torque values were divided by the constant servo torque and multiplied by the biomechanical torque in Nm/kg and motor torque constant.

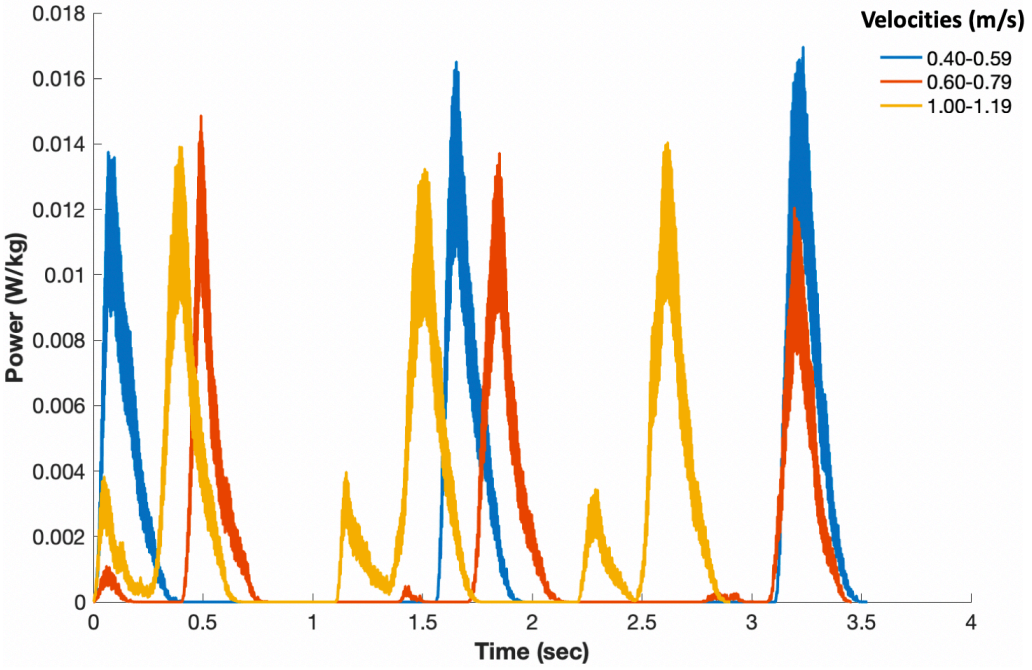

Figure 3.11- Electrical power generated at three different velocities from the experimental setup.

As shown in Figure 3.11, at slow walking velocities the instantaneous power generated is greater when compared to the instantaneous power at higher velocities. This occurs since at low velocities there is a greater range of motion in the ankle joint. However, the average power at lower speeds will be lower when compared to higher velocities since the gait cycle at lower velocities will be longer. Assuming a person mass to be 70 kg, the total average power generated by the harvester at 0.40-0.59, 0.6-0.79, 0.8-0.99, 1.00-1.19, 1.20-1.39 and 1.40-1.59 meters per second is 0.22, 0.20, 0.24, 0.26, 0.28 and 0.32 W respectively. In Figure 3.11 it can be seen that at low speed (0.40 - 0.59 m/s) one power peak is present, meaning that the power will be developed primarily during the stance phase. When walking at a faster speed (1.00 -1.19 m/s), the power generated during the swing motion dorsiflexion will contribute to the total power developed by the harvester to a point where the generator angular momentum could be conserved between the swing and stance phase. For this reason, in a decoupled mechanism a momentary

push button is needed to harvest energy only when the foot is on the ground and not feel the high damping of the generator during the swing motion.

In a decoupled mechanism, the number of turns that the spring is wound will determine the overall torque and angular velocity of the output. Similarly, in a decoupled system at low speeds one can expect a higher instantaneous power and lower average power. The decoupled harvester was wound at the different range of motions depending upon the desired speed. The walking frequency was found from the equation shown in [61]

$$v = L_s * f \tag{3.1}$$

where L_s is stride length which was found from the data presented by Peterson et al. [62]. Total gait cycle time in seconds at the different speeds is shown in Table 3.2. After finding the total angle of rotation of winding and the time of gait cycle, one can plot the different power curves for each velocity, as shown in Figure 3.12.

Table 3.2- Total gait cycle time at an average velocity.

Average velocity (m/s)	Gait Cycle Time (s)
0.5	1.5
0.7	1.35
0.9	1.2315
1.1	1.125
1.3	1.04
1.5	0.965

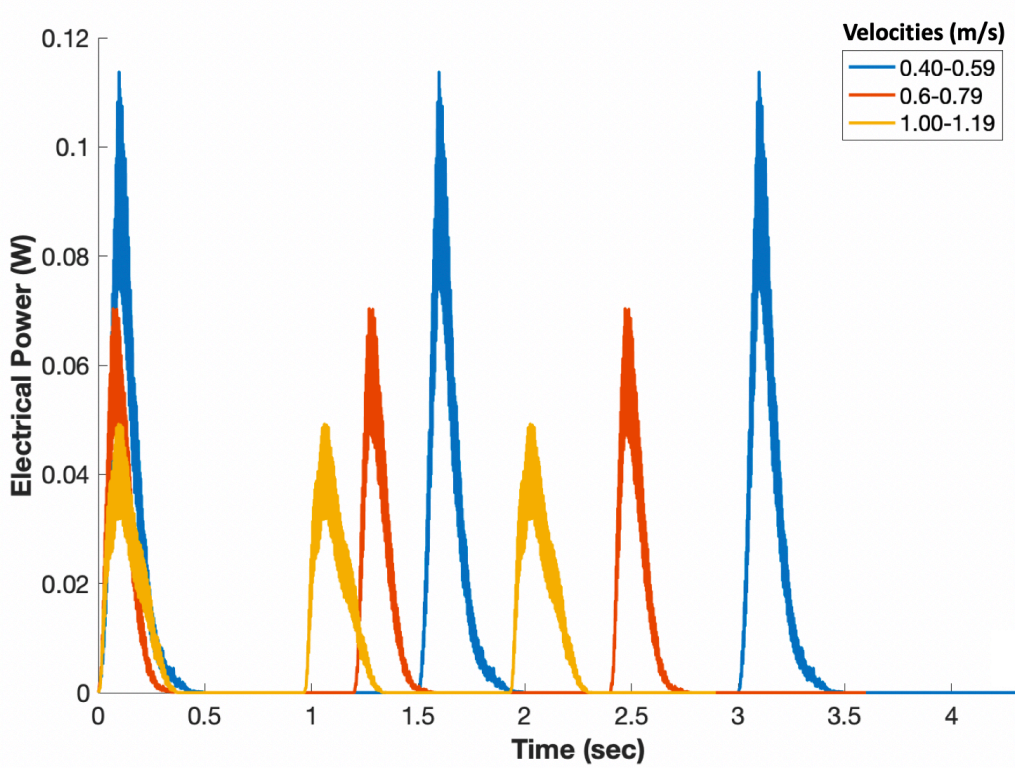

Figure 3.12- Electrical power developed by the decoupled mechanism at three different velocities.

Unexpectedly, the average electrical power developed by the harvester at lower velocities was greater when compared to the power generated at high velocities. The average power at 0.40-0.59, 0.60-0.99 and 1.00-1.19 meters per second was 0.027, 0.017 and 0.015 W, respectively. The reason that this phenomenon happens is because at lower velocities there is a higher range of motion on the ankle therefore increasing the energy held in the spring. In Section 3.7, models of the semi-decoupled and decoupled systems are shown. An explanation is provided for why output power is higher at slower velocities in decoupled systems while higher at faster velocities in a semi-decoupled system.

3.7 Modeling of Shoe Sole Harvester

3.7.1 Shoe Sole Semi-decoupled Harvester

To find the maximum power from an energy harvester, biomechanical data from Bovi et al. [63] is used to find the input displacements and torques at the ankle joint. The ankle displacement and torque are represented mathematically using a polynomial fit with an equation in form of

$$f(x) = \sum_{i=0}^{n} p_i x^{n-i} \tag{3.2}$$

where p_i are the different polynomial coefficients. An almost perfect mathematical polynomial fit of the ankle displacement and torque is seen whenever the mathematical expression has 22 different coefficients as shown in Figure 3.8A and C. Information on the polynomial coefficient equations are shown in Appendix A.

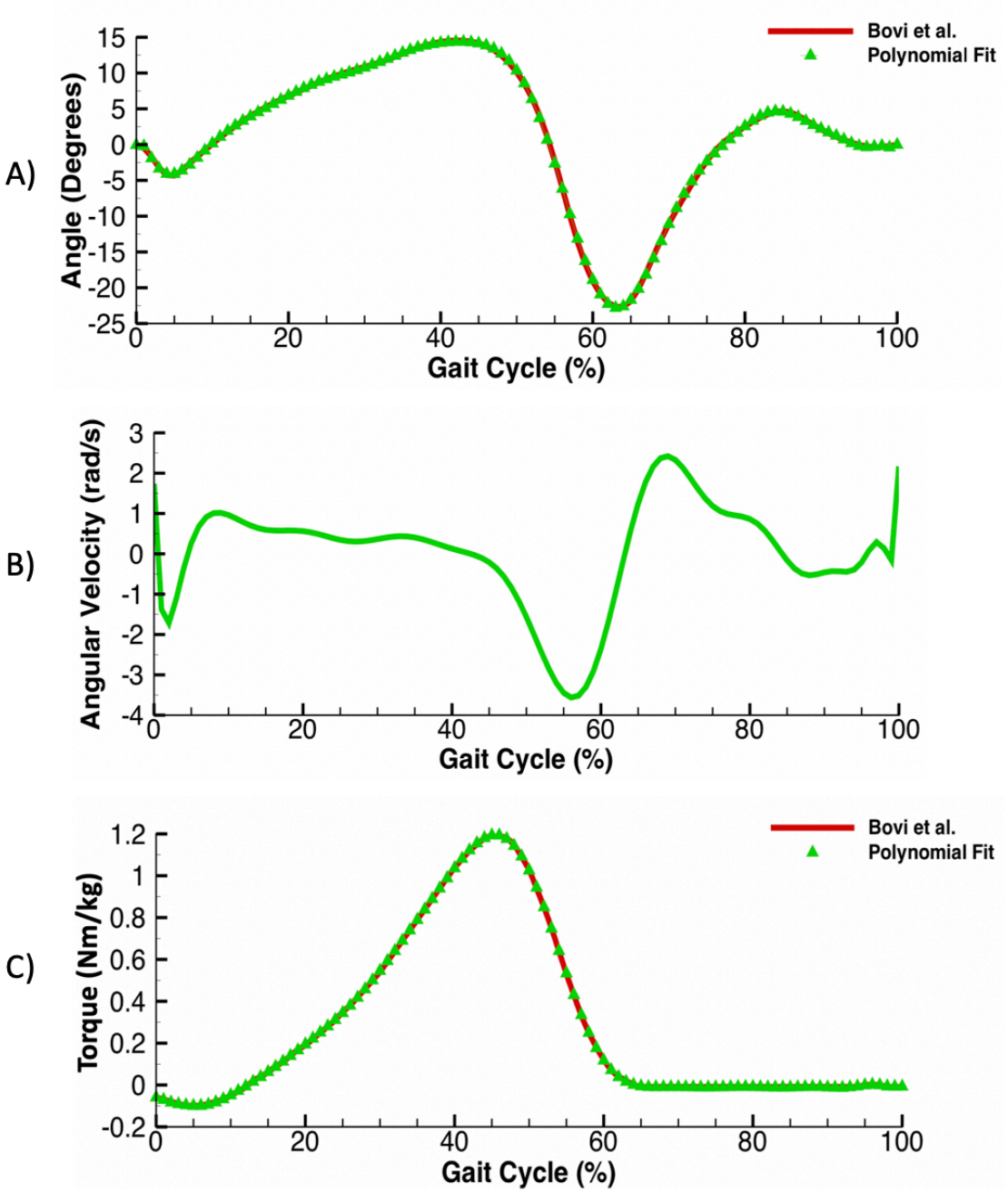

Figure 3.13- A) Comparison of polynomial ankle range of motion with data from Bovi et al. [63] B) Derived velocity from ankle motion polynomial fit. C) Comparison of ankle torque polynomial fit with Bovi et al.[63] data.

Having the polynomial equation of the ankle, one can derive the ankle displacement polynomial with respect to *x,* percentage of gait cycle, to find the angular velocity in radians per second during the gait cycle (Figure 3.13B). This angular velocity can then be multiplied by the

torque polynomial shown in Figure 3.13C to find the equation for the biomechanical power during the gait cycle (Appendix A), as shown in Figure 3.14.

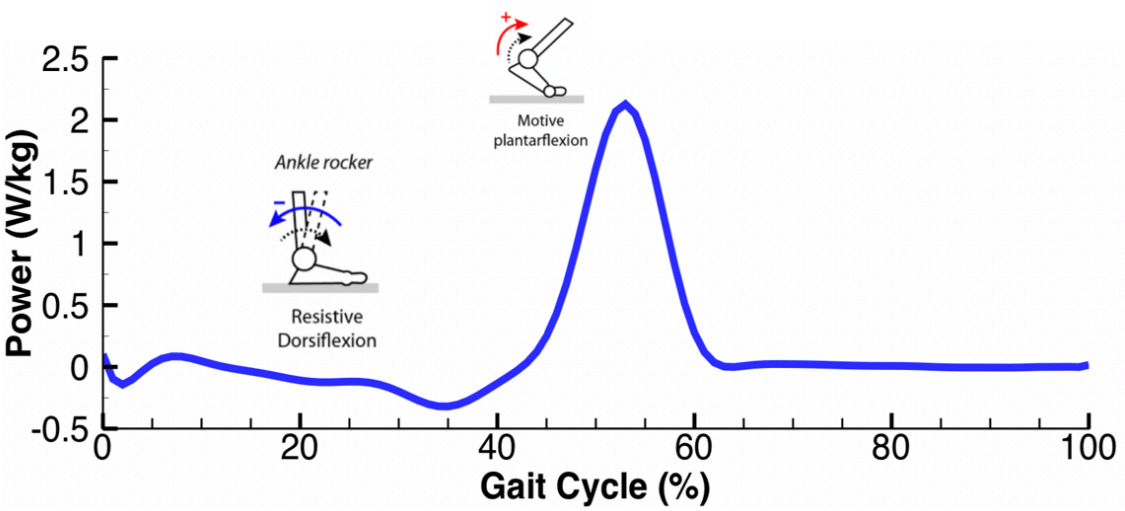

Figure 3.14- Modeled biomechanical power at the ankle from torque polynomial fit and displacement derivation.

Since the biomechanical input torque and velocity is known, the electrical power of a semi-decoupled system can be calculated by using the generator torque and speed constants, K_t and K_s, as shown in Table 3.1. The angular velocity at the generator is multiplied while the torque is divided by the gear ratio, *r*, of both medial and lateral gearboxes whose total value is 67.5. Assuming the weight of the person is 70 kg, the plot of electrical power per stride is shown in Figure 3.15. A large power signal occurred during the dorsiflexion motion in the stance phase while a smaller signal during the dorsiflexion in the swing phase. The average power developed by the model is 0.3387 W at 0.40 - 0.59 m/s. It is expected that the contribution during the swing phase will increase while the power generated during the stance phase will slightly decrease at higher walking velocities.

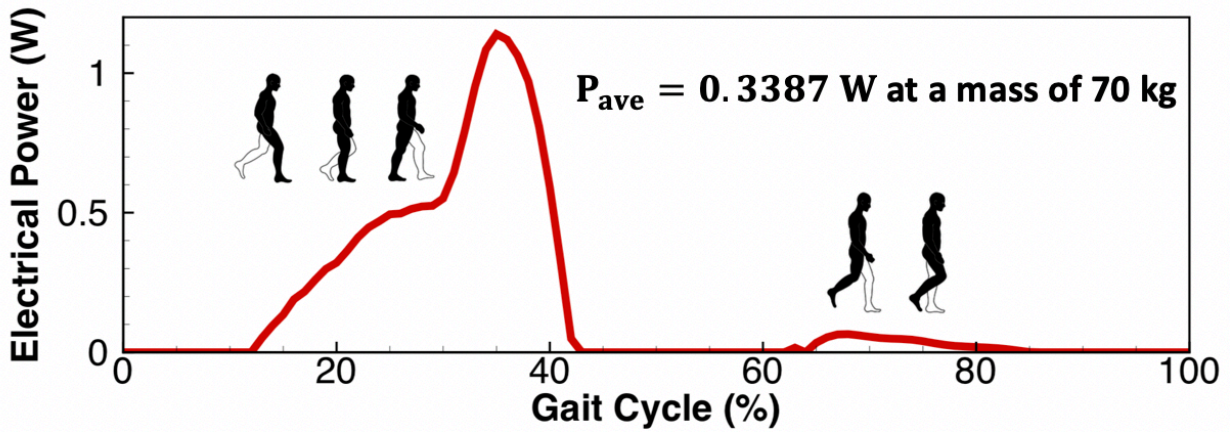

Figure 3.15- Ideal power generated from a semi-decoupled mechanism with a 1:67.5 gear ratio which is the multiplication of the lateral and medial gearboxes, assuming the mass of the person is 70 kg.

3.7.2 Shoe Sole Decoupled Harvester

In a decoupled mechanism, the winding of a spring needs to occur between 5-42% of the gait cycle and not during the swing phase. The amount of energy which can be stored in the system will be equal to

$$PE_{rot} = \frac{1}{2} q_{tors} \theta^2 \tag{3.3}$$

where q_{tors} is the torsional spring stiffness (Nm/radians) and θ is the winding angle of the spring in radians. The maximum potential energy on the torsional spring will be achieved at 42% of the gait cycle. Since the input to the system is high torque and low angular rotation, an initial gear box with a ratio (r) of 7.5 is used to amplify the amount of rotations at the spring; however, at a θ_{max} of 18.85 degrees or 0.328 radians, the input torque from the ankle needs to be greater than the spring torque. Moreover, the mechanical designing factor in this system is what determines the maximum amount of torque that can be applied to the housing. The components that will hold the torque of the torsional spring, one-way clutches and engaging/disengaging rack system, needed to be evaluated. In this particular configuration the maximum torque allowed by the one-way clutch bearing is 2 N.m. Since the housing of the mechanism is build out of low weight

plastic, a safety factor of 4 is used in making the maximum input torque at the timing belt (Figure 3.4B) to be 0.5 N.m. The maximum torque acting on the spring is found by multiplying the input torque by $\frac{1}{r}$ or 0.067 N.m. To find the maximum stiffness needed in the design, Hooke's law needs to be applied:

$$\tau_{max} = q_{rot} * \theta_{max} \tag{3.4}$$

where τ_{max} is 0.067 Nm and θ_{max} is 0.328r or 2.46 radians. As a result, the maximum rotational stiffness of the spring is 0.027 $\frac{Nm}{rad}$. The potential energy stored in the spring as a percent of the proposed gait cycle is shown in Figure 3.16.

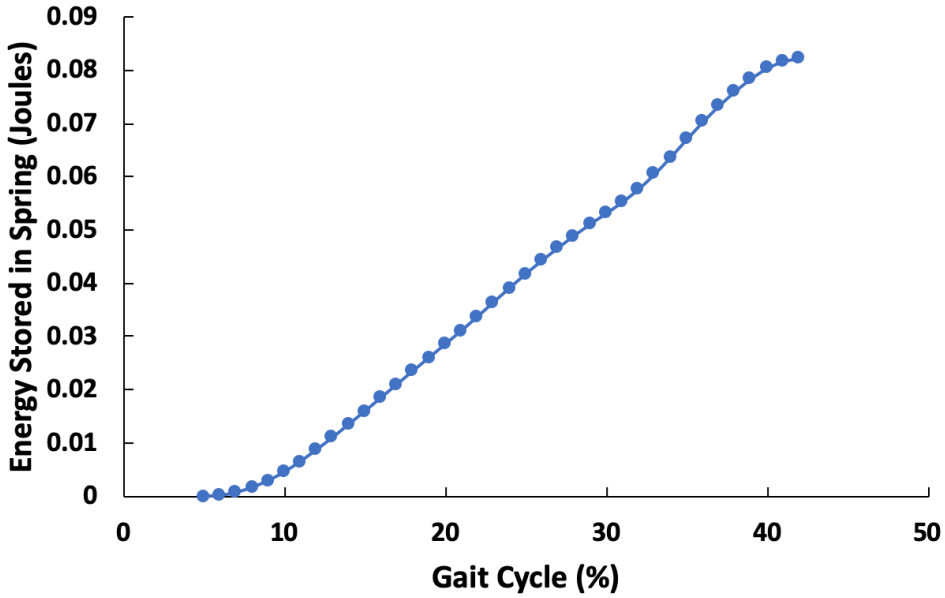

Figure 3.16- Stored potential energy during the targeted gait cycle.

The fraction of energy that will be stored in the spring compared to the input energy can be calculated by the equation:

$$Spring\ storage\ efficiency = \frac{0.5\ q_{rot}\ \theta}{\tau_{in}\ m_p} \tag{3.5}$$

where the torque τ_{in} is the input torque from the ankle in Nm/kg and $m_p$represents the mass of the person in kg. Furthermore, it is important to know that the input biomechanical energy from

the wearer will be dependent on the angular velocity of the ankle or velocity of walking. The energy stored on a decoupled spring system is dependent on the angular rotation of the spring. Ideally if the wearer ankle range of motion is the same during walking, the spring will store the same mechanical energy in the spring at different walking velocities.

When releasing the energy stored in the spring the torque on the system behaves as shown in Figure 3.10. The behavior of the torque released can be modeled by the equation

$$\tau\,(t) = \tau_{max} e^{-\frac{c_m}{J_{eq}}t} \tag{3.6}$$

where τ_{max} is the torque when the spring begins to release or the torque at θ_{max}, c_m is mechanical damping and J_{eq} is the rotational inertia of the spring assembly. The inertia was found by adding all the components along the spring axis and medial gearbox inertia.

$$J_{eq} = J_{spring} + J_{gearbox} + J_{shaft} \tag{3.7}$$

This resulted in a value of $3.3 * 10^{-5} kgm^2$ while the mechanical damping was found to be ~0.0003 $\frac{Nm\ s}{rad}$. Once the output torque from the spring is known, the angular velocity of the system can be found from the differential equation

$$J_{out}\ddot{\theta} = \tau(t) - c_e\dot{\theta} \tag{3.8}$$

where J_{out} is the inertia of the generator rotor (Table 3.1) and c_e the damping coefficient of the generator which is governed by the equation given in [64]

$$c_e = \frac{k_t k_s}{R_i + R_l} \tag{3.9}$$

where k_t denotes the torsional constant of the motor in $\frac{Nm}{A}$, k_s is the speed constant in $\frac{V}{rad/s}$, R_i is the internal resistance and R_l is the external resistance in Ω as shown in Table 3.1. The total torque, angular velocity and expected electrical power of the model is shown in Figure 3.17.

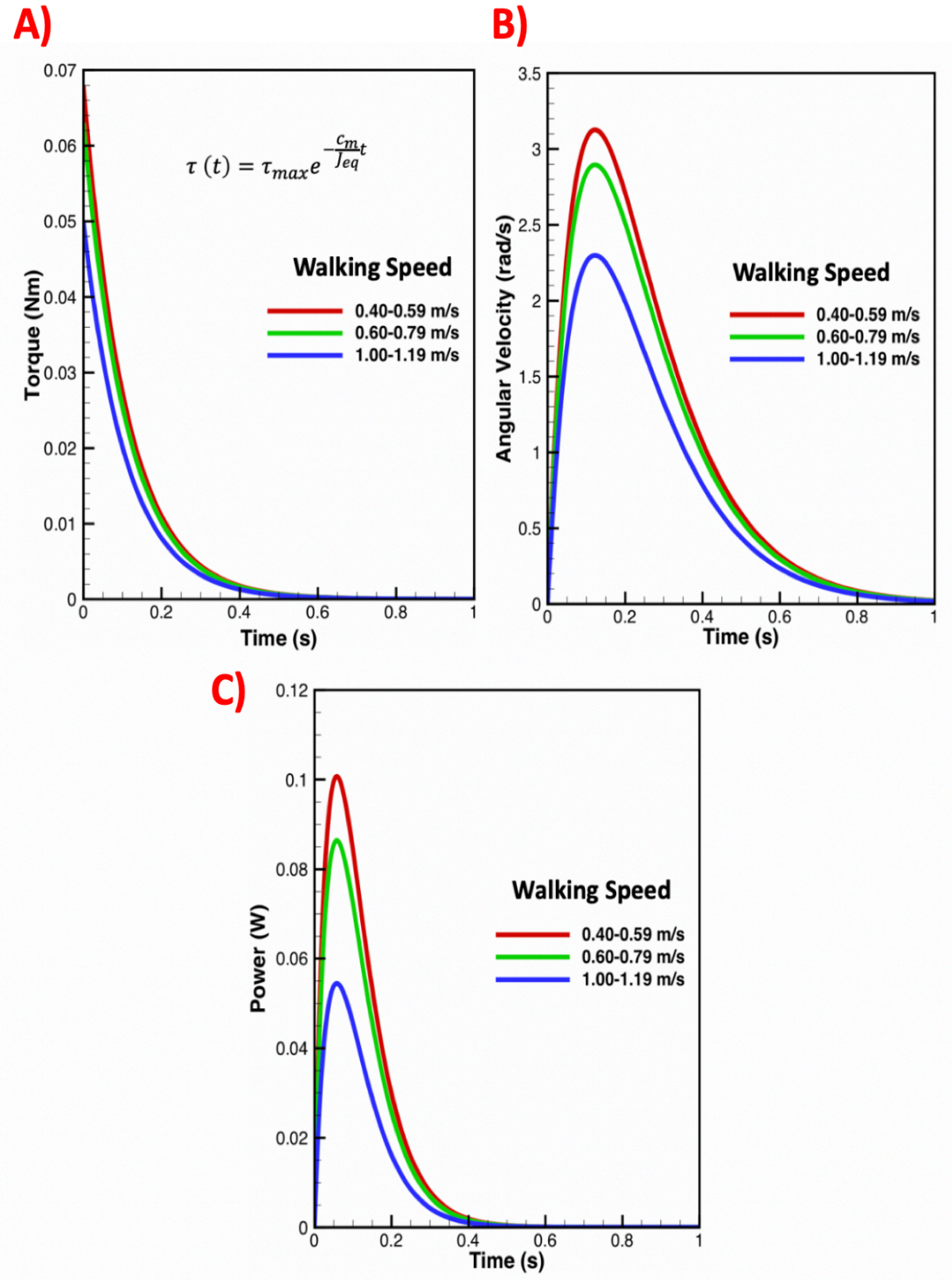

Figure 3.17- A) Torque released by the torsional spring after been wound during the stance phase. B) Angular velocity of the electromagnetic generator. C) Total power generated by the harvester after releasing the spring.

As expected from the experimental results, the power generated during slower velocities is higher than the power generated at faster velocities since the system is mostly dependent on the amount of winds in the torsional spring or range of motion of the ankle and not on the ankle angular velocity. To increase the output electrical power of the proposed harvester one could either increased the total amount of turns, decrease the damping of the system or increase the inertia of the lateral gearbox and generator. However, when increasing the number of turns, a higher torque will be experienced by the inner components and housing of the harvester. While the increase of inertia will make the system bulky and difficult to carry at the ankle joint. Therefore, the ankle generator and lateral gearbox assembly would need to be moved closer to the body center of mass so it decreases the effects on the wearer. Future work on the shoe sole energy harvester is described in Chapter 6.

Chapter 4 Hybrid Energy Harvester Capturing Body Heat and Arm Swing Motion

4.1 Introduction

In this chapter, a wearable dual energy harvester was modeled, built and tested to simultaneously capture energy from body heat and motion. The possibility of integrating a thermoelectric generator (TEG), thermomagnetic generator (TMG) and a pendulum on a single device is evaluated. The TEG is designed to maximize the output power at low temperature differentials by optimizing the heat transfer equations. A combination of TMG and pendulum is designed to be activated during motion which converts arm swing mechanical energy into electrical energy. Finally, the optimization of a TMG at low and high temperature differentials is evaluated for standalone applications.

4.2 Review of Wristband Energy Harvesters

In this section, multiple technologies that could harvest energy by a small differential in temperature or arm swing movement are discussed. These same technologies could be used for standalone applications if a system has a temperature gradient or a change in motion.

4.2.1 Thermoelctric Generators

Thermoelectric generators (TEGs) are solid state devices which can convert a temperature differential into electrical energy. TEGs are governed by three different effects called the Seebeck, Peltier and Thomson effects. The Seebeck effect states that as two sides of a thermocouple material are placed at different temperatures a voltage will be produced proportional to the temperature difference. Multiple materials can be evaluated according to their thermopower or Seebeck coefficient *S* given as [65]:

$$S = -\frac{\Delta V}{\Delta T} \tag{4.1}$$

On the other hand, the Peltier effect is the reverse of the Seebeck effect which states that an electrical current which passes through thermocouple materials will produce a difference in temperature in their junctions, as shown in Figure 4.1.

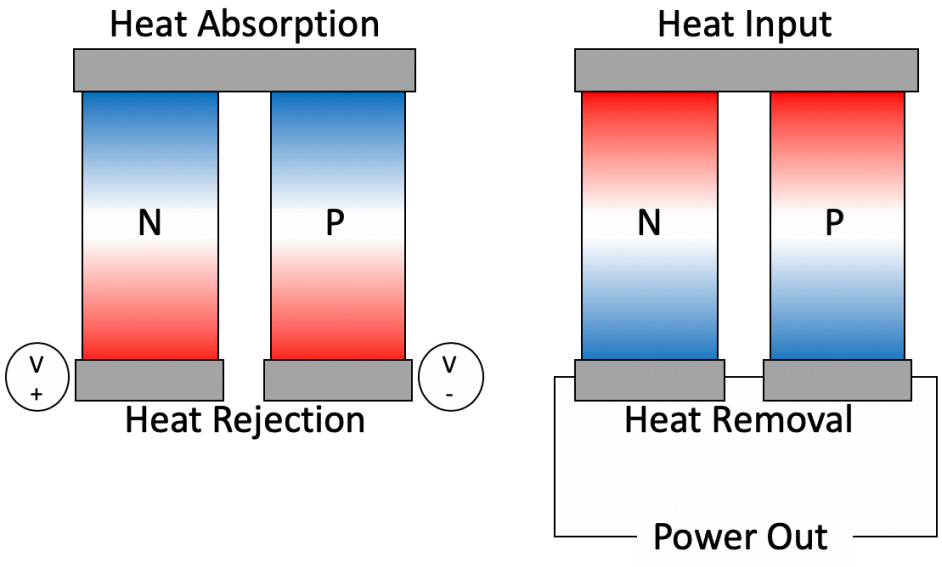

Figure 4.1- (Left) Peltier Effect. An external voltage flow through P and N type materials generates a hot and cold side. (Right) Seebeck Effect. External temperatures create a charge gradient in the material, as a result, generating electrical power.

Finally, the Thomson effect happens when a current flow through a heated conductor where energy is absorbed or evolved. The overall voltage generated by a TEG module is expressed by the equation [65]

$$V = 2nS\Delta T - R_i I \tag{4.2}$$

where ΔT is the temperature across the hot and cold surface, R_i internal resistance of the TEG module, n the number of couples and I the current flowing. Nowadays, the figure of merit that governs thermoelectric material efficiency to generate power is expressed as ([66], [67]) :

$$ZT = \frac{S^2 \sigma T}{k} \tag{4.3}$$

where σ is electrical conductivity, T is temperature and k is the thermal conductivity. Since a thermoelectric module consist of two materials (n-type and p-type) an average ZT value is expressed as ([66], [67]):

$$\overline{ZT} = \frac{\left(S_p - S_n\right)^2 T_{ave}}{\left((\rho_n \kappa_n)^{0.5} + \left(\rho_p \kappa_p\right)^{0.5}\right)^2} \tag{4.4}$$

where ρ is electrical resistivity. As a result, the maximum efficiency of the whole TEG module based on the two materials can be calculated as ([66], [67]):

$$n = \frac{T_H - T_C}{T_H} \frac{\sqrt{1 + \overline{ZT}} - 1}{\sqrt{1 + \overline{ZT}} + \frac{T_C}{T_H}}. \tag{4.5}$$

Using these equations, multiple researchers have focused on increasing the ZT with material engineering and microstructure design.

4.2.2 Arm Motion Energy Harvesters

Energy harvesting from human arm motion can be divided into three different categories: eccentric mass microgenerators, piezoelectric rotors, and electromagnetic harvesters. One of the well-known harvester designs consists of an eccentric mass that is excited by the arm swing motion. This technology was demonstrated by Kitahara at SEIKO [68] and the prototype was able to generate 5-10 μW of average power. Just like eccentric mass microgenerators, piezoelectric rotors consists of magnetic rotor which excites a piezoelectric cantilever beam ([52],[53]). Recently, work from Yeo et al. [69] has shown that low frequency arm motion converted into high frequency vibrations (100-200Hz) during jogging can generate an output power of 38.3-156.6 μW. Electromagnetic harvesters are governed by electromagnetic induction of levitating magnets that are excited by human motion and move through a coil to create a voltage differential. [24]. This concept was later implemented by Halim et al. [70] by using

springs with a magnetic tip mass that were excited by a moving nonmagnetic mass, and were able to generate 2.15 mW of power at a 5 Hz vibrational frequency.

4.2.3 Thermomagnetic Harvesters

Thermomagnetic mechanism relies on ferromagnetic materials that when heated above a certain temperature lose their magnetic properties and become paramagnetic. The temperature at which material changes from ferromagnetic to paramagnetic is called the Curie temperature. Recently, Kishore et al. [71] developed a thermomagnetic energy harvester that generated 105 $\mu W\ cm^{-3}$ at temperature gradients of 2 ^{o}C. This harvester design consisted of a rotating gadolinium wheel which transitioned between ferromagnetic and paramagnetic state while moving through the hot water reservoir at 24 ^{o}C. Chun et al. ([72], [73]) demonstrated a harvester comprising of a piezoelectric beam with a gadolinium tip mass. This harvester was shown to oscillate at signal frequencies up to 9 Hz and generate maximum power of 80 μW at a temperature difference of 60 ^{o}C. Chen et al. [74] developed a miniature piezoelectric beam whose hot side was a magnet at room temperature and cold side iced water. At a different of 20 ^{o}C they were able to generate a power of 62.9 pW/cm^3.

4.3 Gadolinium Material Review

Gadolinium is paramagnetic at room temperature with a ferromagnetic Curie point of about 20°C ([75],[76],[77]). Therefore, when the gadolinium temperature rises above 20°C the material starts losing magnetic properties (Figure 4.2).

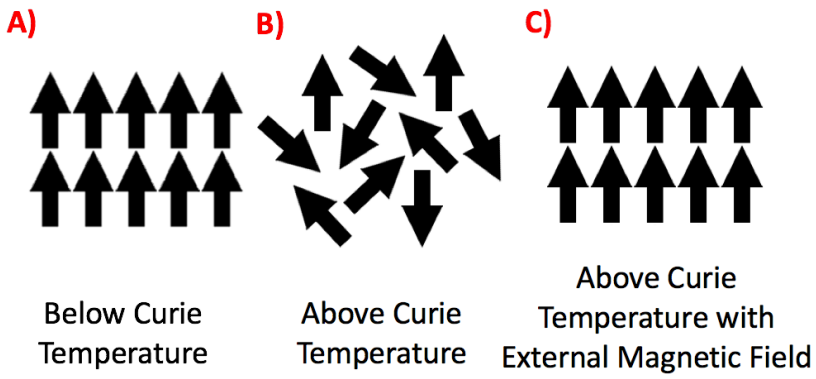

Figure 4.2- A) Below 20 ºC gadolinium retains its magnetic properties. B) Above 20 ºC, gadolinium starts losing its magnetic properties. C) Hot gadolinium exhibits magnetic properties when a large external magnetic field is applied.

The magnetic properties of gadolinium make it an ideal candidate to harvest energy at low heat gradients, especially in wearable devices since room temperature is generally around 20-22°C, body temperature is about 37°C and the skin temperature is 2.5°C lower than body temperature [78].

4.4 Arm Swing Biomechanical Review

During gait cycle, humans swing their arms in conjunction with the motion of the opposite leg. This compensates from the one-sided moment created by the lower limbs and results in balancing of the body when moving [79]. At low speeds of approximately 0.8 m/s there is slower arm movement swing since not much moment is created by the legs, resulting in frequency ratio of 2:1 between arm and leg motions ([80],[81]). At higher walking speeds, higher than 0.8 m/s, arm swing increases and synchronizes with the leg walking frequency with a frequency ratio of 1:1 between arm and leg movements ([80],[81]). When walking on a treadmill, Ford et al. [82] demonstrated that the arm amplitude of rotation increases with velocity as shown in Table 4.1.

Table 4.1 Walking on a treadmill at different velocities vs. arm amplitude in degrees.

Treadmill Velocity (m/s)	Arm Amplitude (degrees)
0.22	4.22
0.40	7.36
0.63	11.16
0.85	16.30
1.10	22.91
1.30	27.01

4.5 Mechanism Description

A typical configuration for a TEG is shown in Figure 4.3a. This wearable device consists of a heatsink on top of a TEG module. Normally, a heatsink is used to increase the difference in temperature across the module; therefore, increasing the output power. Using the same volume, Figure 4.3b shows the first iteration of the hybrid energy harvester which consists of case enclosing a cantilever piezoelectric beam with a gadolinium tip mass and a fixed permanent magnet which serves as components for the TMG on top of the same TEG module. In Figure 4.3b, a baseplate in form of an array of fins serves as the cold side of the TEG module while the hot side is on top of the skin. The use of these spreaders to act as a heatsink has been shown by Hyland et al. [83], mainly for wearable applications to reduce the total volume of energy harvesters.

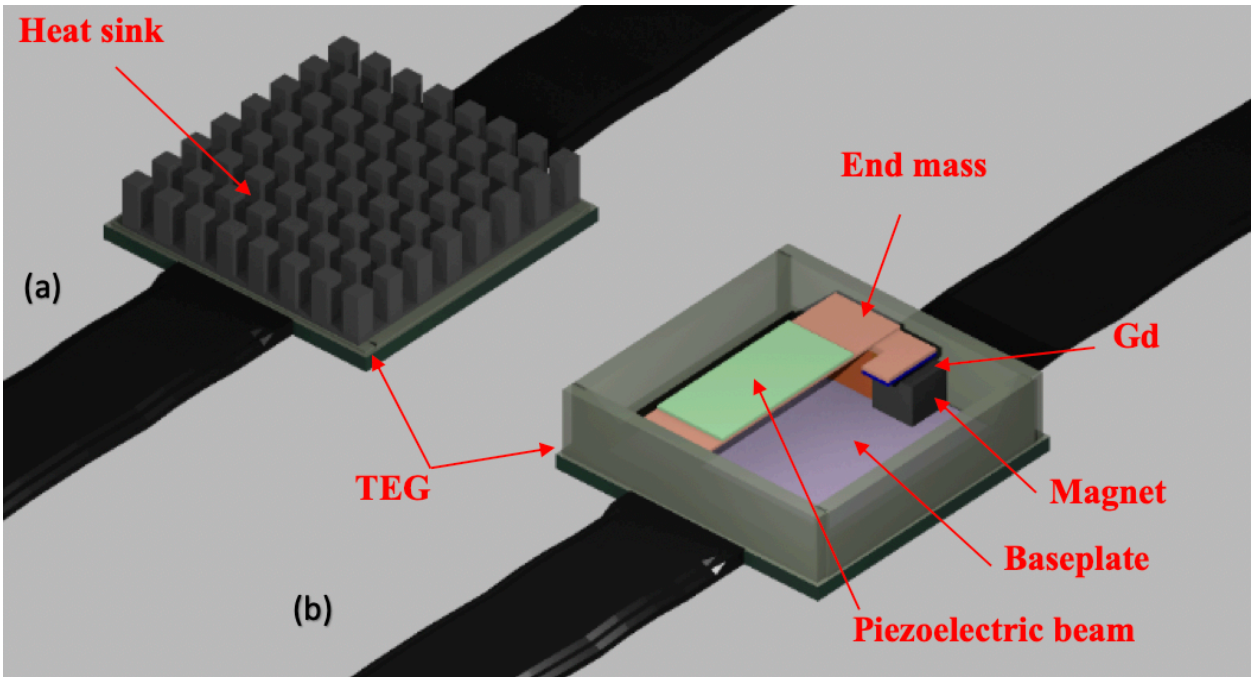

Figure 4.3- (a) A TEG and heatsink assembly. (b) Proposed TEG and TMG hybrid assembly.

While the hybrid harvester is at ambient temperature, the gadolinium tip mass will be attracted to the permanent magnet. As gadolinium touches the hot magnet, it transitions from ferromagnetic to paramagnetic state and loses its magnetic properties. As a result, the cantilever beam will move back to original state, cool down in ambient temperature and become ferromagnetic again. In parallel, TEG is harvesting energy from the change in temperature from the body heat and heat spreader temperature. This cycle keeps on repeating as long as the heat transfer occurs through the gadolinium, thereby generating power from the thermomagnetic piezoelectric beam and TEG. During motion, the power is amplified through the external convection from the air into the harvester.

A second device was fabricated consisting of a pendulum magnet that amplifies the power generated at rest and motion as shown in Figure 4.4.

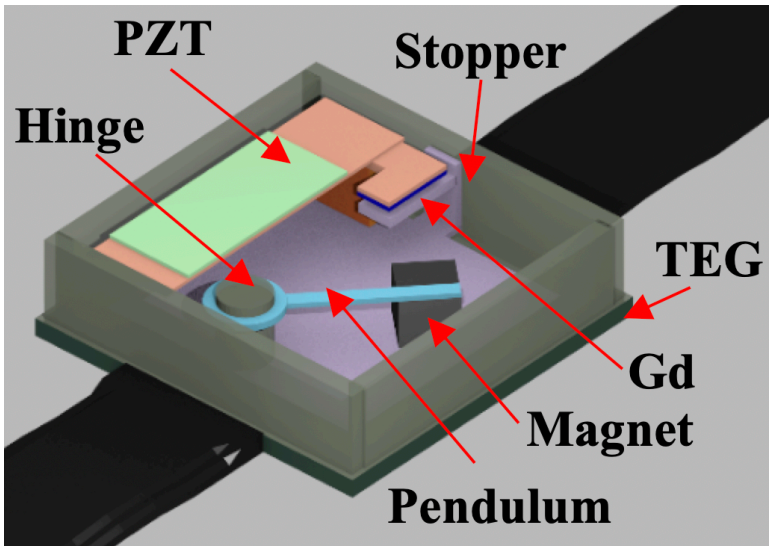

Figure 4.4- Revised TEG and TMG pendulum assembly.

At rest, the permanent magnet on the pendulum attracts the gadolinium. In this configuration, the gadolinium is not touching the low thermal conductivity neodymium permanent magnet ~17 W/mK, but the high thermal conductivity aluminum stopper ~205 W/mK. During motion, the arm swing frequency dictates the frequency at which the piezoelectric beam moves up or down. In motion, the gadolinium is only used for its magnetic properties and not for its phase transition.

4.6 Optimization of Thermoelectric Generator

The average power produced from the harvesters shown in Figure 4.3 and 4.4 depends on multiple parameters including ambient temperature, thermoelectric leg geometry, thermoelectric material properties, overall surface area, skin temperature and heat transfer coefficients. In order to try to optimize these values, a convenient approach to lump multiple parameters into fewer groups is described in this section.

As shown in Figure 4.1, a TEG consists of alternating n-type and p-type materials connected in series that results in two output terminals generating the voltage difference. A TEG module with a heatsink is shown in Figure 4.5.

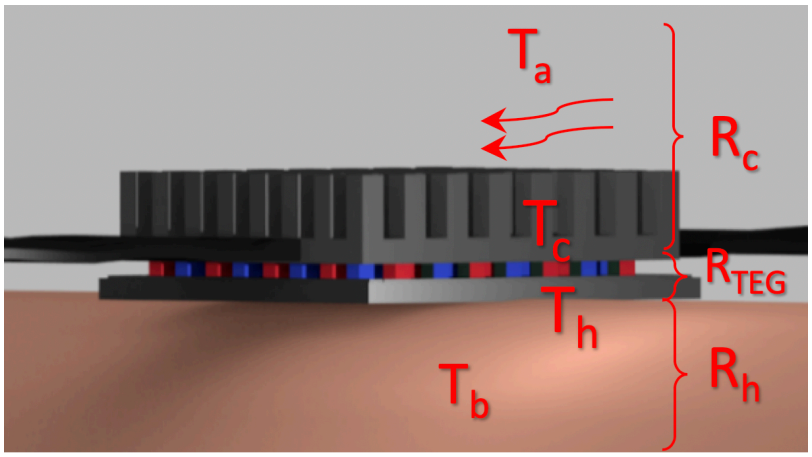

Figure 4.5- Representation of a TEG harvester consisting of p and n type materials shown in red and blue colors, respectively.

The temperature at the hot junction of the system is the temperature from body denoted as T_b while the cold junction is the ambient temperature denoted as T_a. However, the actual difference of temperature of the module which generated the temperature differential is lower than the difference of the extrinsic temperatures. In Figure 4.5, the intrinsic temperatures of the module are shown as T_c and T_h for hot and cold temperatures at the junctions. In a module, three different thermal resistances are established. R_h represents the thermal resistance of the interface between the skin and the hot junction. R_c represents the thermal resistance of the ambient air and heat since. Finally, R_{TEG} represents the thermal resistance of the thermoelectric material used in the module.

To derive the equations governing a TEG module, Lineyking et al. [84] show that a module can be represented as a 1-D electrical circuit as shown in Figure 4.6.

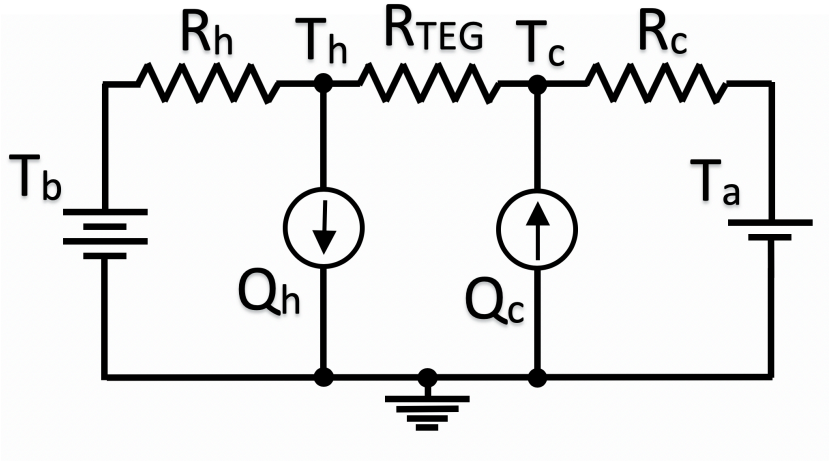

Figure 4.6- Lumped circuit diagram of a TEG module.

The heat flux at the hot and cold junctions is represented as current flows Q_h and Q_c. This heat flux includes the effects of Joule heating Q_j and Peltier heating/cooling effects $Q_{pc/h}$. The heat loss at the hot junction is given by

$$Q_{ph} - Q_J/2 \tag{4.6}$$

while the heat gained at the cold junction is described as

$$Q_{pc} + Q_j/2 \tag{4.7}$$

where the Peltier heating and cooling effects are governed by the equation

$$Q_{pc/h} = S\, n\, T_{c/h}\, I \tag{4.8}$$

where n is the number of TEG couples in the TEG module. On the other hand, the joule heating could be expressed as

$$Q_j = I^2 R_{elec} \tag{4.9}$$

where R_{elec} is the internal electrical resistance of the TEG module. In an ideal scenario, no current flow could be considered ($Q_h = Q_c = 0$). Therefore, the intrinsic temperatures across a TEG module could be expressed as a ratio of resistance times the extrinsic temperature difference

$$\delta T = T_h - T_c = \frac{R_{TEG}(T_b - T_a)}{R_h + R_{TEG} + R_c} \tag{4.10}$$

R_c, R_{TEG} and R_h can be represented as $1/h_c A_o$, $t/A_r A_0 k$ and $1/h_h A_o$, where $h_c, h_h, A_r, A_0, t \; and \; k$ are heat transfer coefficient of cold and hot, area ratio between the area of the thermoelectric legs and total area, nominal area, thickness and thermal conductivity of legs respectively.

However, the presence of current flow in the system decreases the intrinsic temperature difference. Adopting the procedure used by Shiho [85] the intrinsic temperature is given by

$$\Delta T_{int} = \delta T - \frac{R_{TEG}\, S\, n\, L_i}{(R_h + R_{TEG} + R_c)^2} I \tag{4.11}$$

where L_i is defined as

$$L_i = T_a[R_h(R_c + R_h) + R_c R_{TEG}] + T_b[R_c(R_c + R_h) + R_h R_{TEG}]. \tag{4.12}$$

For simplicity Eqn. 4.12 can be represented as $\Delta T_{int} = \delta T - b_o I$. To find the power developed by the module one can represent the module as shown in Figure 4.7.

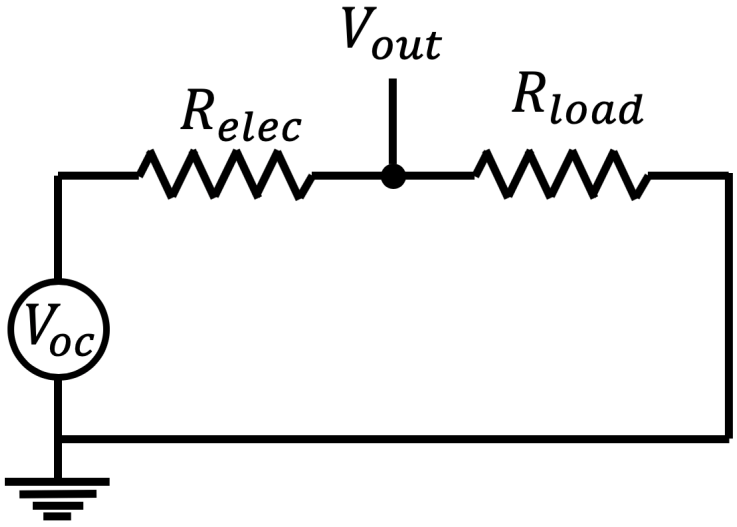

Figure 4.7- Overall circuit of the TEG module where V_{oc} represent the voltage coming from the TEG module while V_{out} is the voltage across the internal electrical resistance.

Eqn. 4.2 expresses the formula for V_{out}. In Eqn. 4.2 one can substitute ΔT by ΔT_{int} or $\delta t - b_O I$. As a result, one will get the equation

$$V_{out} = 2nS(\delta \mathrm{T} - \mathrm{b_o} I) - IR_{elec} \tag{4.13}$$

this equation can be simplified as

$$V_{out} = \frac{2\ n\ S\ \delta T\ R_{load}}{R_{load}+R_{elec}+b_o\ 2\ n\ S} \tag{4.14}$$

from V_{out}, one can find the output electrical power by applying Eqn. 1.3 in Chapter 1. As a result, one gets the TEG power equation

$$P_{TEG} = \frac{4\ n^2\ S^2\ \delta T^2\ R_{load}}{(R_{elec}+R_{load}+b_o 2nS)^2}\ . \tag{4.15}$$

As shown in Eqn. 4.15, the power developed by the TEG module depends on electrical resistance, thermal resistance, intrinsic and extrinsic temperature, material Seebeck coefficient, module area and number of couples. To find the optimal resistance to maximize power, Eqn. 4.15 is differentiated by R_{load} and equaled to zero. As a result, the optimal load resistance is determined to be:

$$R_{optimal\_load} = R_{elec} + 2\ n\ S\ b_o. \tag{4.16}$$

The expression in Eqn. 4.15 is rewritten to optimize power according to the area of the TEG by considering five different variables: heat transfer coefficients (*H*), extrinsic temperatures (*T*), thermoelectric material (*M*), nominal area (*A*) and power (*P*), as shown in Eqn. 4.17.

$$P_{TEG} = H\ T\ M\ A\ P \tag{4.17}$$

where

$$H = \frac{h_c h_h}{h_c + h_h} \tag{4.18}$$

$$T = (T_b - T_a)^2 \tag{4.19}$$

$$M = \frac{S^2}{\rho k} \tag{4.20}$$

$$A = A_O \tag{4.21}$$

$$P = \frac{\beta}{2[(RT_1 + \beta RT_2) + 2(1+\beta)^2]} \tag{4.22}$$

The power factor represented as P is defined as the ratio of the TEG power, P_{TEG} to the product of H, T, M and A factors. The power factor is dependent on three dimensionless ratios

$$RT_1 = \frac{S^2}{\rho k}\left(\frac{h_c T_a + h_h T_b}{h_c + h_h}\right) \tag{4.23}$$

$$RT_2 = \frac{S^2}{\rho k}\left(\frac{h_h T_a + h_c T_b}{h_c + h_h}\right) \tag{4.24}$$

$$\beta = \frac{H\ t}{A_r k} \tag{4.25}$$

The dimensionless numbers RT_1 and RT_2 are similar ratios to ZT figure of merit in Eqn. 4.3; however, the RT values include heat transfer coefficients. Since the difference between the extrinsic temperatures (T_a and T_b) is small, one can assume that $RT_1 \approx RT_2 = RT$. Moreover, when $h_h \approx h_c$, RT_1 and RT_2 become the ZT figure of merit value. As a result, the P factor becomes

$$P = \frac{\beta}{2(1+\beta)(RT + 2(1+\beta)\,)} \tag{4.26}$$

If one plots the power factor (P) according to β and RT, it can be seen that the equivalent power factor has and optimum β and it decreases as RT increases in value as shown in Figure 4.8.

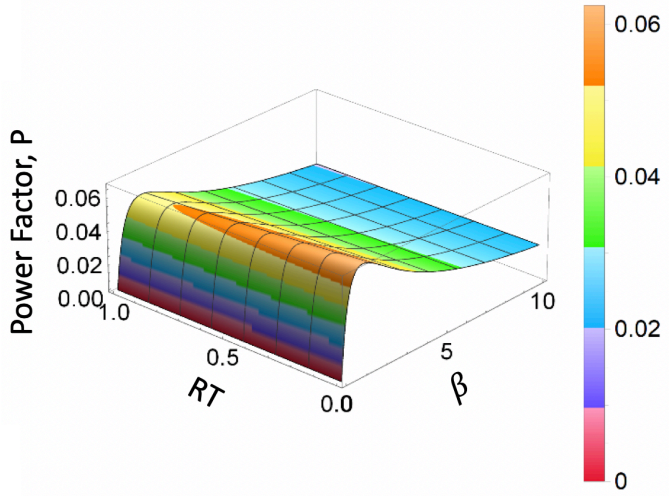

Figure 4.8- Power factor plot as a function of RT and β.

Since an optimal β point is needed to find the maximum power factor one could maximize *P* by differentiating the expression with respect to area ratio (A_r) and equating it to zero resulting in

$$A_{r\_opt} = \frac{H\ t}{k}\left(1 + \frac{RT_1}{2}\right)^{-0.5} \tag{4.27}$$

By substituting Eqn. 4.27 in Eqn. 4.26 the maximum power factor *P* is described by the equation

$$P_{max} = \frac{1}{4\left(1 + \sqrt{1 + \frac{RT}{2}}\right)^2} \tag{4.28}$$

the theoretical limit of Eqn. 4.28 is when *RT* is equal to zero resulting in $P_{max} = \frac{1}{16}$, as shown in Figure 4.8 when *RT* is zero at an optimal β.

A plot of power obtained from the TEG model according to leg thickness and area ratio is shown in Figure 4.9. The parameters used in this simulation are displayed in Table 4.2.

Table 4.2- Selected parameters for mathematical simulation of TEG.

Property	Units	Value
Body Temperature	K	309.15
Ambient Temperature	K	294.15
Hot heat transfer coefficient	W/m^2K	80
Cold heat transfer coefficient	W/m^2K	50
Thermal conductivity of legs	W/m.K	1.3
Seebeck coefficient of legs	μV/K	240
Electrical resistivity of legs	Ωμm	15
Number of thermocouples	#	72
Nominal area	cm^2	1.7
Leg thickness	mm	2

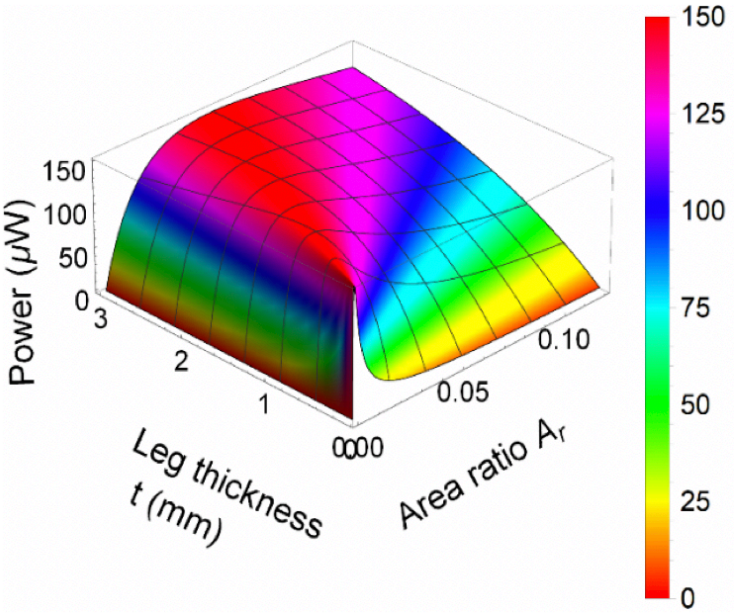

Figure 4.9- Power developed by TEG module when using the mathematical model at different leg thickness and area ratios.

In Figure 4.9, for every leg thickness there exists an optimal area ratio (Eqn. 4.27) to achieve maximum power, since optimal resistance is also dependent on leg thickness and area ratio. Figure 4.10 shows that the optimal resistance (Eqn. 4.16) increases as leg thickness increases and area ratio decreases.

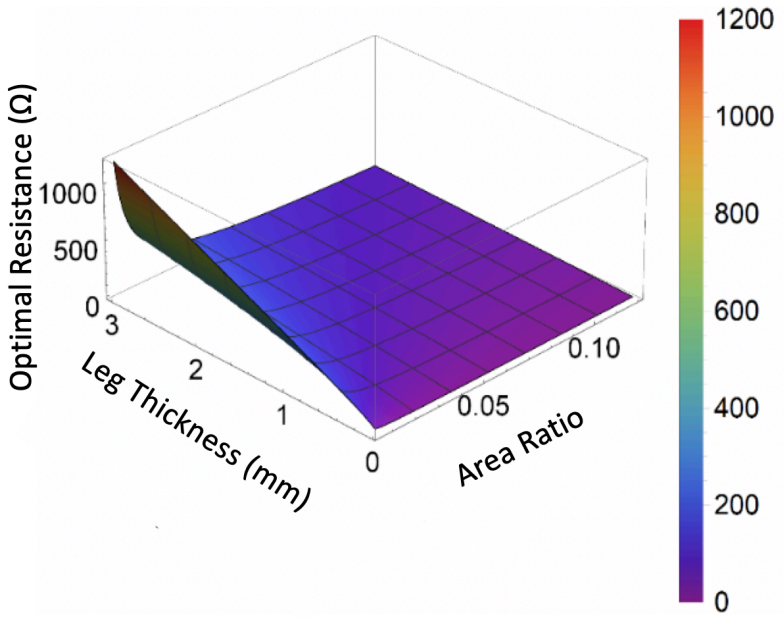

Figure 4.10- Optimal resistance at various module thickness and area ratios.

To properly compare the optimization of the TEG module and a commercial module, the same parameters as shown in Table 4.2 are used to analyze the difference between a TEG module at an optimal area ratio and a commercial module area ratio, as shown in Figure 4.11.

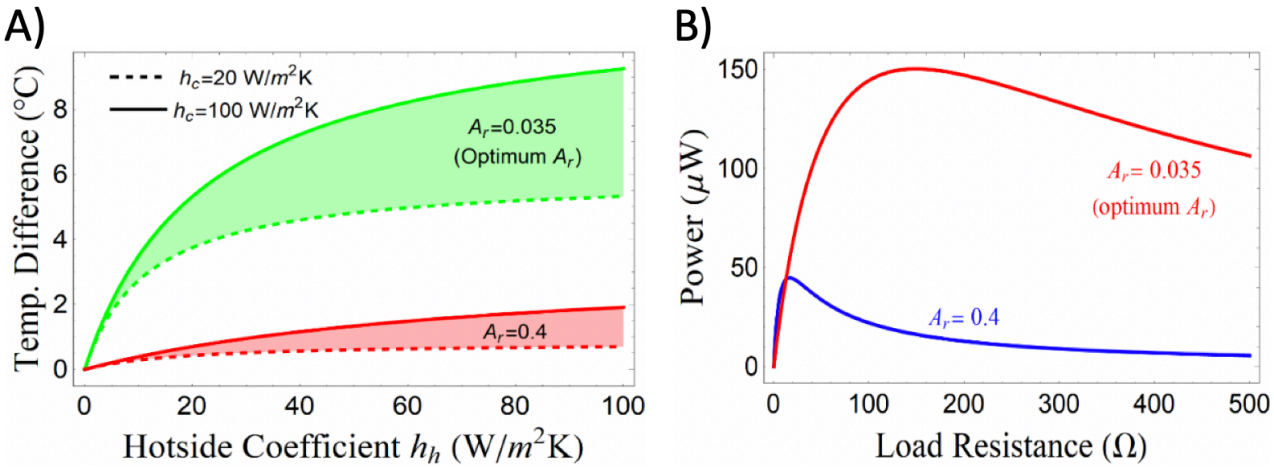

Figure 4.11- A) Intrinsic temperature difference for optimal and non-optimal area ratio. B) The total electrical power output from the TEG.

In Figure 4.11B, the total output power generated by a smaller area ratio is about three times higher when compared to a larger area ratio. The device can be improved for wearable application by using less material which will make it lightweight and less expensive when compared with traditional modules. However, the mechanical rigidity of the module needs to be considered when selecting an optimal TEG area ratio.

4.7 Thermomagnetic and Motion Harvester

In this section, the thermomagnetic generator (TMG) and motion of piezoelectric beam in the wrist harvester assembly are analyzed. In order to find the energy that can be harvested from the piezoelectric movement one needs to calculate the total mechanical energy in the system. The mechanical energy of the device is represented on a bench top stand as shown in Figure 4.12.

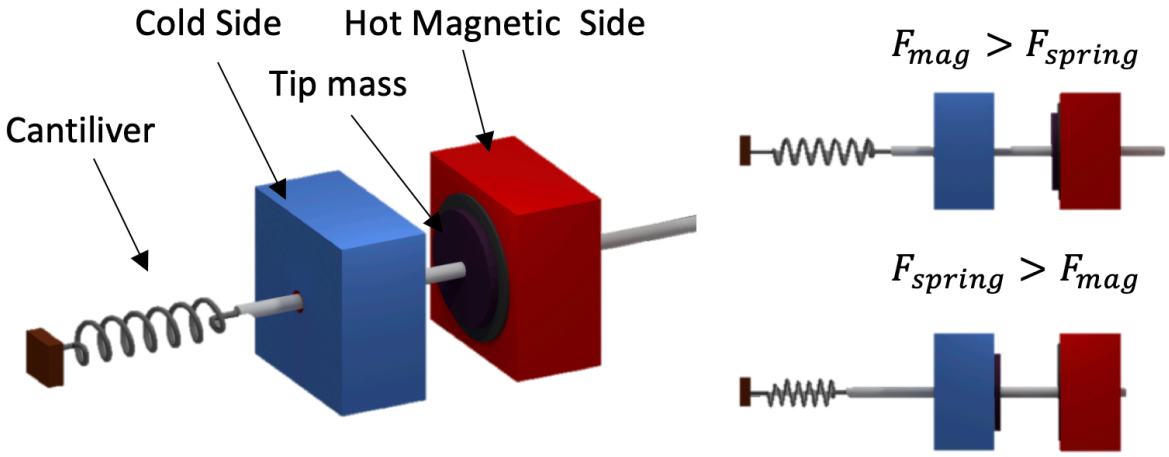

Figure 4.12- Representation of cantilever thermomagnetic beam in linear form. When the gadolinium is below its Curie temperature it will be attracted to the hot magnet. However, when its above Curie temperature the spring or cantilever beam will push the tip mass back to the cold side.

In the scenario shown above, mechanical energy can be calculated by finding the magnetic and thermal properties of gadolinium tip mass across the cold and hot side gap. The

magnetic properties of gadolinium are measured by using a vibrating sample magnetometer (VSM) and shown in Figure 4.13.

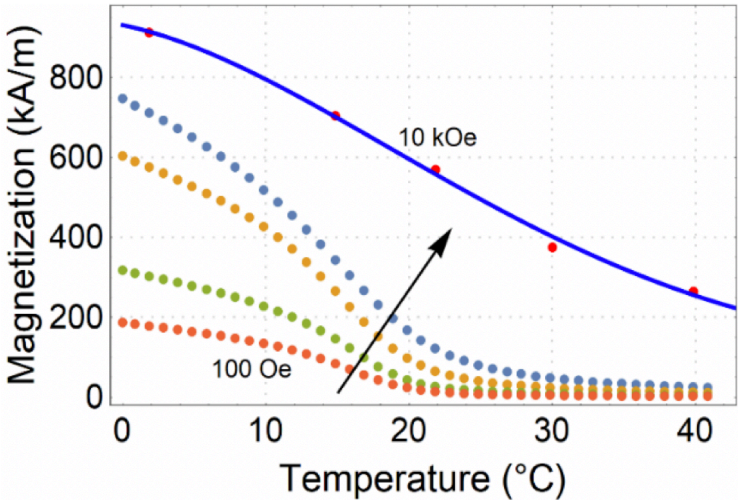

Figure 4.13- Gadolinium magnetization as a function of temperature and external magnetic field density.

As gadolinium crosses its Curie temperature point, the magnetization of the materials gets closer to zero. However, if the external field acting on the gadolinium is large the material will still hold magnetization at high temperatures. The cycle of interest for the material is along two magnetization lines and temperatures as shown in Figure 4.14.

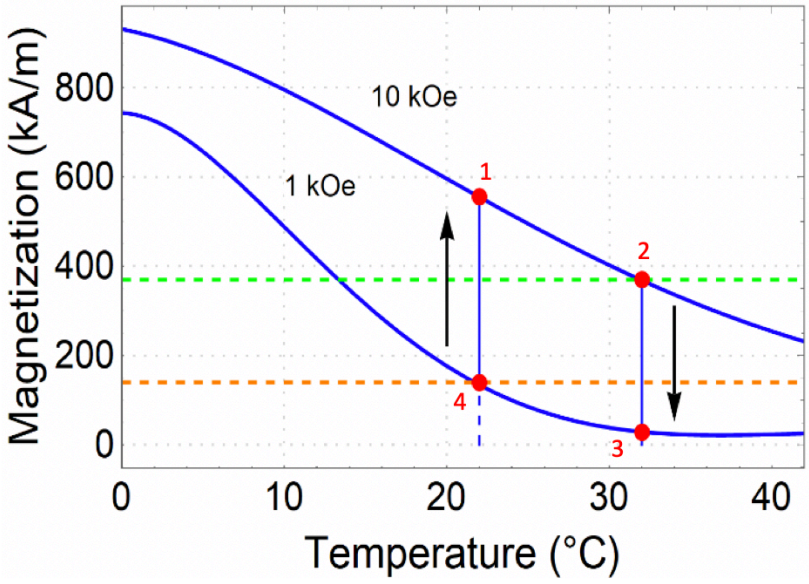

Figure 4.14- A typical cycle of gadolinium at intrinsic hot (32 Celsius) and cold (22 Celsius) temperatures. At (1) the gadolinium attaches to the hot magnet and then increases in temperature therefore decreasing magnetization and arriving at (2). Then, the force in the spring brings the gadolinium away from the magnet to the cold surface (3). Over time, the gadolinium will decrease in temperature and arrive at (4). Finally, the gadolinium will magnetize and attract to the hot magnet to (1).

To achieve a higher mechanical power in the system the transient heating/cooling of the gadolinium needs to be considered since this will dictate the frequency of oscillation. A typical heating profile of gadolinium is shown in Figure 4.15. The simulated response of the heat profile can be represented by an exponential equation [86] as shown

$$T_h - \Delta T \exp(-\alpha t) \tag{4.29}$$

where $\alpha = 0.15\ s^{-1}$ and $\Delta T = 33$ °C.

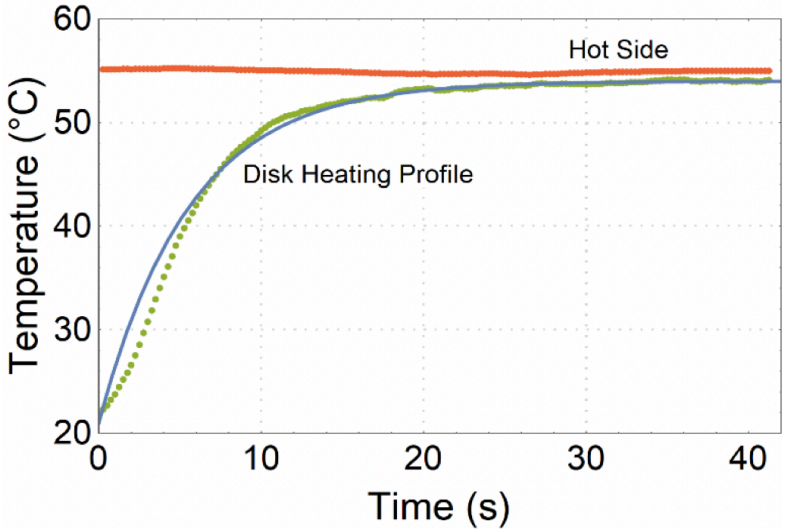

Figure 4.15- Experimental and modeled heat profile of gadolinium with a hot source temperature of 54 °C.

Using the thermal time constant α the thermal transient response of gadolinium can be represented with the desired hot and cold temperature limits. As shown in Figure 4.16, it can be seen that the material takes about 20 seconds to reach 95% of the temperature limit.

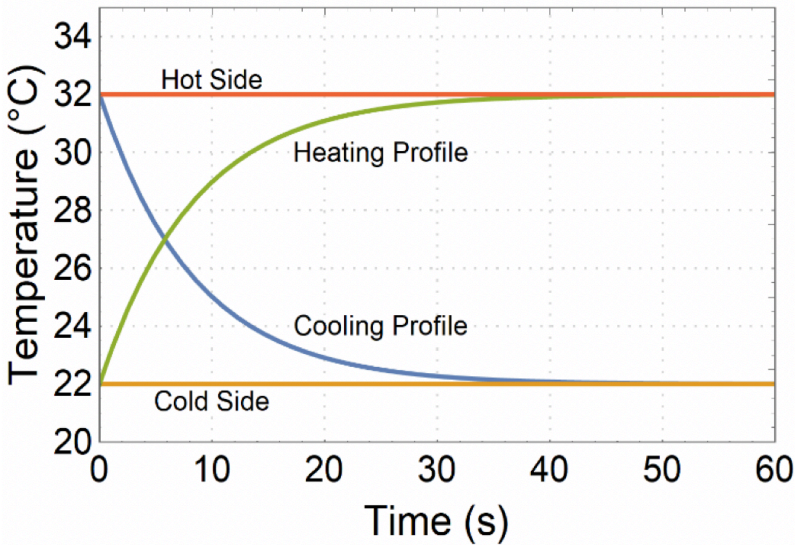

Figure 4.16- Heating and cooling profiles of gadolinium at intrinsic body and ambient temperatures.

However, the energy is only harvested when the material is in motion between the hot and cold reservoirs. When the gadolinium is in motion, the acceleration of the material is governed by the cantilever beam stiffness *k*, force of attraction *F* and gadolinium tip mass *m*. Where the force of attraction is dependent on gap distance and magnetization $F(z, M)$, and magnetization on magnetic field and temperature $M(H, T)$. Moreover, the cantilever force can be represented as the stiffness *k* times distance *z*. Neglecting damping in the system, the governing differential equation during the thermomagnetic cycle can be expressed as:

$$m\ddot{z} = F\big(z, M(H,T)\big) - k(z_o + z) \tag{4.30}$$

where $F\big(z, M(H,T)\big)$ can be expressed as [87]:

$$F\big(z, M(H,T)\big) = M(H,T) * V_{Gd} * \mu_o * \frac{dH(z)}{dz} \tag{4.31}$$

Where μ_o is the permeability of free space, V_{Gd} is the volume of the gadolinium tip mass and $H(z)$ is expressed by Joshi et al. [87] as:

$$H(z) = \frac{M_s}{\pi}\left[\tan^{-1}\left(\frac{(z+L)\sqrt{a^2+b^2+(z+L)^2}}{ab}\right) - \tan^{-1}\left(\frac{z\sqrt{a^2+b^2+z^2}}{ab}\right)\right] \tag{4.32}$$

where M_s is the magnet coercivity of the neodymium magnet, 2a, 2b, L are the width, length and thickness of the permanent magnet. The parameters used in the TMG modeling are shown in Table 4.3.

Table 4.3- Selected parameters for mathematical thermomagnetic simulation.

Property	Units	Value
Body Temperature	K	305.15
Ambient Temperature	K	295.15
Magnet coercivity	kA/m	680
Magnet cube side length	mm	6.35
Gd thickness	mm	0.3
Gd contact area	mm^2	25
Gap between hot and cold side	mm	2
Stiffness of spring	N/m	80
Initial spring elongation	mm	0.5
End mass of beam	grams	6.3
Pendulum	grams	5.3
Pendulum arm length	mm	22

The displacement and velocity response of the model is shown in Figure 4.17. As expected, it takes about 20 seconds for the material to transition from hot to cold, however, the amount of time of movement where mechanical energy can be harvest is 0.02 seconds. Moreover, Figure 4.17C shows that gadolinium will have a greater velocity when traveling from cold side to hot magnet (1) than traveling from hot magnet to cold side (3).

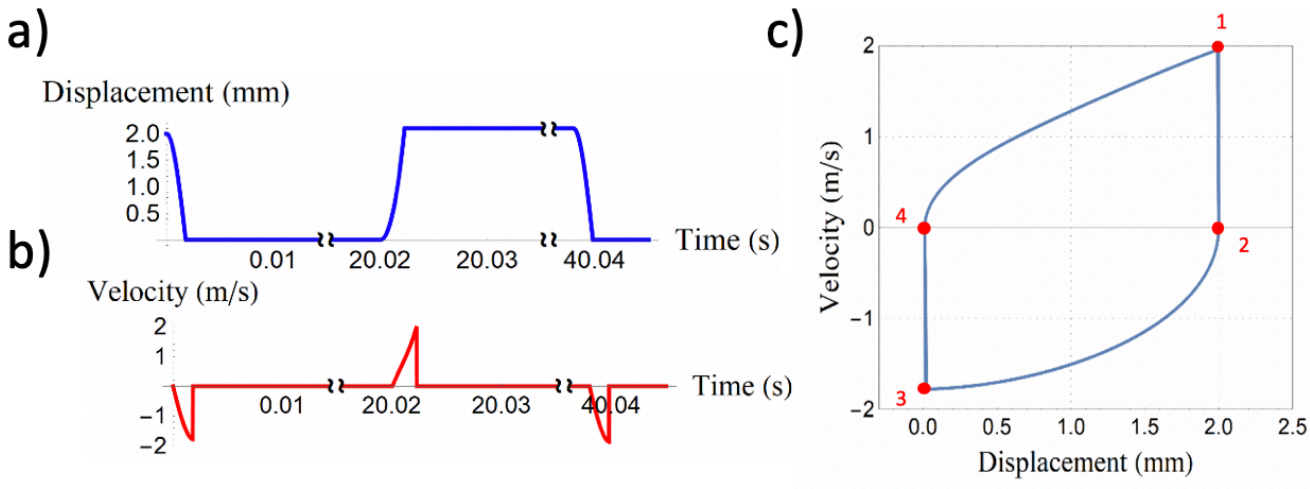

Figure 4.17- a) Displacement over time of the gadolinium tip mass. b) Velocity over time of the gadolinium tip mass. c) Velocity vs. displacement plot at the four relevant temperatures and magnetizations.

The amount of force acting on the gadolinium mass through the gap is shown in Figure 4.18. The optimal cantilever stiffness of a thermomagnetic cantilever can be calculated by drawing a diagonal line in between the force extremes of the hot and cold sides.

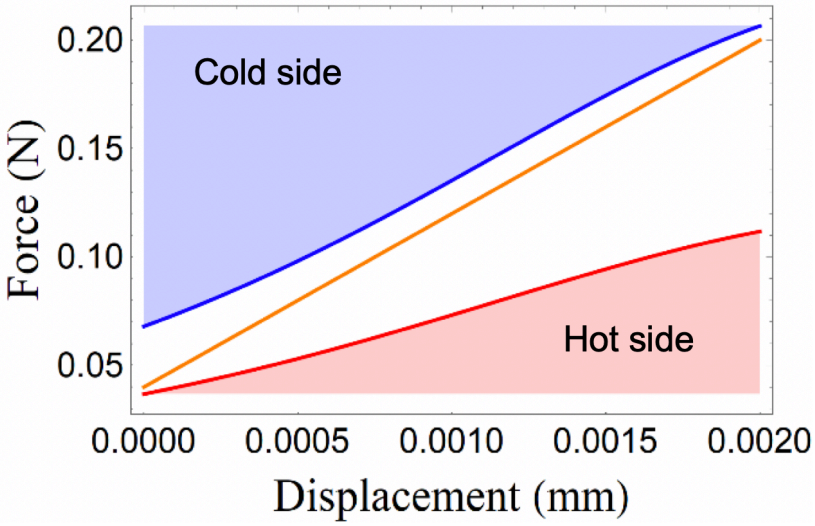

Figure 4.18- Plot of the material forces when oscillating through the magnetic gap. The optimal spring stiffness is shown by the yellow line. The maximum spring stiffness needs to be greater than the hot gadolinium at the permanent magnet but lower than the attraction forces between the cold gadolinium and permanent magnet.

Any linear spring below the red line of the graph would not let the system oscillate since gadolinium would be permanently attached to the hot magnet; vice versa, any linear curve above the cold side would not attract the gadolinium to the hot magnet. The instantaneous power developed by the movement of the gadolinium is shown in Figure 4.19 by using the magnetization force times the velocity and by deriving the kinetic energy of the system over time. Even though the theoretical maximum power of the system is 0.12 W the average power over the entire 20 second period of movement is close to 4 μW.

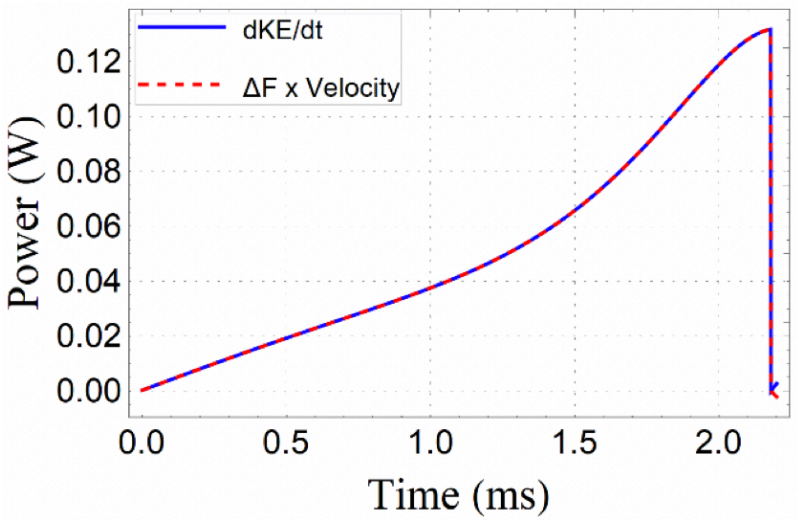

Figure 4.19- Theoretical instantaneous power generated by the TMEG.

Since Eqn. 4.30 did not consider the damping of the cantilever beam the overall power from the system is expected to be even lower. Therefore, power needed to be maximized by increasing the oscillating frequency and the amplitude displacement of the beam. With this in mind, a modification from the original concept occurred as shown in Figure 4.4. The frequency of oscillation is increased by placing a magnet on a pendulum. As a result, the frequency of the system will be synchronized to the arm movement of an individual. In this scenario, the pendulum will dominate the electrical output during motion. While in a static posture, the thermomagnetic effect as described above will generate the electrical output.

4.8 Experimental Results

The proposed wrist harvester shown in Figure 4.4B and C is constructed consisting of a TEG and TMG pendulum, and compared to a TEG module with a heatsink (Figure 4.20A).

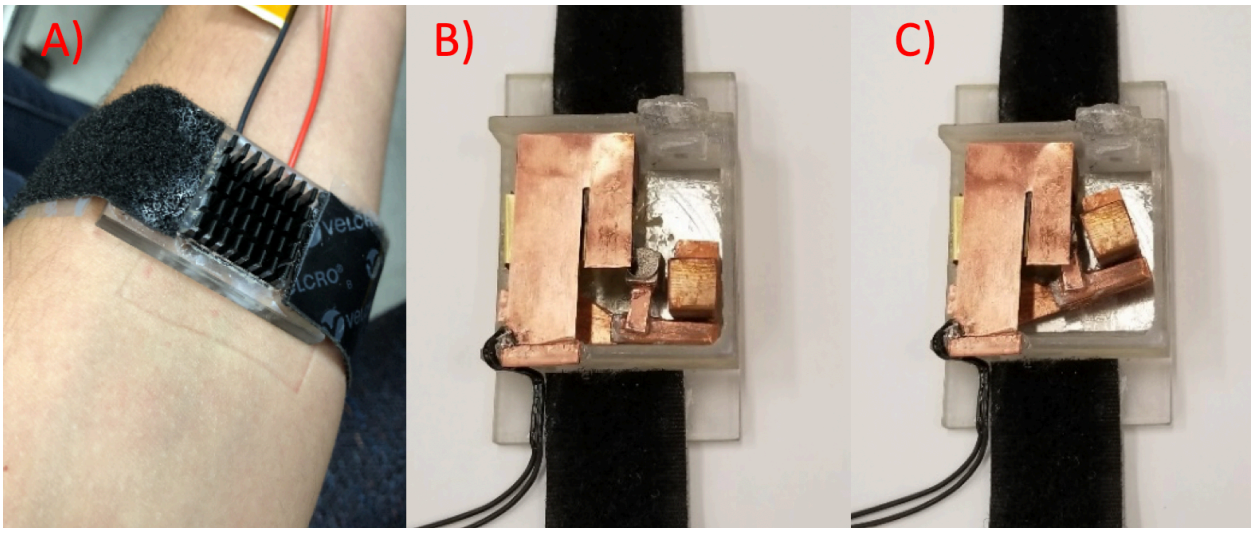

Figure 4.20- A) Thermoelectric generator with heatsink. B) Unlock position of the proposed dual harvester were the piezoelectric is free to move up and down according to thermal gradients. C) Locked position of the proposed harvester where the displacement of the piezoelectric beam is determined by the pendulum magnet.

In Figure 4.20A, the hot side of the module is attached to a copper plate which touches the wrist surface. While the cold side of the TEG is attached to a fin heatsink. On the other hand, the proposed harvester cold side consists of a heat spreader that houses the piezoelectric beam and magnetic pendulum. The heat transfer comparison of a commercial heatsink and heat spreader at an air velocity of 0.25 m/s is modeled as shown in Figure 4.21. As seen below, the temperature difference at an optimal area ratio ($A_r = 0.035$) for a TEG with spreaders can be greater than a commercial TEG ($A_r = 0.4$) with a heatsink.

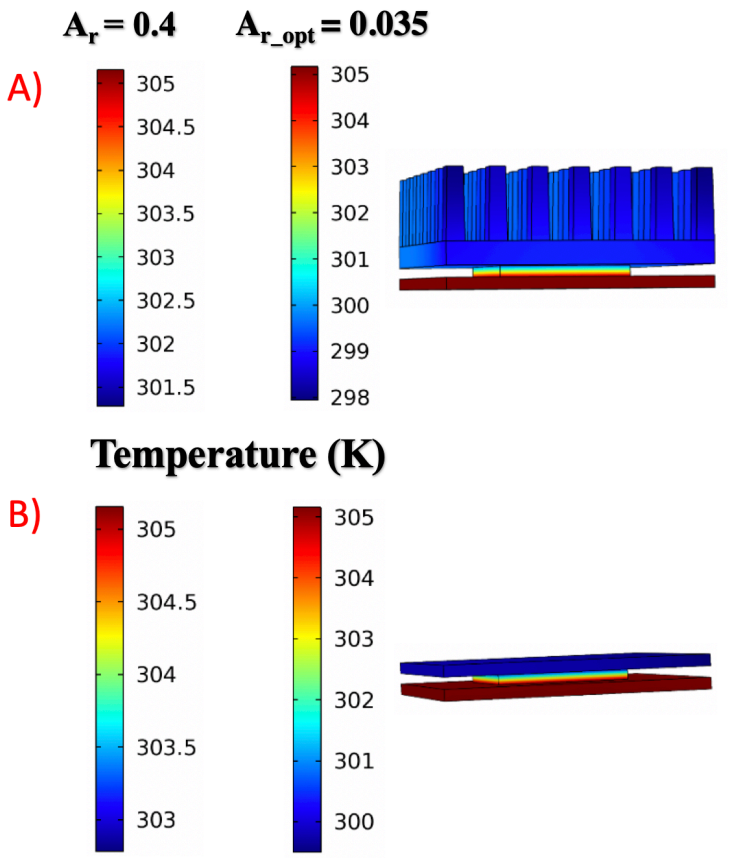

Figure 4.21- Temperature profile of TEG when walking with an air velocity of 0.25 m/s. A) TEG with heatsink at an area ratio of 0.4 ($\Delta T_{ext} = 3.5\ K$) and optimal area ratio of 0.035 ($\Delta T_{ext} = 7\ K$). B) TEG with spreaders at an area ratio of 0.4 ($\Delta T_{ext} = 2\ K$) and optimal area ratio of 0.035 ($\Delta T_{ext} = 5\ K$).

The difference between intrinsic temperatures of Figure 4.21 for a TEG with a heatsink and spreaders with the same area ratio are 1.5 K and 1 K, respectively. In the proposed concept, when the harvester is worn the temperature on the hot side spreader will increase. The heat from the body will continue to transfer through a folded brass sheet that serves as baseplate to the gadolinium resulting in a disengagement of the piezoelectric beam from the permanent magnet. The piezoelectric beam is comprised of a 200 μm thick copper substrate and a 200 μm PZT sheet with a length of 20 mm. The free end has an extra curvature to hold the gadolinium tip mass. During arm motion, the pendulum with the permanent magnet moves towards the beam. The

cantilever beam bends and the tip mass touch the magnet through the brass sheet that maintains the hot temperature of the body (Figure 4.4).

Accelerometers are mounted on the side frame of the proposed harvester to estimate the velocity of the arm motion when walking at different speeds. Two thermocouples are mounted in the hot and cold sides of the TEG module to record the temperatures over time. Output voltage from the TEG heatsink device is recorded as shown in Figure 4.22. At steady state the temperature difference across the module with the heatsink is 1.6 °C while the open circuit voltage 0.02 Volts.

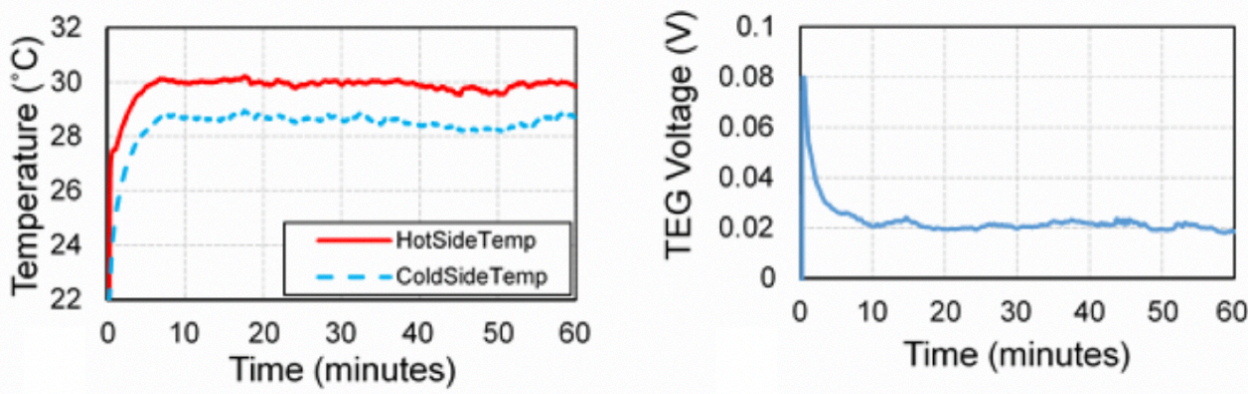

Figure 4.22- (Left) Temperature of hot and cold side over time for the TEG module with heatsink. (Right) Simultaneously open loop voltage of the module with heatsink.

When the spreader is used as a heatsink the temperature difference overtime is 0.98 °C and the voltage across a 5 ohms resistance is 9.1 mV resulting in a power of 16.5 μW. When walking at 4 mph the TMG module follows the frequency of the arm swing. In this case the voltage generated by the harvester depends on the walking speed and not in the thermal time constant as shown in Figure 4.23.

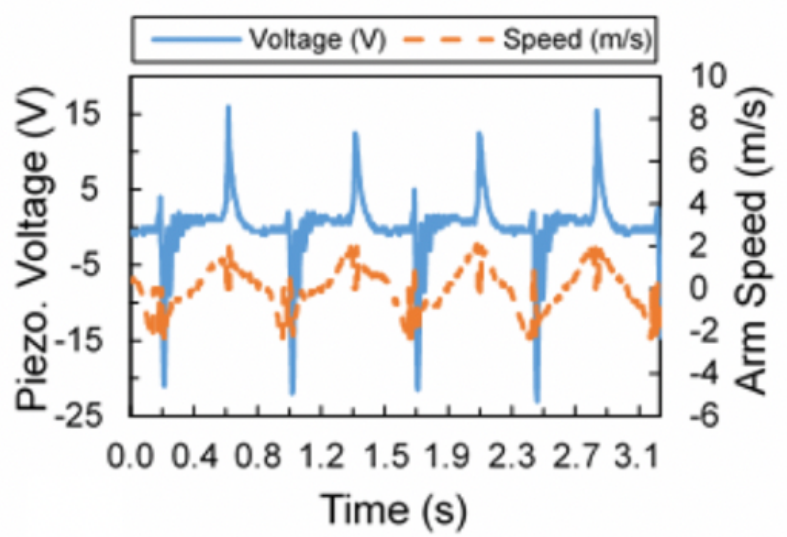

Figure 4.23- Plot of voltage and arm swing velocity as a function of time. A greater voltage peak is seen when the arm swings forward.

The RMS voltage of the piezoelectric system is calculated to be 3.69 V with an optimal load resistance of 600 kOhms resulting in a power of 23 μW when swinging an arm at a frequency of 2.6 Hz. When walking at a 1 Hz frequency, the power developed by the TMG harvester decreased to 11.8 μW. Therefore, the inclusion of the TMG in the system increase the power generated by ~70%, however, using the same conditions a TEG with a heatsink generated 24.3 μW. Overall, the proposed dual harvester is better in motion when compared with a TEG and heatsink assembly while worst in static posture by the small change in temperature and frequency across the thermomagnetic cantilever.

4.9 Thermomagnetic Energy Harvesting from Surroundings

In Section 4.8, the TMG contributed little during static posture, however, during motion the magnetic pendulum dominated power generation. Recent work publish by Chun et al. ([72], [73]) have shown that thermomagnetic cantilever beams can achieve high frequencies and improve power generation. In this section, a TMG generator was optimized for standalone

applications at high temperature differentials. A low frequency and high displacement TMG harvester is hypothesized to produce a greater average power when compared to current high frequency and low amplitude TMG harvesters ([72], [73]).

Piezoelectric energy harvesting converts change in strain ($\Delta\epsilon$) in a mechanical system into an output electrical voltage. Different ways to generate higher output power is by having a higher amplitude oscillation on a system (high $\Delta\epsilon$) or a higher frequency oscillation with a small amplitude (constant $\Delta\epsilon$). If one considers a vibrational cantilever beam to be a string on a shaker. The kinetic energy at each element of the system will be governed by the equation [31]

$$\delta KE = \frac{1}{2}(\delta m)(v^2) \tag{4.33}$$

where δKE is the kinetic energy at each element and δm the mass of each element. If one assumes the piezoelectric moves in a sinusoidal manner $x = A\sin(kx - w\,t)$. One can derive the equation of displacement with respect to time to find the velocity of the system

$$\delta KE = \frac{1}{2}(\delta m)(-A\,w\cos(kx - w\,t))^2 \tag{4.34}$$

where k is the wave number equal to $\frac{2\pi}{\lambda}$ and λ is wavelength. On the other hand, the potential energy of the system will be comprised of the spring constant of the mechanical piezoelectric beam k_{beam} and displacement x [31]

$$\delta PE = \frac{1}{2}k_{beam}x^2 \tag{4.35}$$

where k_{beam} is equal to $w^2 * \delta m$ and $x = A\sin(kx - wt)$. As a result, the change in potential energy is

$$\delta PE = \frac{1}{2}w^2\,(\delta m)(A\sin(kx - w\,t))^2 \tag{4.36}$$

From the change in potential and kinetic energy equations in the system one can see that the mechanical energy is proportional to the square of the frequency w^2 and the square of the amplitude A^2.

In a piezoelectric TMG, in order to increase the frequency of the system at a constant amplitude one needs to increase the thermal conductivity of the soft magnetic material. Using a spin coating machine, a 20 μm silver coating is deposited on gadolinium to improve the thermal conductivity at the interface between the gadolinium and hot/cold sources, as shown in Figure 4.24.

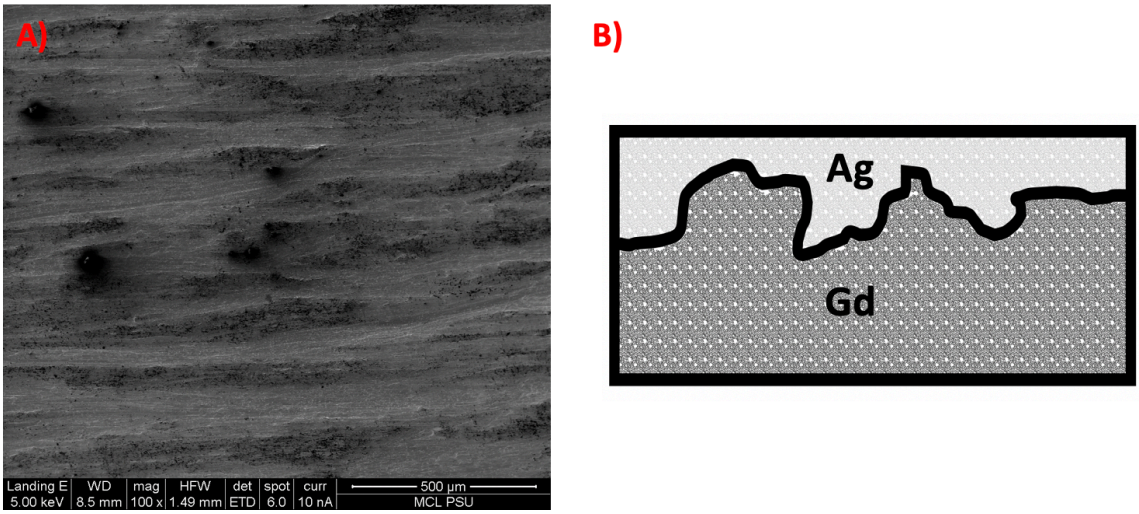

Figure 4.24- A) Roughness of commercial gadolinium without any modifications. B) Cross sectional schematic of silver (Ag) deposition on gadolinium (Gd).

The thermal resistance between the hot magnet and an uncoated gadolinium tip mass can be expressed as [86]:

$$R_{totGd} = \frac{1}{h_{NdGd}A} + \frac{L_{Gd}}{k_{Gd}A} \tag{4.37}$$

where h_{NdGd} is the thermal contact coefficient between the neodymium permanent magnet and gadolinium, k_{Gd} thermal conductivity of gadolinium ~10.5 $\frac{W}{m\,K}$ and L_{Gd} is the thickness of the gadolinium tip mass ~127 μm. However, when silver is deposited to the tip mass Eqn. 4.37 modifies to:

$$R_{tot} = \frac{1}{h_{NdAg}A} + \frac{L_{Gd}}{k_{Gd}A} + 2\frac{L_{Ag}}{k_{Ag}A} \tag{4.38}$$

where k_{Ag} is the thermal conductivity of silver and L_{Ag} the thickness of the silver coating. Hence, in Eqn. 4.38 the thermal contact coefficient of the silver touching the neodymium magnet (h_{NdAg}) differs to the thermal constant of the gadolinium when touching the permanent magnet (h_{NdGd}). The thermal coefficient of the interface of two materials is expressed by Cooper et al. [88] as:

$$h = \frac{1.25k_s\left(\frac{P}{H}\right)^{0.95}}{\frac{\sigma}{m}} \tag{4.39}$$

where P is the contact pressure, H the hardness of the softest contact material, σ is the RMS surface roughness,m the RMS surface slope and k_s the total conductivity of the two surfaces expressed by [86]:

$$k_s = \frac{2k_1k_2}{k_1 + k_2} \tag{4.40}$$

where each subscript represents the materials under contact. The constants used to simulate the total thermal resistance of the two compositions are shown in Table 4.4. Different silver coating thickness were applied in the model to find the optimal thickness of silver. The surface roughness and slope of the two surfaces in contact are also changed. Additional information on how to find these values is shown in past literature ([88], [89]).

Table 4.4- Selected parameters to calculate the total thermal resistance between the uncoated/coated tip mass and hot magnetic surface.

Parameter	Units	Value
Surface Area	mm^2	42.25
Thickness of Gd	μm	127
Gd Thermal Conductance	$\frac{W}{m\,K}$	10.5
Ag Thermal Conductance	$\frac{W}{m\,K}$	406
Nd Thermal Conductance	$\frac{W}{m\,K}$	8.95
Gd Hardness	MPa	570
Ag Hardness	MPa	251
Nd Hardness	MPa	343
Force of Magnet	N	24.5

If thermal contact resistance is neglected the total resistance of an uncoated gadolinium tip mass and neodymium magnet will be govern by the second term of Eqn. 4.37 and result in $0.286\,\frac{K}{W}$. On the other hand, the total thermal resistance of a silver coated gadolinium tip mass is governed by the second and third terms in Eqn. 4.38. Resulting in $116.46L_{Ag} + 0.286\,\frac{K}{W}$ where the thickness of silver, L_{Ag}, is expressed in meters. In other words, as the thickness of the silver increases the total thermal resistance will increase and when the thickness is zero the thermal resistance will be $0.286\,\frac{K}{W}$. However, when including the contact resistance between the Gd and neodymium permanent magnet the total thermal resistance of the system varies as shown in Figure 4.25.

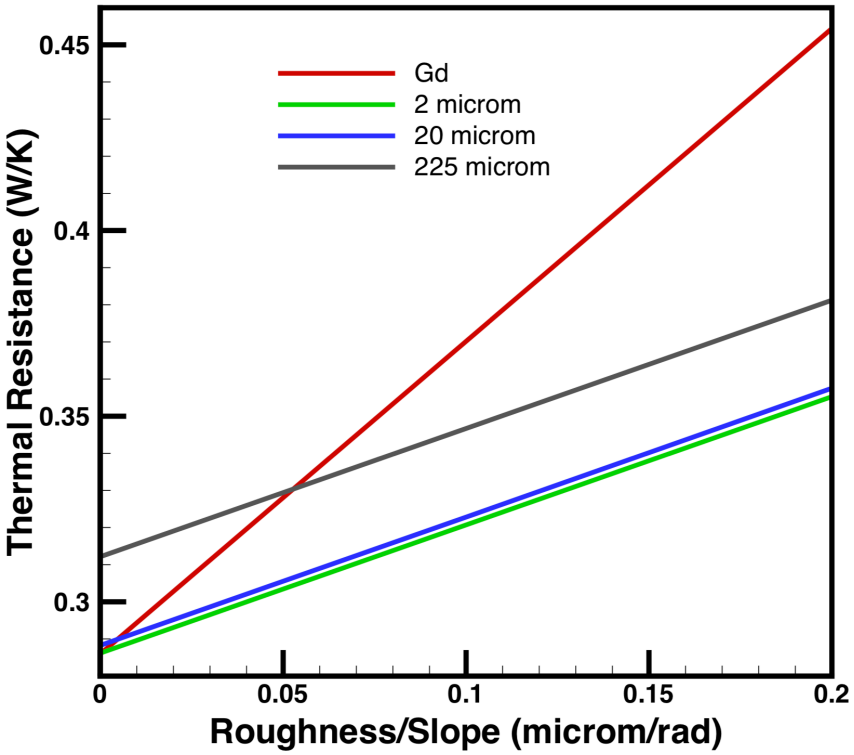

Figure 4.25- Thermal resistance of gadolinium (Gd) and silver coated Gd at different surface roughness/slope where each plot represents the silver coating thickness on gadolinium.

An ideal gadolinium tip mass, roughness/slope of material is equal to zero, will have a lower thermal conductivity when compared with a coated tip mass. However, at low roughness values a thin layer of silver will slightly decrease the total thermal resistance of the tip mass. Moreover, when a thick coating layer is applied; for example, 225 μm the thermal resistance of the coated material will increased when compared to an uncoated material.

It is important to remember that a cantilever TMG is not a common vibrational system since the energy when the Gd moves to the hot magnet $(F_{mag} - F_{spring}) * v_h$ is different than the energy when the Gd moves to the cold surface $F_{spring} * v_c$, as shown from the TMG piezoelectric output voltage in Figure 4.26.

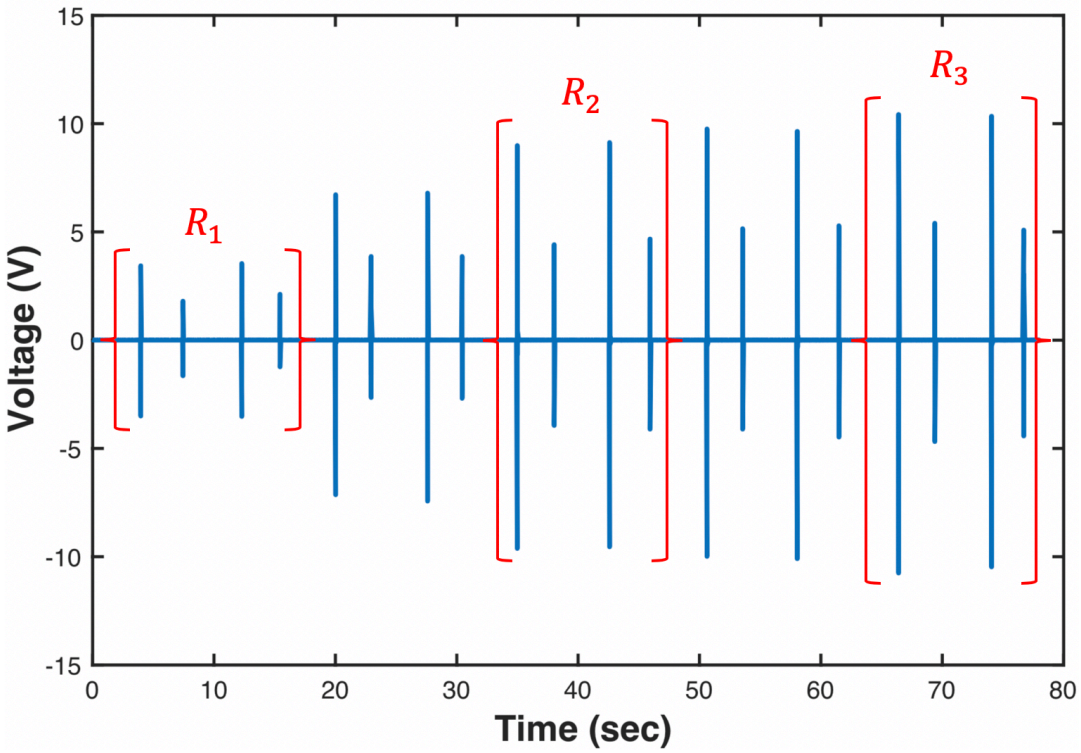

Figure 4.26- Voltage from piezoelectric TMG at different resistances where $R_3 > R_2 > R_1$. The first peak at each resistance represents the voltage developed when the tip mass was moving to the hot surface while the second represents the movement of the mass when the tip mass moved to the cold source.

Since the voltage amplitude of the system varies, the RMS and peak voltages are analyzed to find the optimal resistance at a particular gap distance. An energy harvesting cantilever was built with a tip to base ratio of 0.375 for maximum power generation as shown by Chun et al.[73]. The setup to find the maximum and average power at a given amplitude between hot and cold sources is shown in Figure 4.27. In this figure, one can see that the optimal resistance to generate maximum power differs to the optimal resistance to generate maximum average power.

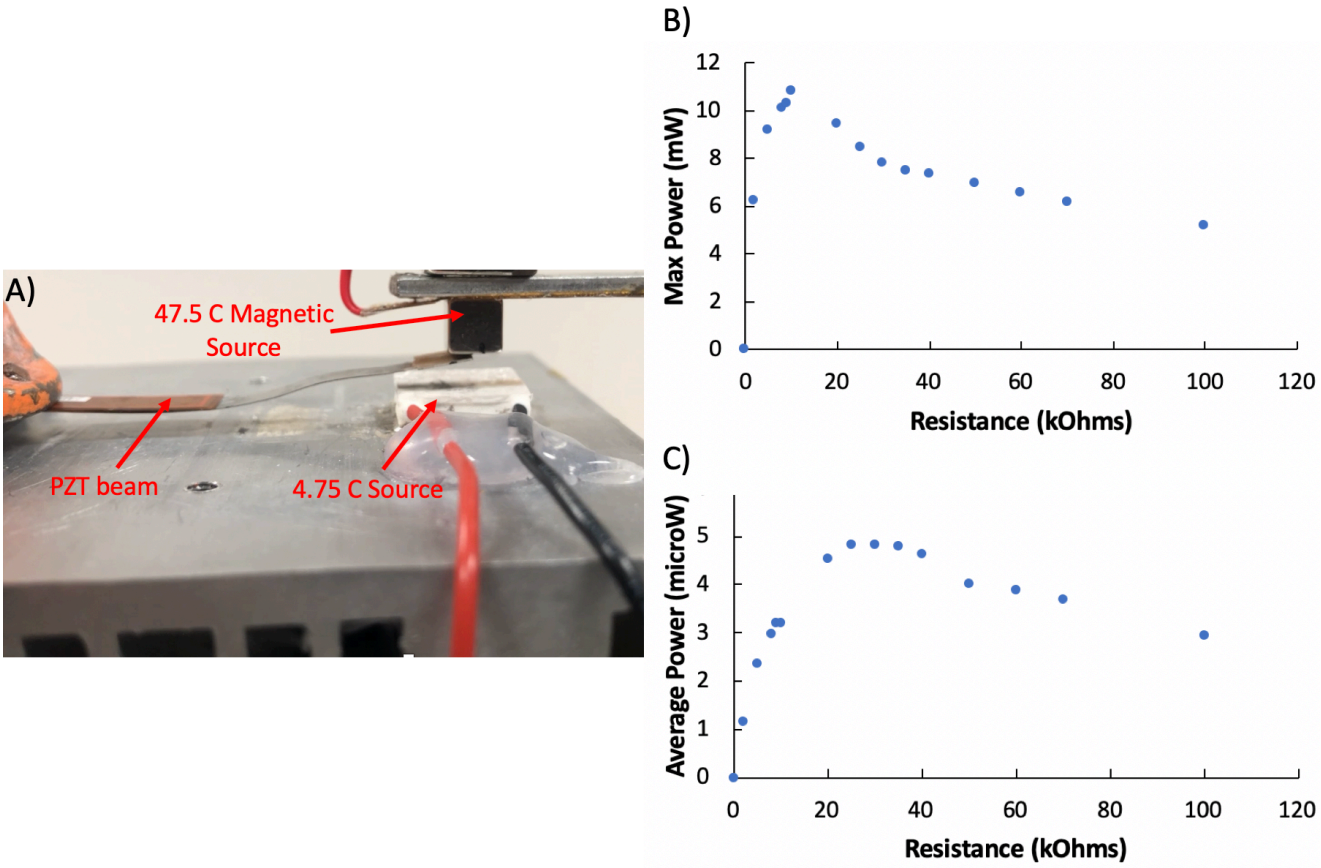

Figure 4.27- A) Experimental setup of the cantilever TMG for a temperature differential of 42.75 °C. B) Maximum peak electrical power at different load resistance. C) Average electrical power at different load resistance.

Once the optimal resistance at a determined gap is found. The hot magnetic source was moved in the bending direction to find the optimal gap distance as shown in Figure 4.28.

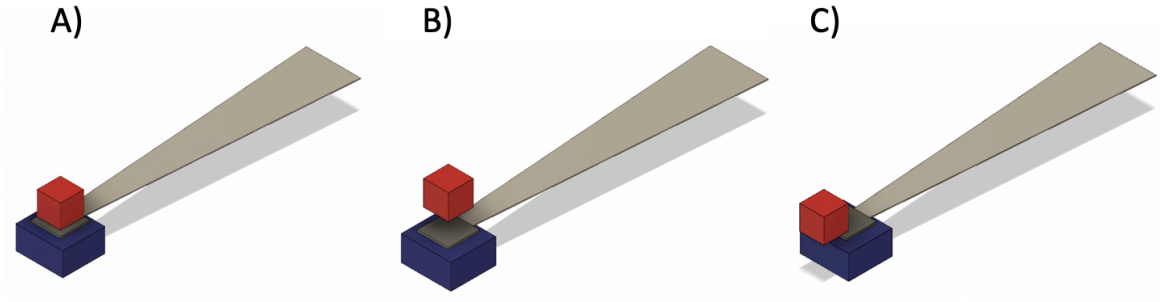

Figure 4.28- A) Origin where the hot magnet is resting on top of the gadolinium tip mass were coordinates are (0,0,0). B) Maximum amplitude at the origin point at (0,0,z_{max}). C) Maximum movement in the y-direction to increase the bending moment at coordinates (0, y_{max},0).

For a given amplitude in the z-coordinate multiple variations are tested in the y-coordinate. Maximum power and average power at the different coordinate combinations are shown in Figure 4.29. Magnetic movements in the x-coordinate were not considered since this would create a torque on the cantilever and reduce the total electrical power.

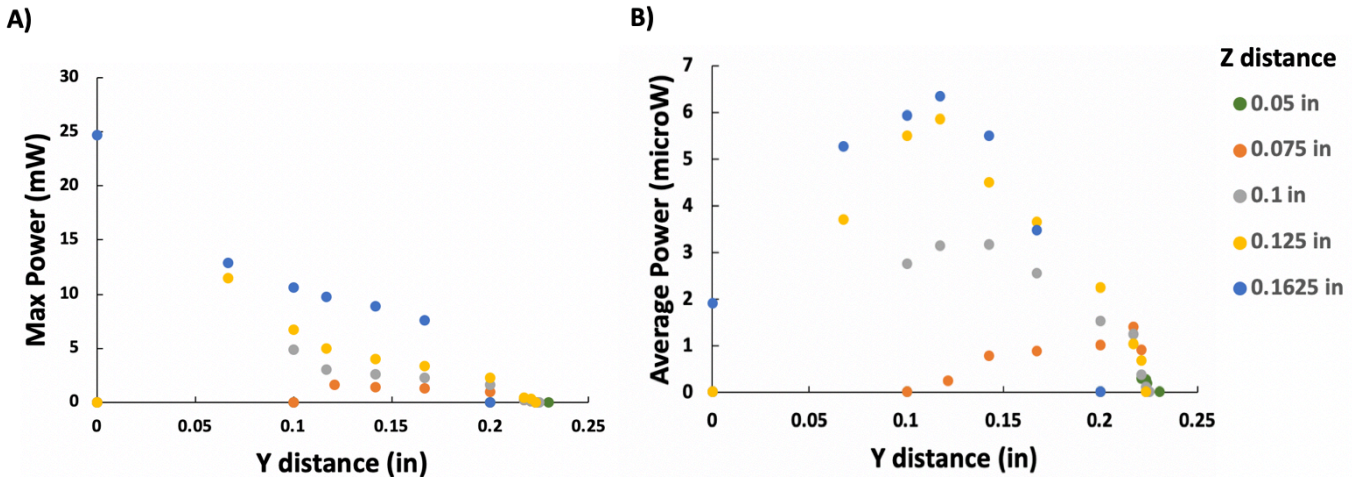

Figure 4.29- A) Maximum power at different z and y coordinates combinations. Maximum power occurs at higher gap amplitudes and decreases as y is increased. B) Average power at different y and z coordinates combinations. Higher average power occurred at higher z distances; however, an optimal y-distance is needed to achieve higher power.

At lower z-distances the frequency of the harvester increased; however, the amplitude of oscillation decreased. Figure 4.29B shows that amplitude is more important than frequency when

generating power in a cantilever thermomagnetic generator. To confirm that amplitude oscillation is more important than frequency oscillation, a 47 μF capacitor is charged with the same parameters. Frequency of the device is measured by the frequency of the voltage signal in the capacitor, as shown in Figure 4.30.

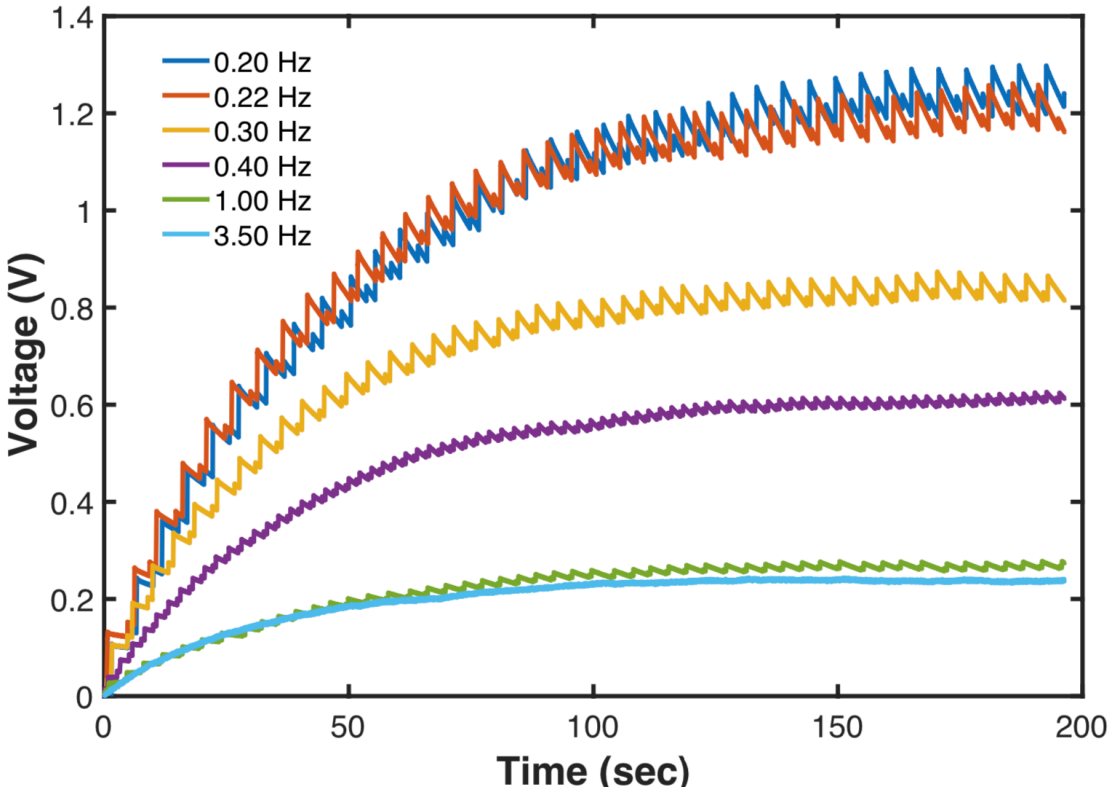

Figure 4.30- Voltage across a 47 μF capacitor when using the same harvester at different oscillation frequencies; in other words, distance between hot and cold reservoir.

Having defined the optimal z and y distances between the hot and cold reservoirs. The heat transfer model is validated experimentally by using the same setup shown in Figure 4.27A. The time of oscillation between two different gadolinium coatings and uncoated tip mass is shown in Figure 4.31. The period of oscillation of the uncoated material was around 2.98 seconds, while silver and carbon nanotube coating increased the period of oscillation to 5.926 seconds. Finally, the silver coated material decreased the total cycle time to 1.52 seconds, in other words, about 100% increase in frequency when compared to the uncoated material.

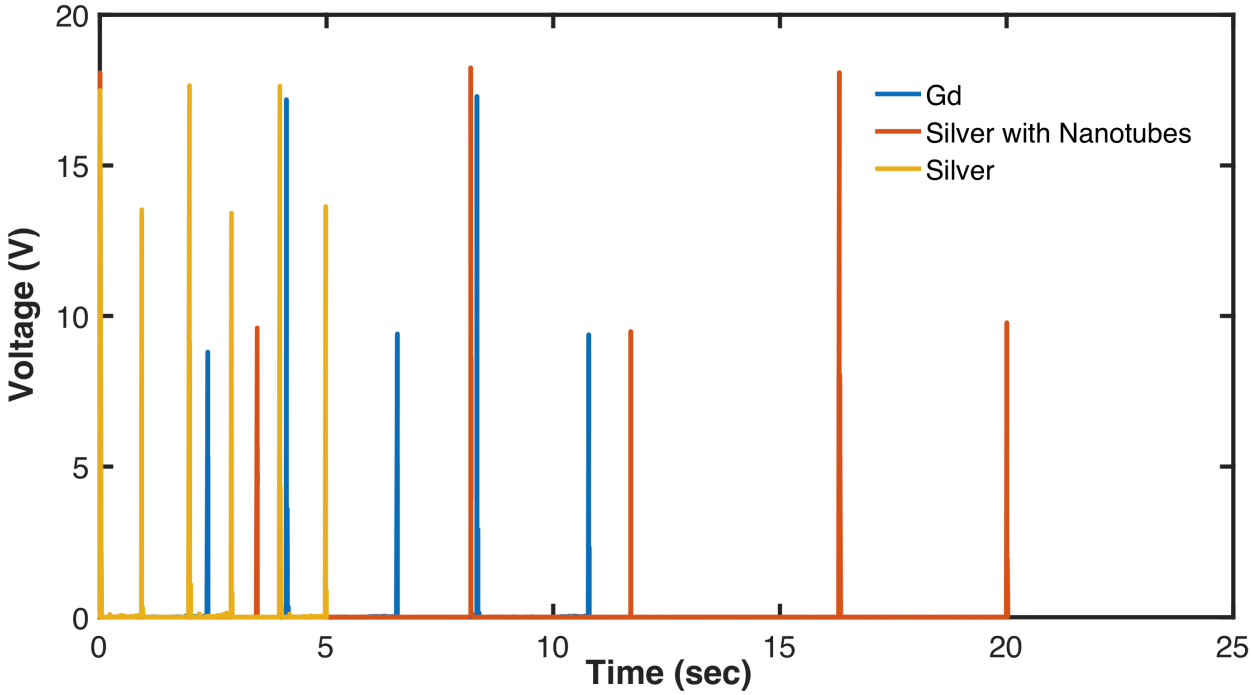

Figure 4.31- Total cycle time of the cantilever TMG with 3 different tip mass coatings.

In Figure 4.31, each voltage spike of the TMG was able to power about 100 LEDs. However, the intensity of the LEDs decreased in the lower voltage spike when the TMG moved from hot to cold side. To make the power developed from each spike useable, a supercapacitor is charged for 427 minutes. The voltage developed in the supercapacitor is able to power an NI tag CC2650STK sensor which recorded the temperature and humidity in the room and communicated with a mobile phone in real time. Multiple harvesters can be used along a hot magnetic surface to decrease the amount of time to power this sensor. As a result, it would take about 7 thermomagnetic cantilevers to power the NI tag CC2650STK sensor in 1 hour.

Chapter 5 Energy Scavenging from Electromagnetic Fields to Power Sensors

5.1 Introduction

In this chapter, the design of a stand-alone energy harvester that absorb energy from magnetic fields is built to power sensors. The device is excited by the interaction of the magnetic field from an electrical source and a stationary magnetic field. The field torque induces a vibration in the structure, therefore, a piezoelectric composite can harvest power from the change of strain during deflection. Since powerlines waveforms are normally comprised of 50 Hz, 230 V or 60 Hz, 110 V the desired harvester natural frequency needs to be tuned to the powerline frequency. A simple diagram of a magnetic field cantilever harvester is shown in Figure 5.1.

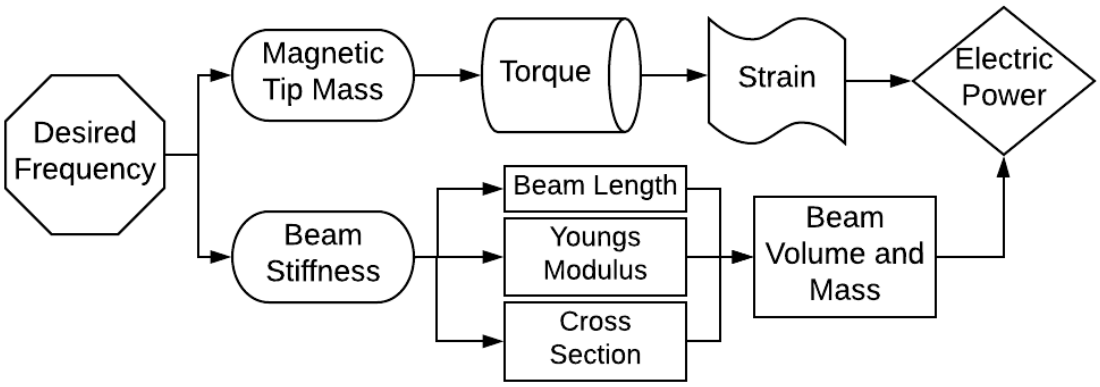

Figure 5.1- Schematic of a tuned cantilever magnetic field harvester.

Figure 5.1 details two key parameters for a cantilever magnetic field harvester: magnet tip mass and stiffness of the beam. These two parameters comprised the natural frequency shown as [31]:

$$w_n = \sqrt{\frac{k}{m}} = \sqrt{\frac{3EI}{ml^3}} \tag{5.1}$$

where E is the material Young's Modulus, I is moment of inertia of the beam, m is mass of the tip and l is length of the beam. To increase the energy harvested, PZT materials have to be attached to the structural parts where maximum strain occurs while maintaining the desired resonance frequency of 60 Hz.

In this chapter, literature from magnetic field and vibrational piezoelectric energy harvesters is reviewed. Then, experiments and models of a two degree of freedom magnetic harvester are developed. Finally, the proposed harvester is shown to power a commercial sensor without the need of an external capacitor.

5.2 Review of Magnetic field Energy Scavengers

Magnetic field energy harvesters are governed by Faraday's law of induction which is represented as [90]:

$$V_{emf} = -N\frac{\Delta\phi}{\Delta t} \tag{5.2}$$

where V_{emf} is the induced voltage, N the number of turns of a coil, t time and ϕ the magnetic flux comprised of the magnetic field times the effective cross-sectional area. Using this principle, Yuan et al. [91] developed a system that could harvest energy under the powerlines magnetic field and produce 1.86 $\frac{\mu W}{cm^3}$ at 7 μT. Similarly, harvesters placed on powerlines ([92],[93]) are intrusive to the cable vibrations and produce a higher output power. Magnetic induction harvesters which are placed on cables normally harvest more energy since the flux density at the cable source is higher. The disadvantage of these systems is their bulkiness; therefore, a lower power density is expected.

Recently, a new way to harvester energy from magnetic fields has been introduced by using magneto-mechanic-electric (MME) harvesters [94]. They are designed to use a magnetoelectric (ME) beam comprising of a piezoelectric and a magnetostrictive material which

provides magnetic and elastic behaviors [95]. Annapureddy et al.[94], created a cantilever MME harvester with a magnet as a proof mass in order to amplify the ability to transduce energy between the magnetic and piezoelectric domains. This system generated an output power of 0.73 mW at 0.7 mT.

In an MME cantilever system, the proof magnetic mass can always be changed in order to interact with surrounding magnetic fields. The magnetic mass also provides a mechanical torque under a magnetic field [96] described as:

$$\tau = (M\ x\ B) * V \tag{5.3}$$

where M is magnetization, B is external magnetic field and V is volume. Similarly, Kang et al. [97] enhanced an MME cantilever beam by understanding the nature of the magnetic field induced vibrations, and concluded that vibrations from the magnet tip mass are the main contributor to the power developed. However, a high ME coupling enhances the total power. As a result, a system which generates 180μW and 9.8 mW peak power under AC magnetic fields of 0.1 and 1 mT was reported.

5.3 Review of Vibrational Energy Scavengers

A dual broadband harvester which generates electrical power from vibrations and AC magnetic fields was developed by Song et al. [98]. The harvester consists of five piezoelectric cantilevers with different lengths and magnetic tip mass. The system is excited at 1g of acceleration while also under an AC magnetic field. The power density exhibit by this device was of 243 $\frac{\mu W}{cm^2 g^2}$ with a bandwidth of more than 30 Hz. A different way to enhance vibrational harvesters is demonstrated by Lin et al. [99]. In their work, fixed permanent magnets caused nonlinear forces to a cantilever beam with a magnetic tip mass. Their results show that under resonance the voltage produced by the piezoelectric beam was similar to the one with no

magnetic coupling. On the contrary, when outside resonance the voltage output from the coupled system increased when compared to a magnetic coupled system.

Pure vibration energy harvesters comprising of a cantilever beam and tip mass are commonly known in literature ([100],[101]). If a vibration source frequency is known, a cantilever beam could be fabricated to match its resonance frequency. However, surrounding devices have different vibrational frequencies, therefore, making magnetic field harvesters more feasible when harvesting from surroundings.

5.4 Mechanisms Descriptions

5.4.1 Manufacturing of Magnetic Field Scavengers

Manufacturing of MME harvesters can vary according to its shape and complexity. A common magnetic cantilever beam is comprised of a PZT ceramic over a laminated magnetostrictive material, and a magnetic tip mass as shown in Figure 5.2.

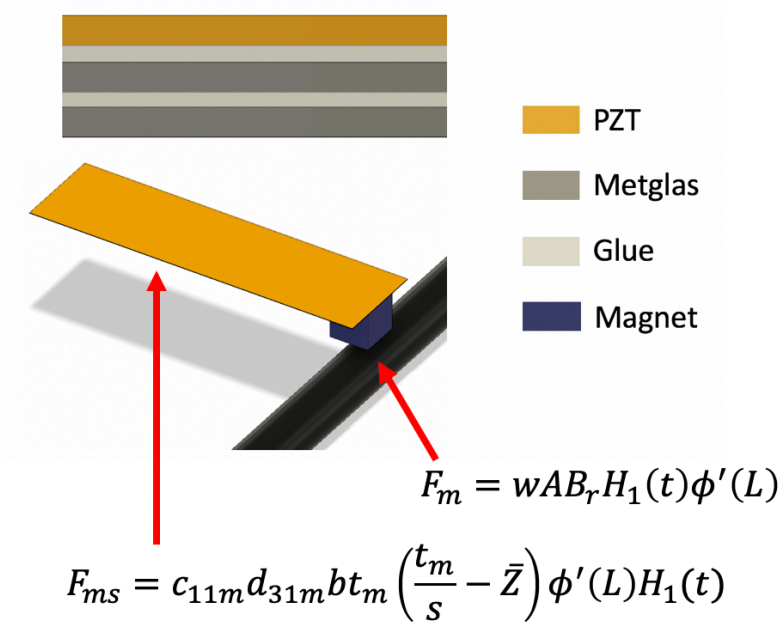

Figure 5.2- Total thickness of beam is 0.1 mm (Metglas 23 microns, glue 12 microns and PZT 30 microns). Forces on a common magnetic beam harvester described by Annapureddy et al.[94].

For complex structures, for example curved beams, a mold needs to be manufactured in order to laminate the Metglas® and solidify the structure. Then, a PZT material can be attached to the beam curvature (Figure 5.3A). Other MME architectures include the manufacturing of a nonmagnetic structure which is laminated in areas for high concentrated magnetic field (Figure 5.3B) or manufacturing Metglas® absorbers to harvest energy from a greater distance, as shown in Figure 5.3C.

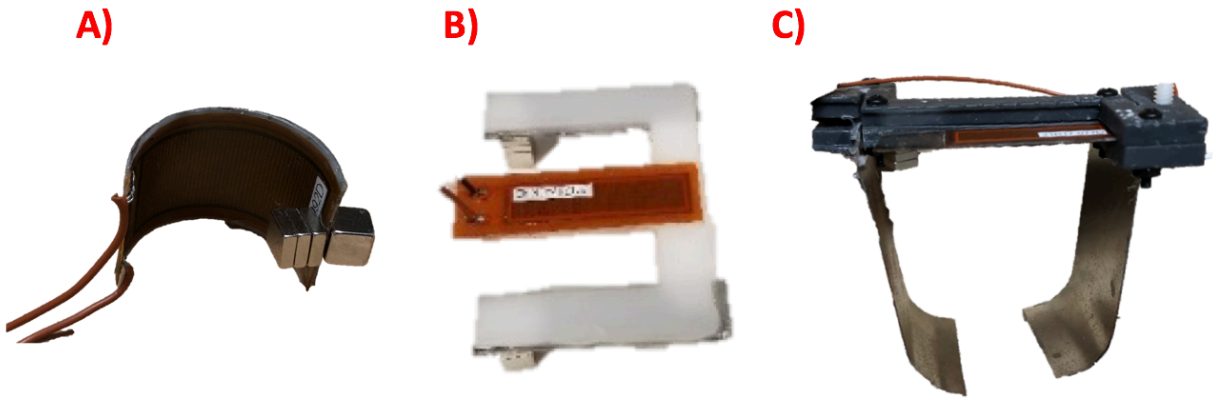

Figure 5.3- A) Curved magnetic harvester where a mold is needed to create the curvature. B) Complex plastic structure where magnetostrictive material is added to the locations for flux concentration. C) Magnetic field harvester where extended magnetostrictive absorbers are manufactured in order to absorb magnetic flux from a larger distance.

5.4.2 Design of Magnetic Field Scavenger

This section describes the design of a magnetic field harvester used for standalone and wearable applications. When designing the harvester, it is crucial to consider the mass and volume of the device so it is not intrusive to the wearer or environment. The harvester should be able to absorb magnetic fields dynamically by standing close to the wire. Therefore, providing a contactless power transmission. It was hypothesized that a double beam configuration or a two degree of freedom system (Figure 5.4) could produce a higher power density if the secondary mass reached isolation while the primary beam had higher oscillation amplitudes.

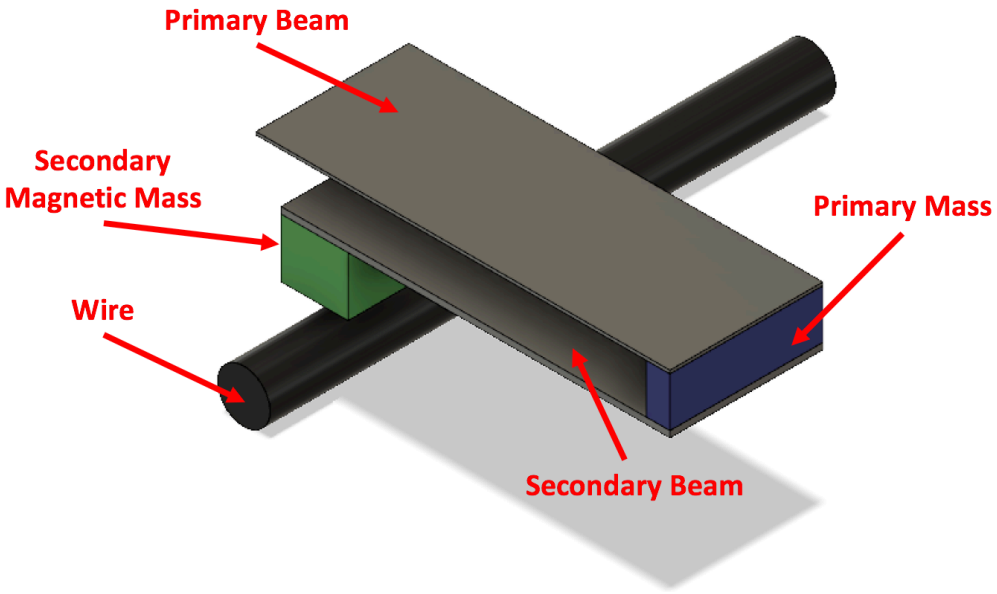

Figure 5.4- An isometric view of the proposed two degree of freedom energy harvester. The harvester consists of magnetostrictive primary and secondary beams joined by a non-magnetic primary mass. A secondary magnetic mass is attached to the end of the secondary beam.

The harvester consists of two beams made of magnetostrictive and piezoelectric laminates as shown in Figure 5.4. The secondary magnetic mass and current wire provide the excitation to the structure. While piezoelectric attached to the primary and secondary beam generates the power harvested. The architecture conditions to achieve a lower displacement in the secondary mass are presented in Section 5.5.

5.5 Modeling

Each beam of the proposed harvester consists of magnetostrictive and piezoelectric layers using Metglas® and PZT macro fiber composite (MFC) layers. The secondary magnetic mass experiences a torque which applies a moment to the secondary beam end. The proposed energy harvester can operate in two modes. The first mode consists of both masses going in phase of each other as shown Figure 5.5A while the second mode consist of both masses going out of

phase with each other, as shown in Figure 5.5B. In the second mode, the secondary mass reaches isolation while the primary mass high oscillation displacements.

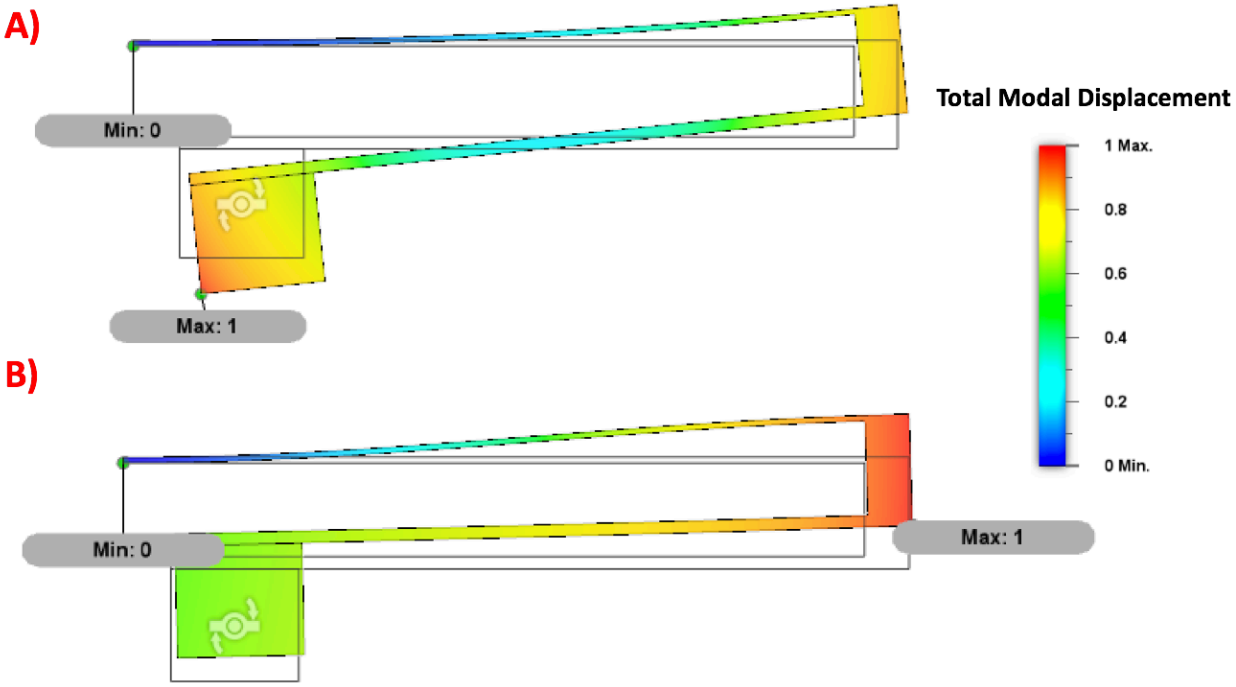

Figure 5.5- First two modes of the designed beam architecture. A) First mode where the maximum displacement occurs at the secondary mass. B) Second mode where maximum displacement occurs at the primary mass.

The terminals of the two MFC were combined such that both layers contributed to the power constructively. The beams are manufactured to have low stiffness to operate in the second mode of the harvester.

Piezoelectric beams are combined in parallel to get a total capacitance C_p and voltage V is read across a resistance R_l. The displacement of the primary mass (m_1) is $x_1$and secondary mass (m_2) is x_2. Damping coefficients of each beam is c_1 and c_2, and piezo electric coupling coefficient is G_1 and G_2. The free body diagram of the structure is shown in Figure 5.6

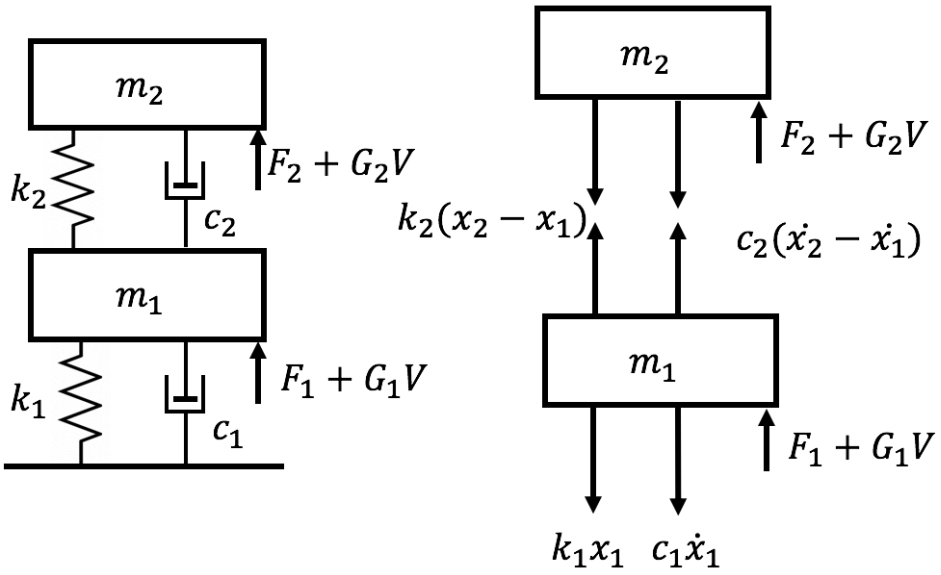

Figure 5.6- Schematic of the two degree of freedom magnetic harvester.

As a result, the equations of motion of the two degree of freedom harvester are

$$m_1\ddot{x_1} + (c_1 + c_2)\dot{x_1} + (k_1 + k_2)x_1 - c_2\dot{x_2} - k_2x_2 - G_1V = F_1 \tag{5.4}$$

$$m_2\ddot{x_2} + c_2\dot{x_2} + k_2x_2 - c_2\dot{x_1} - k_2x_1 - G_2V = F_2 \tag{5.5}$$

$$C_p\dot{V} + G_1\dot{x_1} + G_2\dot{x_2} + \frac{V}{R_l} = 0 \tag{5.6}$$

where F_2 consists of the end magnet and the equivalent force due to the magnetostriction of the Metglas® layers [94]. While F_1 consist of the force due to the magnetostriction of the Metglas® in the primary beam. The second mode shape is used to estimate the coupling coefficient G_1, G_2 and stiffness of the beams. The power is estimated from the voltage using [3]:

$$P = \frac{V_{max}^2}{2R_l} \tag{5.7}$$

where

$$V_{rms} = \frac{V_{max}}{\sqrt{2}} \tag{5.8}$$

the damping of the system was found experimental as shown in Section 5.7. An eigen analysis of the structured was created to find the masses and stiffness combination which would create the second mode shape. The two frequencies of the system were obtained as function of the base frequency [31]

$$w_1 = \sqrt{\frac{k_1}{m_1}} \tag{5.9}$$

mass ratio

$$\mu = \frac{m_2}{m_1} \tag{5.10}$$

and frequency ratio

$$\beta = \frac{w_2}{w_1} \tag{5.11}$$

As a result, the frequencies obtained were

$$w_{a,b} = w_1 \sqrt{\frac{1}{2\beta^2}(\alpha \pm \sqrt{\alpha^2 - 4\beta^2(1-\mu)})} \tag{5.12}$$

where

$$\alpha = 1 + \beta^2(1+\mu) \tag{5.13}$$

A plot of the two natural frequencies normalized with base frequency w_1 is shown in Figure 5.7A. From this figure one can see that by increasing the mass ratio the second modal frequency w_b increases several times its base frequency.

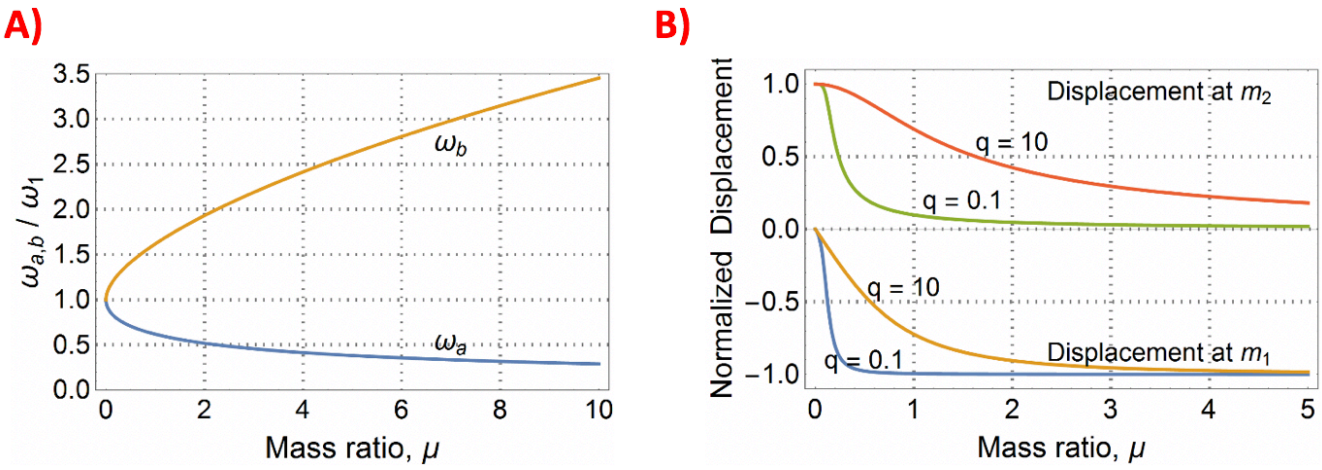

Figure 5.7- A) The distribution of the first two modes of the system as a function of mass ratio for β =1. It can be observed that the second mode can be at least 5 times higher when μ > 4. B) The eigenvector for two stiffness ratios (q = 0.1, and 10) is plotted as a function of mass ratio. At low mass ratios, the system behaves as a vibration isolator, while at higher mass ratios the displacement at the primary mass $m_1$is higher than that of the secondary mass at m_2.

A plot of the eigenvector in the second mode is shown in Figure 5.7B, for two values of the stiffness ratio

$$q = \frac{k_2}{k_1} \tag{5.14}$$

At a mass ratio less than 0.25 and q = 0.1, the amplitude of the secondary mass is larger than the primary mass as shown in Figure 5.7B. For the primary mass to resonate and secondary mass have smaller amplitudes, the mass ratio needs to be higher than 0.25. Isolation of the secondary mass is beneficial since the structure will receive a uniform magnetic field. As the primary beam has higher share of the piezoelectric material, the increased displacements compared to the secondary beam would result in greater power levels. By selecting appropriate values of mass and stiffness ratios, the harvester is designed to operate in the second more.

5.6 Experimental Setup

Magnetic fields at 10 mm distance around a 400 kV 3-phase overhead power lines are close to 20 Gauss [100]. To achieve a high magnetic field similar to the ones experience in the

power lines a current carrying conductor is simulated by making 50 turns of 24 AWG copper wire and encasing it in a 1 cm diameter hollow brass tube. An alternative current is passed through the wire to simulate the oscillating magnetic field. The three currents levels used are 0.36 A, 0.58 A and 0.75 A which created magnetic flux densities in the wire of 3.5 and 7 Gauss at 2 mm away from the wire. The setup of the experiments is shown in Figure 5.8A while the magnetic flux density with respect to the distance from the wire is shown in Figure 5.8B.

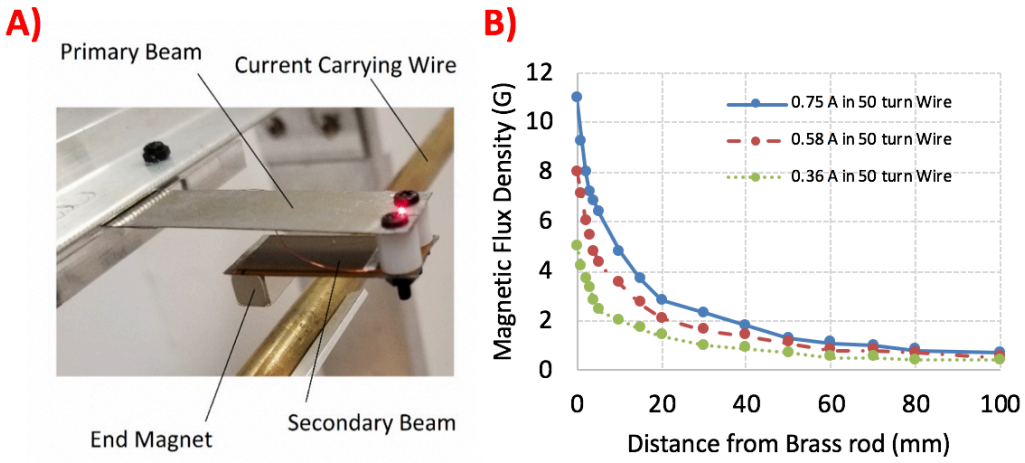

Figure 5.8- A) Experimental setup of the folded magnetic harvester. B) Magnetic flux density at different distances from the current carrying wire comprised of 50 turns.

5.7 Experimental Results

A 49 mm long and 15 wide Metglas beam comprised of 5 layers is constructed. The frequencies observed experimentally are shown in Figure 5.9A. A transcendental equation [101], is used to find the equivalent Young's modulus of the composite to be around 9.67 GPa. The response of the beam is shown in Figure 5.9B is studied to find the damping ratio by using the logarithmic decrement formulas [31]:

$$\delta = \frac{1}{n}\ln\left|\frac{x_1}{x_{n+1}}\right| \quad \text{or} \quad \delta = \frac{2\pi\zeta}{\sqrt{1-\zeta^2}} \tag{5.15}$$

$$\zeta = \frac{c}{2mw_n} \tag{5.16}$$

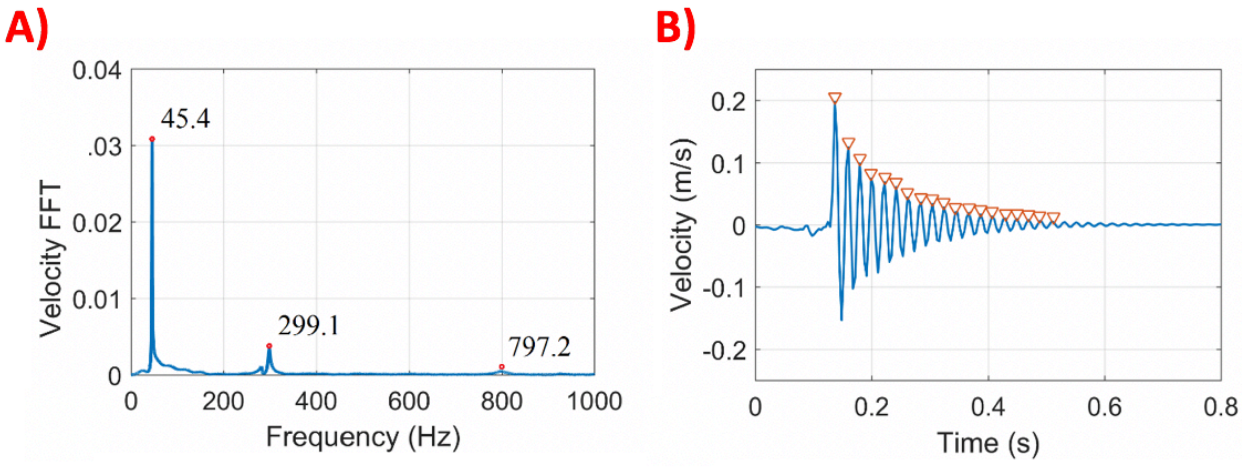

Figure 5.9- A) Velocity FFT of the beam. B) Real time velocity of the transient response of the beam.

The estimate damping ratio is 0.023 while when using the half power bandwidth method resulted in 0.026. Using this method, the estimated damping ratio and Young Modulus of the proposed beam is used for simulation.

The number of layers of Metglas® selected are 7 in the primary beam and 4 in the secondary beam to match the second resonant frequency of the harvester to 60 Hz. The two piezoelectric layers are placed such that the two layers are on the inner faces of the folded beam and that the poling directions are opposite to each other. As the poling directions are opposite and that the desired frequency of operation is the second mode, the two piezoelectric layers are connected in parallel. The length of the primary beam is 48 mm, and that of the secondary beam is 30 mm. Both the beams have a width of 15 mm. The end mass at the primary and secondary beams are 1 g and 4 g respectively, as shown in Figure 5.8A.

A plot of the power developed by the harvester as a function of load resistance at 2 mm gap for two currents 0.58 A and 0.36 A resulting in an average flux density of 5 G (500 μT) and 3 G (300 μT) as shown in Figure 5.10A. The average power developed by the harvester at 3 G and 5 G fields is measured to be 1.1 mW and 3.1 mW respectively. The power from the harvester

is observed to be maximum at 38.5 kΩ. The end displacement at the primary mass is measured to be 1.33 mm and that at the secondary mass it is 0.82 mm when the field is 5G. Figure 5.10B shows the plot of the power developed by the harvester as a function of resistance and distance. The average flux density at the harvester changes from 5 to 2.5 Gauss as the distance increased from 2 mm to 10 mm.

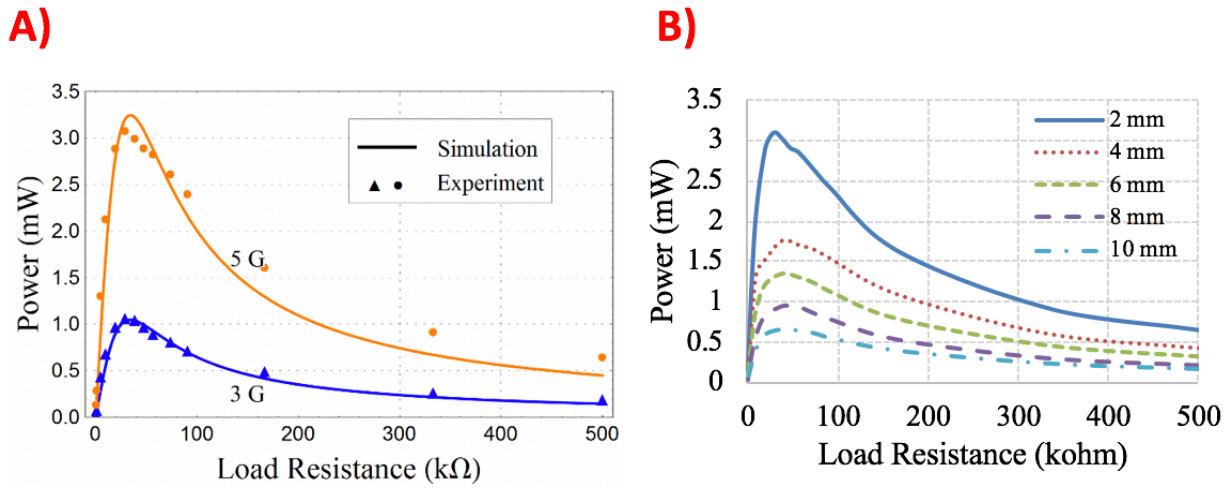

Figure 5.10- A) The power developed by the harvester as a function of load resistance at 2 mm distance from the wire for two currents resulting in an average flux density of 3 G and 5 G. B) The power developed by the harvester as a function of resistance at different gaps from the wire.

As for applications, the harvester is utilized in sending a wireless signal from a light sensor via Bluetooth. The integrated circuit LTC 3588 is used to rectify and regulate to a constant voltage required by NI sensor tag CC2650STK. The sensor is powered by the harvester placed in an average flux density of 5 G. The power developed by the harvester is sufficient to operate a light sensor present in the sensor and send the data to a mobile phone in real time. The picture of the harvester excited by a current carrying wire powering the sensor tag is shown in Figure 5.11. It can be observed that the power developed by the harvester is sufficient for the sensor to respond to the ambient light changes and communicate it with a mobile phone.

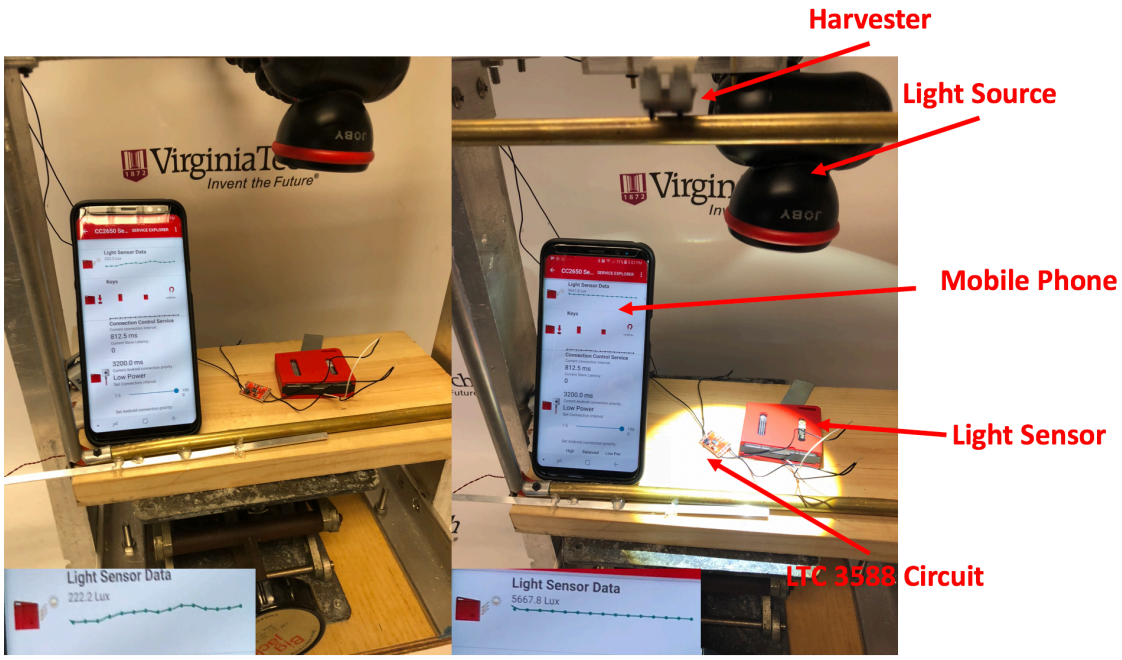

Figure 5.11- Powered generated from the harvester is used to power the sensor and send a signal a mobile phone to measure luminosity.

The power from the proposed harvester could also be utilized to charge a 350 mAh drone battery. The voltage output from the harvester is rectified and regulated before connecting the battery. The integrated circuit LTC 3588 is used to rectify and regulate the output to a constant 5 V across a 47 µF output capacitor. An N channel MOSFET is used to enable and disable the connection to the battery depending on the output capacitor voltage. This results in a trickle charging of the battery once the output capacitor reaches 5 V and disable the battery as the voltage across the capacitor drops below 5 V. The setup for charging and discharging the battery is shown in Figure 5.12A. The increase of the battery voltage with time is shown in Figure 5.12B and the drain of the drone battery across a 5 ohms resistance is shown in Figure 5.12C.

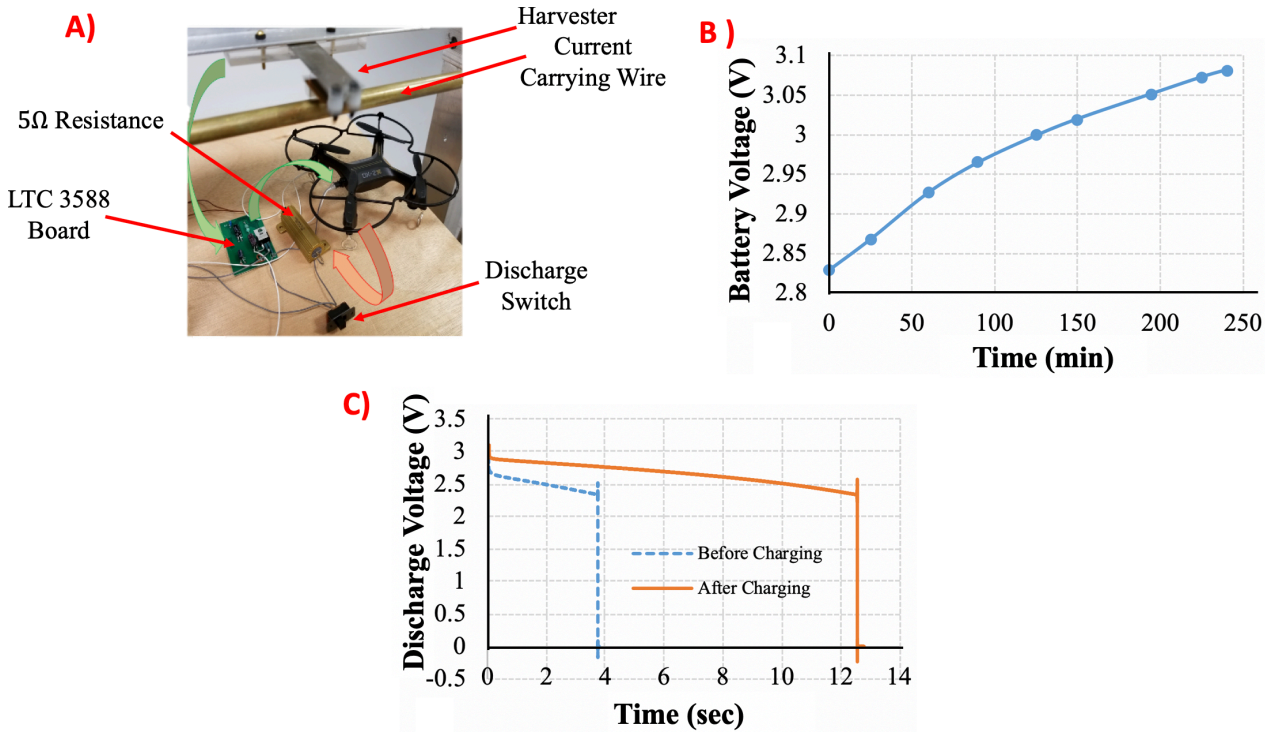

Figure 5.12- A) Setup of the drone charging station. B) Voltage across the drone voltage after four hours of charging. C) Discharging battery profile after and before the four hours of charging.

Thus, after charging the battery for four hours, the 350 mAh battery is capable of delivering 1.5 W of power for 12.5 seconds indicating 18.5 J of energy stored in the battery by the harvester. The weight of the harvester is 7.5 grams and the volume of the harvester is 1.5 cm^3. The maximum values of the power densities are 2.066 $\frac{mW}{cm^3}$, 0.413 $\frac{mW}{g}$ and 0.275 $\frac{mW}{cm^3 g}$.

Chapter 6 Conclusions and Future Work

In this dissertation, different techniques to harvest energy from a human being were developed. These energy harvesters were divided into three different categories: motion, body and surroundings.

Energy harvesters from motion are gadgets that harness energy from natural locomotion movements in the case of this dissertation a backpack and shoe sole energy harvesters were developed and tested as described in Chapter 2 and 3. A new energy harvester concept which is coined as a decoupled energy harvester was manufactured, tested and compared to traditional harvesters. In a decoupled energy harvester, the energy from human motion is first stored in a mechanical spring and then released to an electromagnetic generator. Therefore, mitigating the interaction between the wearer and the harvester.

Energy harvesters from body are devices that harness energy from a static posture and can be enhanced by motion as described in Chapter 4. A wearable thermoelectric harvester which is enhanced by arm swing motion was developed. The thermoelectric device was modeled for power generation by decreasing the number of thermoelectric materials in the system. The addition of the arm swing pendulum further increased the generation of electrical power when walking. A thermomagnetic harvester was integrated on the system to increase the electrical output in static postures. However, the thermomagnetic generated contributed little when compared to the thermoelectric and motion harvesters. Therefore, a thermomagnetic harvester was implemented at high changes in temperature in stand-alone applications.

An energy harvester from human surroundings is defined as energy harvesters that harness energy from immediate environments as shown in Chapter 5. Most of these technologies are commercially used in the renewable energy field; for example, solar panels, wind turbines,

etc. In Chapter 5, energy coming from wires electromagnetic field at 60 Hz is harvested using a two degree of freedom system. This energy harvester performed the best when close to the wire; therefore, performing better in standalone applications. A more detailed summary and future work for each of these chapters is shown in the sections below.

6.1 Chapter 2: Backpack Energy Harvesters

6.1.1 Summary

In Chapter 2, an ergonomic suspended backpack was built using lightweight devices. An energy harvester was incorporated to the suspended bag assembly according to simulations that shown that an electromagnetic system is more efficient in one direction (semi-decoupled) at inertia values of $1 * 10^{-6}$ to $0.00505\ \text{kgm}^2$ when compared to a two-way coupled harvester. For proper comparison, a decoupled energy harvester was built using the same components. Additional components, torsional storing spring assembly and disengaging pawl mechanism, were needed to decoupled the backpack harvester. The decoupled harvester consists of a torsional spring that stores energy in the downward stroke and releases the stored energy in the upward stroke. The mechanical power inflow into the decoupled system was 30% lower when compared to the semi-decoupled harvester. When walking at 4 mph while wearing a 12.8 kg suspended mass the decoupled harvester generated an average power of 1.4 W while the semi-decoupled produced 2.15 W. Moreover, the oscillation forces and relative displacement of the decoupled backpack were 52% smaller when compared to the semi-decoupled harvester. Overall the efficiency of both semi-decoupled and decoupled harvesters remained constant ~26%.

A new way to represent backpack energy harvester data is shown which incorporates the mechanical power, electrical power, walking velocity, stiffness and mass of the system. From these plots one can see that the there are three points of interest: 1) high natural frequency means

the suspended backpack behaves a locked bag, 2) low natural frequency is when isolation occurs and there is a big relative displacement but low accelerative forces and 3) when the backpack is at resonance and it experience high accelerative forces and high output power.

6.1.2 Future Work

In Section 2.7, a new way to graphically represent electrical output power and forces acting on the wearer according to the natural frequency of the system is shown. As one can see, at different walking speeds the resonance peaks of the vibrational system differ. If complete isolation wants to be achieved, the stiffness of the harvester needs to adjust according to the mass of the payload and walking speed. Ward et al. [102] showed a solution to change stiffness of a spring in prosthetic systems, however, this mechanism consumed electrical power. To implement this system, a passive controller which could engage and disengage multiple springs is theorized, as shown in Figure 6.1 and Figure 6.2.

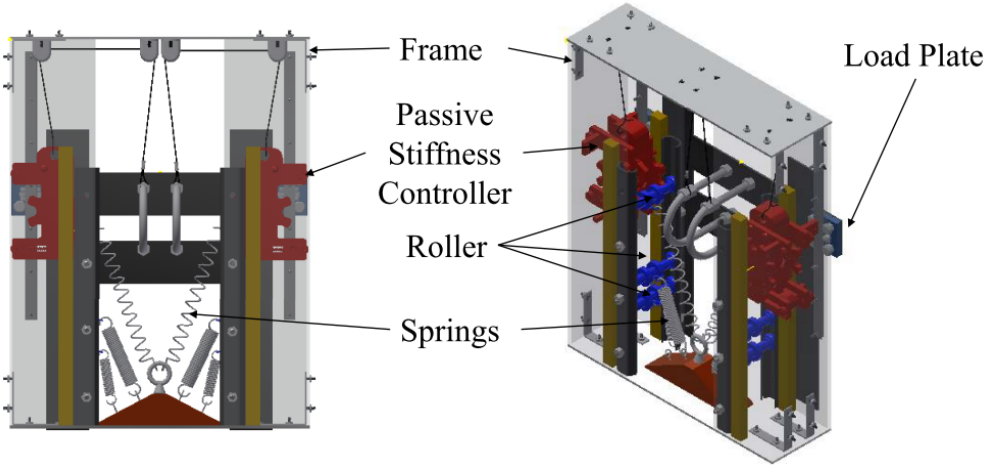

Figure 6.1- Model of main components in change of stiffness frame.

In Figure 6.1, the passive stiffness controller of the backpack is mounted onto the sides of the frames. Each roller which is connected to a spring. The number of rollers engaged or disengaged by the mechanism is shown in the flowchart in Figure 6.2.

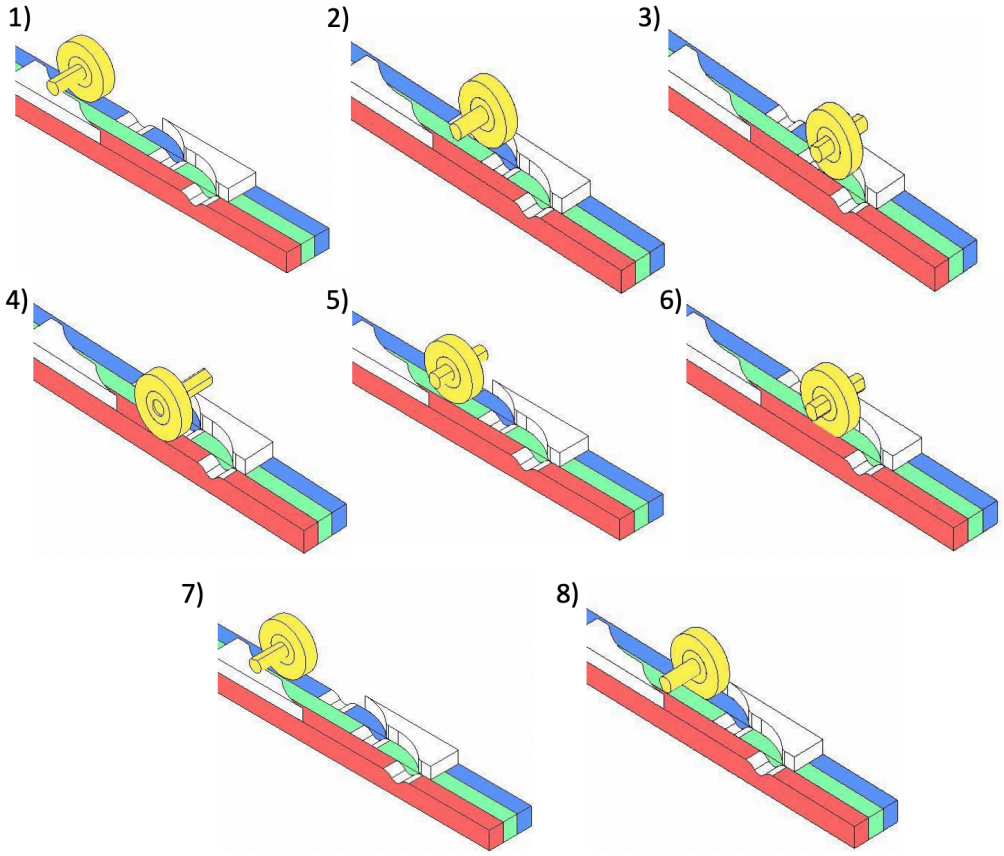

Figure 6.2- Flow chart of how the passive stiffness controller works at different gear shifters or tracks.

In Figure 6.2, (1) the passive stiffness roller oscillates attached to a spring. If the oscillation of the bag is large, the roller is pushed to the green gear (2) where is engaged to a second spring. If the oscillations remain high, the roller is pushed to the red gear (3) where is engaged to a third spring (4) and return back to the green gear (5). The movement of the gear shifter is true to high amplitude oscillations or high mass payloads. At too great stiffness the springs release at the valleys of the green gear (6), oscillates (7) and if the stiffness is still too great it releases a spring in the blue gear (8). It is important to mention that this theorized prototype was designed substantially bigger to make room for all the components. Future work

will be need to minimize the size of the components so a backpack system can passively switch between springs without the need of electrical power.

6.2 Chapter 3: Shoe Sole Energy Harvesters

6.2.1 Summary

In Chapter 3, the ankle joint is picked as an input of a decoupled harvester since at this joint maximum biomechanical power is produced. The best region to harvest power is selected and consists of the negative power region between 9 and 47 percent of the gait cycle. The decoupled mechanism is developed by using a lateral gearbox which amplifies the rotational winding of the torsional spring and a medial gearbox which increases the angular velocity of the output generator. The total extra weight of the assembly consisted of about 472.2 grams which is in the range of passive exoskeletons that reduce metabolic rate. The torsional spring stiffness was picked according to the maximum clutch bearing ratings and structure stability. A benchtop experimental test was developed for a decoupled and coupled mechanism. The total electrical output for the coupled ankle harvester increased as velocity increased from 220 to 320 miliwatts at 0.40-0.59 to 1.40-1.59 m/s. In the case of the decoupled harvester, the power generated at lower velocities was greater than the power generated at high velocities since at lower velocities the range of motion of the ankle is greater. The total power produce was 27 mW to 15 mW for 0.40-0.59 and 1.00-1.19 m/s, respectively.

6.2.2 Future Work

In section 3.6, the model predicted that a decoupled energy harvester power will rise and drop rapidly when compared to a coupled mechanism. The time where electrical power was generated was ~0.35 seconds for the three different velocities tested (Fig. 3.17). To increase the total amount of power generated overtime of the harvester. The total time where power is

generated needs to be greater than period of a walking stride. As a result, the generator in the system will conserve its angular momentum for each walking step. To increase the power over time one could: 1) decrease the electrical damping of the system by switching generators, 2) increasing the amount of turn to wind the torsional spring or 3) increasing the generators inertia with a higher gear ratio. In Figure 6.3, the mathematical model describes four different scenarios: 1) the current design, 2) ideal design with no electrical damping, 3) power spring increase in torque to 1 Nm and 4) the increase of moment of inertia by 9 times to 0.0003 kgm^2.

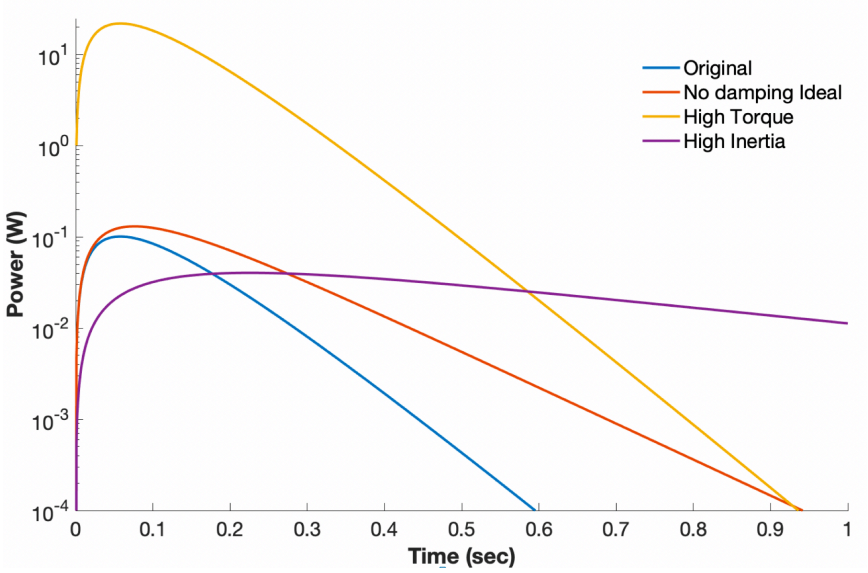

Figure 6.3- Power generated over a gait cycle assuming the average stride time of a person is 1 second. Original plot is shown in Figure 3.17 at 0.40-0.59 m/s.

As shown in Figure 6.3, in the current system time will increase if no damping and high torque is assumed; however, these changes will not be enough to keep the angular momentum of the generator above the stride period. On the other hand, by increasing inertia the total time of power generation exceeds the stride time. However, increasing the inertia of the system will increase the mass of the overall harvester since a bigger generator, gearbox or flywheel is needed. A plot of high inertia over time for 16 seconds in shown in Figure 6.4. As a result, the

medial gearbox of the energy harvester needs to increase in order to maintain the same output power while increasing the total power overtime until saturation.

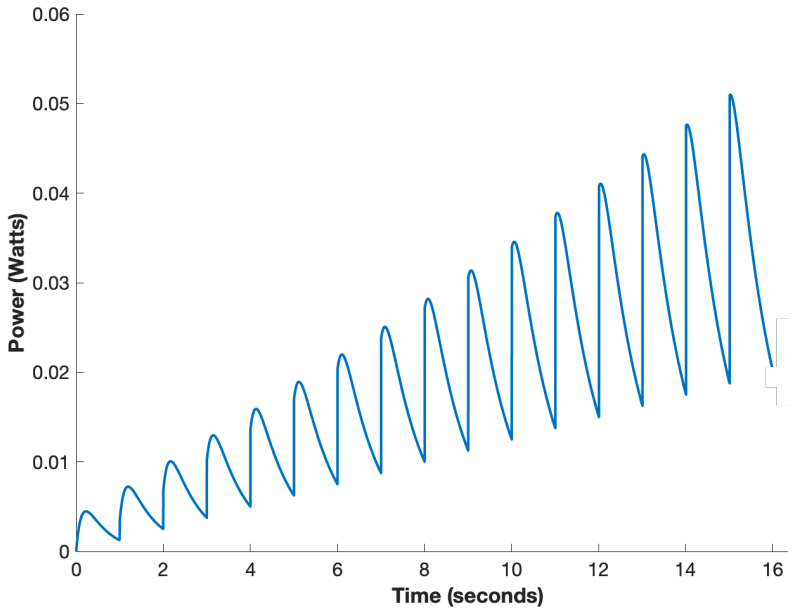

Figure 6.4- Electrical power generation over 16 seconds.

6.3 Chapter 4: Hybrid Energy Harvesters from Heat and Motion

6.3.1 Summary

In Chapter 4, a wrist energy harvester which harness energy from the change between the wrist and ambient temperature is constructed. The thermoelectric generator (TEG) is optimized by dividing the thermoelectric power variables into five different metrics: 1) heat transfer coefficient, 2) extrinsic temperature, 3) thermoelectric material characteristics, 4) nominal area of the harvester and 5) power coefficient. It is shown that a maximum power can be generated by an optimal area ratio and leg thickness. A thermomagnetic generator (TMG) is analyzed for harvesting energy from body temperature. To improve the power generated by the TMG, the harvester is incorporated with a magnetic pendulum that oscillates according to arm motion. The total average power produced by the module with the TMG and spreader was 16.5 μW. The voltage provided by the piezoelectric beam as the arm swing frequency of 2.6 Hz is 23 μW while

an average of 11.8 μW was acquired at frequencies of 1 Hz. As a result, by hybridizing an arm motion and TEG in the system the harvester can be enhanced by ~70%. However, a conventional TEG harvester with a heatsink generates around ~24.3 μW making our proposed harvester better during motion but worst during static postures.

A stand-alone TMG generator was constructed and optimize to generate high power at low frequencies and high amplitudes. The gadolinium tip mass is coated with 20 μm of silver to reduce the roughness of the material; therefore, reducing the thermal resistance of the tip mass. The maximum power achieve was around 25 mW; however, at this position average power consisted of 2 μW. In the position were maximum power was 10 mW the maximum average power occurred which value was 6 μW. A non-coated tip mass total period of oscillation was 2.98 seconds when compared to the silver coated tip mass of 1.52 second. About 100 LEDs were powered by the instantaneous oscillation of the TMG while a sensor which recorded temperature and humidity was power after 427 minutes.

6.3.2 Future Work

In Section 4.6, the power output of a thermoelectric harvester was optimized according to the area ratio between the thermoelectric material and total contact area. High power output occurred when the area ratio was around 0.035. At this small are ratios, a commercial TEG cannot be mechanically stable for a long duration. Moreover, materials ZT value of p-type and n-type thermoelectric material change in efficiency [103] at different hot side temperatures.

For these reasons a “smart thermoelectric” harvester can be created by multiple materials that are activated when a specific hot side temperature is achieved. Having multiple materials in the system will not only help create higher efficiency at different temperatures but also increase the mechanical stability of the module. Currently, cascaded thermoelectric modules shown by

Kanimba et al.[104] showed that a three stage module with different materials generated more power when compared to a two stage module; however, the amount of stages makes the complete assembly bulky and hard to manufacture. Therefore, a single stage TEG module with multiple material units that can be activated at different temperature ranges is needed for easy manufacturing, reduce volume and increase device efficiency. This could be done by using actuators that move according to the hot temperature experienced by the TEG material. In theory, these actuators would not consume power and move according to difference in temperature like a shape memory alloy. A simple proof of concept could be accomplished by manually or electrically changing the inner thermomagnetic material at each module by using an external power source, as shown in Figure 6.5. Furthermore, the thermoelectric materials would need to be selected according to the intrinsic temperature across the module. The actuation step shown in Figure 6.5, could increase thermal contact resistance while electric resistance would remain constant. On the other hand, actuation within the module would increase both thermal and electrical resistance.

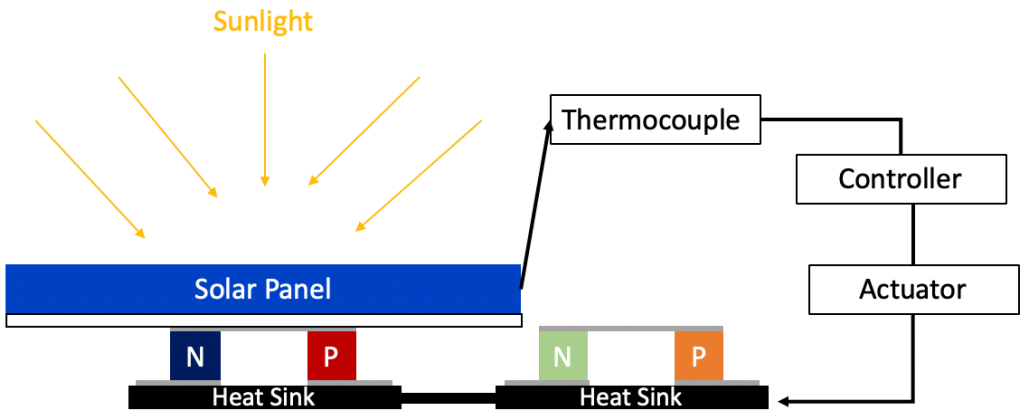

$$P_{solar} + P_{TEG} \gg P_{actuator} + P_{controller}$$

Figure 6.5- Schematic of a combination of solar cell and TEG harvester that could change thermoelectric materials at different temperature range.

6.4 Chapter 5: Electromagnetic Field Harvesters

6.4.1 Summary

In Chapter 5, a design of a magnetic field harvester in the form of a two degree of freedom system is proposed. The harvester consists of two beams constructed of laminated Metglas® and piezoelectric layers. The secondary beam tip mass consisted of a magnet while the primary beam had a nonmagnetic tip mass. The harvester is mathematically modeled to find the mass ratio and stiffness ratio where the secondary mass reach isolation at ~60 Hz. The isolation of the magnetic tip mass ensures the harvester to reach a uniform magnetic field coming from a wire. The realized harvester weights 7.5 grams and volume consists of 1.5 cm^3. The power developed by the harvester under a magnetic field of 5 Gauss is 3.1 mW when distance between wire and harvester is 2 mm. As the distance between the wire and the harvester increases the power decreases to 0.75 mW at 10 mm. For this reason, the magnetic field harvester is proposed to perform better in standalone applications and not wearable systems. The harvester is used to power a light sensor and power an UAV battery for 4 hours which is observed to gain 18.5 Joules of energy.

6.4.2 Future Work

In wearable applications harvesting energy from radio frequency is preferred by its commonality in the everyday environment. However, the energy that could be capture from radio waves is a small amount and governed by the Friss equation of transmission [105]

$$\frac{P_r}{P_t} = D_t D_r \left(\frac{\lambda}{4\pi d}\right)^2 \tag{6.1}$$

where P_t is the power transmitted, P_r power received, λ is the wave length of the signal, d is the distance between transmitter and receiver, D_r and D_t are directivity of the receiving antenna and

transmission antenna, respectively. An antenna is essential to gather RF signals then a RF to DC converter is needed to create electrical energy. In wearable applications miniaturization of antennas is needed, however, as shown in Eqn. 6.1 as the directivity decreases the received power decreases. Moreover, when bending antennas for wearable applications would change their resonance frequency and damage over time. According to Kim et al. [106], radio frequency harvesters are available to supply a voltage between 1.8-4.0 V with a maximum converted power of 100 μW which could power ultra-low sensors or extend battery life.

Since our everyday surroundings are mostly comprised on buildings (office, home, etc.) and antenna that could harvest at Wi-Fi signal of 2.4 GHz would need to be fabricated. A circular patch antenna could be picked since this could properly integrate with cloth while the circular shape is chosen to work better in different frequency environments. Dielectric constant (ϵ_r) for different substrates like jeans, cotton and felt are all given by Huang et al. [107]. While the dominant resonance frequency can be found by the equation [108]

$$f = \frac{1.8412 v_o}{2\pi a \sqrt{\epsilon_r}} \tag{6.2}$$

where v_o is the speed of light in free space and a the radius of the circular patch antenna. By using energy already spent in the environment, a capacitor could build up enough energy to power ultra-low sensors.

References

[1] J. A. Paradiso and T. Starner, "Energy scavenging for mobile and wireless electronics," *IEEE Pervasive Comput.*, vol. 4, no. 1, pp. 18–27, 2005.

[2] Thompson Phillips, *Dynamo-Electricity Machinery: A Manual for Students of Electrotechnics*, Third. Cambridge University Press, 2009.

[3] S. Priya and D. J. Inman, *Energy harvesting technologies*. Boston, MA: Springer US, 2009.

[4] H. Piggott, *The Permanent Magnet Generator (PMG): A manual for manufacturers and developers*. UK, 2001.

[5] M. Whittle, *Gait analysis : an introduction*. Butterworth-Heinemann, 1991.

[6] K. Hamill Joseph, Knutzen, *Biomechanical Basis of Human Movement*, 3rd editio. LWW, 2008.

[7] D. A. Winter, A. E. Patla, J. S. Frank, and S. E. Walt, "Biomechanical Walking Pattern Changes in the Fit and Healthy Elderly," no. 6, pp. 340–347, 2015.

[8] J. F. Patton, *Measurement of oxygen uptake with portable equipment*. Emerging Technologies for Nutrition Research: Potential for Assessing Military Performance Capability, 1997.

[9] J. M. Donelan, Q. Li, V. Naing, J. A. Hoffer, D. J. Weber, and A. D. Kuo, "Biomechanical energy harvesting: Generating electricity during walking with minimal user effort," *Science (80-.).*, vol. 319, no. 5864, pp. 807–810, 2008.

[10] R. Orr, "The history of the soldier's load," *Aust. Army J.*, vol. 7, no. 2, pp. 67–88, 2010.

[11] D. A. Winter, *Biomechanics and motor control of human movement*. John Wilet & Sons, 2009.

[12] M. S. Orendurff, A. D. Segal, G. K. Klute, J. S. Berge, E. S. Rohr, and N. J. Kadel, "The effect of walking speed on center of mass displacement," *J. Rehabil. Res. Dev.*, vol. 41, no. 6, p. 829, 2004.

[13] S. A. Gard and D. S. Childress, "What determins the vertical displacement of the body during normal walking?," *J. Prosthetics Orthot.*, vol. 13, no. 3, pp. 3–6, 2001.

[14] and T. D. Y. Rome, Lawrence C., Louis Flynn, "Rubber bands reduce the cost of carrying loads," *Nature*, vol. 444, no. 7122, p. 1023, 2006.

[15] J. Ackerman and J. Seipel, “A model of human walking energetics with an elastically-suspended load,” *J. Biomech.*, 2014.

[16] L. Xie and M. Cai, “Increased energy harvesting and reduced accelerative load for backpacks via frequency tuning,” *Mech. Syst. Signal Process.*, 2015.

[17] D. Li, T. Li, Q. Li, T. Liu, and J. Yi, “A simple model for predicting walking energetics with elastically-suspended backpack,” *J. Biomech.*, 2016.

[18] L. C. Rome, L. Flynn, E. M. Goldman, and T. D. Yoo, “Generating electricity while walking with loads.,” *Science*, vol. 309, no. September, pp. 1725–1728, 2005.

[19] Y. Yuan, M. Liu, W.-C. Tai, and L. Zuo, “Design and experimental studies of an energy harvesting backpack with mechanical motion rectification,” vol. 1016825, no. April 2017, p. 1016825, 2017.

[20] L. Xie and M. Cai, “Development of a Suspended Backpack for Harvesting Biomechanical Energy,” *J. Mech. Des.*, vol. 137, no. 5, p. 054503, 2015.

[21] J. Granstrom, J. Feenstra, H. A. Sodano, and K. Farinholt, “Energy harvesting from a backpack instrumented with piezoelectric shoulder straps,” *Smart Mater. Struct.*, vol. 16, no. 5, pp. 1810–1820, 2007.

[22] J. Feenstra, J. Granstrom, and H. Sodano, “Energy harvesting through a backpack employing a mechanically amplified piezoelectric stack,” *Mech. Syst. Signal Process.*, vol. 22, no. 3, pp. 721–734, 2008.

[23] W. Yang *et al.*, “Harvesting energy from the natural vibration of human walking,” *ACS Nano*, vol. 7, no. 12, pp. 11317–11324, 2013.

[24] C. R. Saha, T. O’Donnell, N. Wang, and P. McCloskey, “Electromagnetic generator for harvesting energy from human motion,” *Sensors Actuators, A Phys.*, vol. 147, no. 1, pp. 248–253, 2008.

[25] D. A. Winter and H. J. Yack, “EMG profiles during normal human walking: stride-to-stride and inter-subject variability,” *Electroencephalogr. Clin. Neurophysiol.*, vol. 67, no. 5, pp. 402–411, 1987.

[26] F. Danion, E. Varraine, M. Bonnard, and J. Pailhous, “Stride variability in human gait: The effect of stride frequency and stride length,” *Gait Posture*, vol. 18, no. 1, pp. 69–77, 2003.

[27] Z. A. Cavagna GA, Thys H, “The sources of external work in level walking and running,” *J. Physiol.*, vol. 262, no. 3, pp. 639–657, 1976.

[28] S. Kajita, F. Kanehiro, K. Kaneko, K. Yokoi, and H. Hirukawa, “The 3D linear inverted pendulum mode: a simple modeling for a biped walking pattern generation,” *Proc. 2001 IEEE/RSJ Int. Conf. Intell. Robot. Syst. Expand. Soc. Role Robot. Next Millenn. (Cat. No.01CH37180)*, vol. 1, pp. 239–246, 2001.

[29] P. G. Adamczyk, S. H. Collins, and A. D. Kuo, “The advantages of a rolling foot in human walking,” *J. Exp. Biol.*, vol. 209, no. 20, pp. 3953–3963, 2006.

[30] B. R. Whittington and D. G. Thelen, “A Simple Mass-Spring Model With Roller Feet Can Induce the Ground Reactions Observed in Human Walking,” *J. Biomech. Eng.*, vol. 131, no. 1, p. 011013, 2009.

[31] D. Inman, *Engineering Vibration*, 4th Editio. Pearson Education, 2014.

[32] S. J. Chapman, *Electric Machinery Fundamentals*. McGraw Hill, 2012.

[33] Y.-M. Choi, M. Lee, Y. Jeon, Y.-M. Choi, M. G. Lee, and Y. Jeon, “Wearable Biomechanical Energy Harvesting Technologies,” *Energies*, vol. 10, no. 10, p. 1483, Sep. 2017.

[34] B. I. Prilutsky, L. N. Petrova, and L. M. Raitsin, “Comparison of mechanical energy expenditure of joint moments and muscle forces during human locomotion,” *J. Biomech.*, vol. 29, no. 4, pp. 405–415, Apr. 1996.

[35] S. H. Collins, M. B. Wiggin, and G. S. Sawicki, “Reducing the energy cost of human walking using an unpowered exoskeleton,” *Nature*, vol. 522, no. 7555, pp. 212–215, 2015.

[36] A. B. Zoss, H. Kazerooni, and A. Chu, “Biomechanical design of the Berkeley lower extremity exoskeleton (BLEEX),” *IEEE/ASME Trans. Mechatronics*, vol. 11, no. 2, pp. 128–138, Apr. 2006.

[37] C. J. WALSH, K. ENDO, and H. HERR, “A QUASI-PASSIVE LEG EXOSKELETON FOR LOAD-CARRYING AUGMENTATION,” *Int. J. Humanoid Robot.*, vol. 04, no. 03, pp. 487–506, Sep. 2007.

[38] N. S. Shenck and J. A. Paradiso, “Energy scavenging with shoe-mounted piezoelectrics,” *IEEE Micro*, vol. 21, no. 3, pp. 30–42, 2001.

[39] C. A. Howells, “Piezoelectric energy harvesting,” *Energy Convers. Manag.*, vol. 50, no. 7, pp. 1847–1850, Jul. 2009.

[40] J. G. Rocha, L. M. Goncalves, P. F. Rocha, M. P. Silva, and S. Lanceros-Mendez, “Energy Harvesting From Piezoelectric Materials Fully Integrated in Footwear,” *IEEE Trans. Ind. Electron.*, vol. 57, no. 3, pp. 813–819, Mar. 2010.

[41] J. Zhao, Z. You, J. Zhao, and Z. You, “A Shoe-Embedded Piezoelectric Energy Harvester for Wearable Sensors,” *Sensors*, vol. 14, no. 7, pp. 12497–12510, Jul. 2014.

[42] W.-S. Jung *et al.*, “Powerful curved piezoelectric generator for wearable applications,” *Nano Energy*, vol. 13, pp. 174–181, Apr. 2015.

[43] K. Fan, Z. Liu, H. Liu, L. Wang, Y. Zhu, and B. Yu, “Scavenging energy from human walking through a shoe-mounted piezoelectric harvester,” *Appl. Phys. Lett.*, vol. 110, no. 14, p. 143902, Apr. 2017.

[44] T.-C. Hou, Y. Yang, H. Zhang, J. Chen, L.-J. Chen, and Z. Lin Wang, “Triboelectric nanogenerator built inside shoe insole for harvesting walking energy,” *Nano Energy*, vol. 2, no. 5, pp. 856–862, Sep. 2013.

[45] G. Zhu, P. Bai, J. Chen, and Z. Lin Wang, “Power-generating shoe insole based on triboelectric nanogenerators for self-powered consumer electronics,” *Nano Energy*, vol. 2, no. 5, pp. 688–692, Sep. 2013.

[46] T. Huang, C. Wang, H. Yu, H. Wang, Q. Zhang, and M. Zhu, “Human walking-driven wearable all-fiber triboelectric nanogenerator containing electrospun polyvinylidene fluoride piezoelectric nanofibers,” *Nano Energy*, vol. 14, pp. 226–235, May 2015.

[47] X. Cheng, B. Meng, X. Zhang, M. Han, Z. Su, and H. Zhang, “Wearable electrode-free triboelectric generator for harvesting biomechanical energy,” *Nano Energy*, vol. 12, pp. 19–25, Mar. 2015.

[48] K. Zhang, X. Wang, Y. Yang, and Z. L. Wang, “Hybridized Electromagnetic–Triboelectric Nanogenerator for Scavenging Biomechanical Energy for Sustainably Powering Wearable Electronics,” *ACS Nano*, vol. 9, no. 4, pp. 3521–3529, Apr. 2015.

[49] R. I. Haque, P.-A. Farine, and D. Briand, “Fully casted soft power generating triboelectric shoe insole,” *J. Phys. Conf. Ser.*, vol. 773, no. 1, p. 012097, Nov. 2016.

[50] P. Bai *et al.*, “Integrated Multilayered Triboelectric Nanogenerator for Harvesting Biomechanical Energy from Human Motions,” *ACS Nano*, vol. 7, no. 4, pp. 3713–3719, Apr. 2013.

[51] L. Xie and M. Cai, “An In-Shoe Harvester With Motion Magnification for Scavenging Energy From Human Foot Strike,” *IEEE/ASME Trans. Mechatronics*, vol. 20, no. 6, pp. 3264–3268, Dec. 2015.

[52] M. Pozzi and M. Zhu, “Characterization of a rotary piezoelectric energy harvester based on plucking excitation for knee-joint wearable applications,” *Smart Mater. Struct.*, vol. 21, no. 5, p. 055004, May 2012.

[53] Y. Kuang, Z. Yang, and M. Zhu, “Design and characterisation of a piezoelectric knee-joint energy harvester with frequency up-conversion through magnetic plucking,” *Smart Mater. Struct.*, vol. 25, no. 8, p. 085029, Aug. 2016.

[54] Y. Rao, S. Cheng, and D. P. Arnold, “An energy harvesting system for passively generating power from human activities,” *J. Micromechanics Microengineering*, vol. 23, no. 11, p. 114012, Nov. 2013.

[55] K. Ylli, D. Hoffmann, A. Willmann, P. Becker, B. Folkmer, and Y. Manoli, “Energy harvesting from human motion: exploiting swing and shock excitations,” *Smart Mater. Struct.*, vol. 24, no. 2, p. 025029, Feb. 2015.

[56] S. Wu, P. C. K. Luk, C. Li, X. Zhao, Z. Jiao, and Y. Shang, “An electromagnetic wearable 3-DoF resonance human body motion energy harvester using ferrofluid as a lubricant,” *Appl. Energy*, vol. 197, pp. 364–374, Jul. 2017.

[57] M. Duffy and D. Carroll, “Electromagnetic generators for power harvesting,” in *2004 IEEE 35th Annual Power Electronics Specialists Conference (IEEE Cat. No.04CH37551)*, pp. 2075–2081.

[58] B. F. Mentiplay, M. Banky, R. A. Clark, M. B. Kahn, and G. Williams, “Lower limb angular velocity during walking at various speeds,” *Gait Posture*, vol. 65, pp. 190–196, Sep. 2018.

[59] T. A. Mcmahon and P. R. Greene, “Fast Running Tracks,” vol. 239, no. 6, pp. 148–163, 1978.

[60] A. E. Kerdok, A. A. Biewener, T. A. McMahon, P. G. Weyand, and H. M. Herr, “Energetics and mechanics of human running on surfaces of different stiffnesses,” *J. Appl. Physiol.*, vol. 92, no. 2, pp. 469–478, Feb. 2002.

[61] T. Ji, “Frequency and velocity of people walking Elasticity of structures using analytical, semi-analytical and numerical methods View project,” 2005.

[62] C. L. Peterson, S. A. Kautz, and R. R. Neptune, “Braking and propulsive impulses increase with speed during accelerated and decelerated walking,” *Gait Posture*, vol. 33, no. 4, pp. 562–567, Apr. 2011.

[63] G. Bovi, M. Rabuffetti, P. Mazzoleni, and M. Ferrarin, “A multiple-task gait analysis approach: Kinematic, kinetic and EMG reference data for healthy young and adult subjects,” *Gait Posture*, vol. 33, no. 1, pp. 6–13, Jan. 2011.

[64] M. Liu *et al.*, “Design, simulation and experiment of a novel high efficiency energy harvesting paver,” *Appl. Energy*, vol. 212, pp. 966–975, Feb. 2018.

[65] G. J. Snyder, “Thermoelectric Energy Harvesting,” in *Energy Harvesting Technologies*, S. Priya and D. J. Inman, Eds. Boston, MA: Springer US, 2009, pp. 325–336.

[66] F. J. DiSalvo, “Thermoelectric cooling and power generation,” *Science*, vol. 285, no. 5428, pp. 703–6, Jul. 1999.

[67] S. N. Khatami and Z. Aksamija, “Lattice Thermal Conductivity of the Binary and Ternary Group-IV Alloys Si-Sn, Ge-Sn, and Si-Ge-Sn,” *Phys. Rev. Appl.*, vol. 6, no. 1, p. 014015, Jul. 2016.

[68] J. Kitahara, “Development of small AGS (automatic power-generator for wrist watch,” *Horol Inst Jpn*, 1996.

[69] H. G. Yeo, T. Xue, S. Roundy, X. Ma, C. Rahn, and S. Trolier-McKinstry, “Strongly (001) Oriented Bimorph PZT Film on Metal Foils Grown by rf-Sputtering for Wrist-Worn Piezoelectric Energy Harvesters,” *Adv. Funct. Mater.*, vol. 28, no. 36, pp. 1–9, 2018.

[70] M. A. Halim, H. Cho, and J. Y. Park, “Design and experiment of a human-limb driven, frequency up-converted electromagnetic energy harvester,” *Energy Convers. Manag.*, vol. 106, pp. 393–404, Dec. 2015.

[71] R. A. Kishore *et al.*, “Energy scavenging from ultra-low temperature gradients †,” | *Energy Environ. Sci*, vol. 12, p. 1008, 2019.

[72] J. Chun, H.-C. Song, M.-G. Kang, H. B. Kang, R. A. Kishore, and S. Priya, “Thermo-magneto-electric generator arrays for active heat recovery system,” *Sci. Rep.*, vol. 7, p. 41383, 2017.

[73] J. Chun *et al.*, “Self-Powered Temperature-Mapping Sensors Based on Thermo-Magneto-Electric Generator,” *ACS Appl. Mater. Interfaces*, vol. 10, no. 13, pp. 10796–10803, 2018.

[74] Chin-Chung Chen, Tien-Kan Chung, Chia-Yuan Tseng, Chiao-Fang Hung, Po-Chen Yeh, and Chih-Cheng Cheng, “A Miniature Magnetic-Piezoelectric Thermal Energy Harvester,” *IEEE Trans. Magn.*, vol. 51, no. 7, pp. 1–9, Jul. 2015.

[75] H. E. Nigh, S. Legvold, and F. H. Spedding, “Magnetization and Electrical Resistivity of Gadolinium Single Crystals,” *Phys. Rev.*, vol. 132, no. 3, pp. 1092–1097, Nov. 1963.

[76] W. M. Haynes, *CRC Handbook of Chemistry and Physics, 95th Edition*. CRC Press, 2014.

[77] “Periodic Table of Elements: Los Alamos National Laboratory.” [Online]. Available: https://periodic.lanl.gov/64.shtml. [Accessed: 10-Sep-2018].

[78] R. A. Freitas, *Nanomedicine, volume I: basic capabilities*. 1999.

[79] J. Park, “Synthesis of natural arm swing motion in human bipedal walking,” *J. Biomech.*, vol. 41, no. 7, pp. 1417–1426, Jan. 2008.

[80] R. C. Wagenaar and R. E. . van Emmerik, “Resonant frequencies of arms and legs identify different walking patterns,” *J. Biomech.*, vol. 33, no. 7, pp. 853–861, Jul. 2000.

[81] S. F. Donker, P. J. Beek, R. C. Wagenaar, and T. Mulder, “Coordination Between Arm and Leg Movements During Locomotion,” *J. Mot. Behav.*, vol. 33, no. 1, pp. 86–102, Mar. 2001.

[82] M. P. Ford, R. C. Wagenaar, and K. M. Newell, “Arm constraint and walking in healthy adults,” *Gait Posture*, vol. 26, no. 1, pp. 135–141, Jun. 2007.

[83] M. Hyland, H. Hunter, J. Liu, E. Veety, and D. Vashaee, “Wearable thermoelectric generators for human body heat harvesting,” *Appl. Energy*, vol. 182, pp. 518–524, 2016.

[84] S. Lineykin and S. Ben-Yaakov, “Modeling and Analysis of Thermoelectric Modules,” *IEEE Trans. Ind. Appl.*, vol. 43, no. 2, pp. 505–512, 2007.

[85] S. Kim, “Analysis and modeling of effective temperature differences and electrical parameters of thermoelectric generators,” *Appl. Energy*, vol. 102, pp. 1458–1463, 2013.

[86] T. L. Bergman and F. P. Incropera, *Fundamentals of heat and mass transfer.* Wiley, 2011.

[87] K. B. Joshi and S. Priya, “Multi-physics model of a thermo-magnetic energy harvester,” *Smart Mater. Struct.*, vol. 22, no. 5, p. 55005, 2013.

[88] M. G. Cooper, B. B. Mikic, and M. M. Yovanovich, “Thermal contact conductance,” *Int. J. Heat Mass Transf.*, vol. 12, no. 3, pp. 279–300, Mar. 1969.

[89] H. Yüncü, “Thermal contact conductance of nominaly flat surfaces,” *Heat Mass Transf.*, vol. 43, no. 1, pp. 1–5, Sep. 2006.

[90] M. N. O. Sadiku, “Elements of electromagnetics,” Jan. 2014.

[91] S. Yuan, Y. Huang, J. Zhou, Q. Xu, C. Song, and P. Thompson, “Magnetic Field Energy Harvesting Under Overhead Power Lines,” *IEEE Trans. Power Electron.*, vol. 30, no. 11, pp. 6191–6202, Nov. 2015.

[92] F. Guo, H. Hayat, and J. Wang, “Energy harvesting devices for high voltage transmission line monitoring,” in *2011 IEEE Power and Energy Society General Meeting*, 2011, pp. 1–8.

[93] M. J. Moser, T. Bretterklieber, H. Zangl, and G. Brasseur, “Strong and Weak Electric Field Interfering: Capacitive Icing Detection and Capacitive Energy Harvesting on a 220-kV High-Voltage Overhead Power Line,” *IEEE Trans. Ind. Electron.*, vol. 58, no. 7, pp. 2597–2604, Jul. 2011.

[94] V. Annapureddy *et al.*, “Exceeding milli-watt powering magneto-mechano-electric generator for standalone-powered electronics,” *Energy Environ. Sci.*, vol. 11, no. 4, pp. 818–829, Apr. 2018.

[95] J. Ryu, S. Priya, K. Uchino, and H.-E. Kim, “Magnetoelectric Effect in Composites of Magnetostrictive and Piezoelectric Materials,” *J. Electroceramics*, vol. 8, no. 2, pp. 107–119, 2002.

[96] Z. Xing, K. Xu, G. Dai, J. Li, and D. Viehland, “Giant magnetoelectric torque effect and multicoupling in two phases ferromagnetic/piezoelectric system,” *J. Appl. Phys.*, vol. 110, no. 10, p. 104510, Nov. 2011.

[97] M. G. Kang *et al.*, “High Power Magnetic Field Energy Harvesting through Amplified Magneto-Mechanical Vibration,” *Adv. Energy Mater.*, vol. 8, no. 16, p. 1703313, Jun. 2018.

[98] H.-C. Song *et al.*, “Broadband dual phase energy harvester: Vibration and magnetic field,” *Appl. Energy*, vol. 225, pp. 1132–1142, Sep. 2018.

[99] J.-T. Lin, B. Lee, and B. Alphenaar, “The magnetic coupling of a piezoelectric cantilever for enhanced energy harvesting efficiency,” *Smart Mater. Struct.*, vol. 19, no. 4, p. 045012, Apr. 2010.

[100] J. Institution of Electrical Engineers., *IEE proceedings. Generation, transmission, and distribution.*, vol. 142, no. 5. Institution of Electrical Engineers, 1994.

[101] L. Meirovitch and R. Parker, “Fundamentals of Vibrations,” *Appl. Mech. Rev.*, vol. 54, no. 6, p. B100, 2001.

[102] J. A. Ward, T. G. Sugar, and K. W. Hollander, “Using the translational potential energy of springs for prosthetic systems,” in *2011 IEEE International Conference on Control Applications (CCA)*, 2011, pp. 1461–1467.

[103] G. J. SNYDER and E. S. TOBERER, “Complex thermoelectric materials,” in *Materials for Sustainable Energy*, Co-Published with Macmillan Publishers Ltd, UK, 2010, pp. 101–110.

[104] E. Kanimba, M. Pearson, J. Sharp, D. Stokes, S. Priya, and Z. Tian, “A modeling comparison between a two-stage and three-stage cascaded thermoelectric generator,” *J. Power Sources*, vol. 365, pp. 266–272, Oct. 2017.

[105] Friis and H. T., “A Note on a Simple Transmission Formula,” *Proc. IRE*, vol. 34, no. 5, pp. 254–256, 1946.

[106] S. Kim *et al.*, “Ambient RF Energy-Harvesting Technologies for Self-Sustainable Standalone Wireless Sensor Platforms,” *Proc. IEEE*, vol. 102, no. 11, pp. 1649–1666, Nov. 2014.

[107] H. Huang and J. Skilskyj, “Flexible textile antenna sensor for bio-impedance sensing,” in *Sensors and Smart Structures Technologies for Civil, Mechanical, and Aerospace Systems 2019*, 2019, vol. 10970, p. 47.

[108] C. A. Balanis, *Antenna theory : analysis and design*. .

[109] S. Kumar. "Energy Scavenging During Human Walk". https://www.researchgate.net/profile/Sampath_Kumar30/publication/269702564_Energy_Scavenging_During_Human_Walk/links/5493d9300cf286fe31269862/Energy-Scavenging-During-Human-Walk.pdf

[110] A. Dollar and H. Herr. "Design of a quasi-passive knee exoskeleton to assist running." *2008 IEEE/RSJ international conference on intelligent robots and systems. IEEE*, 2008.

Appendix A: Polynomial Fit

```
%data points of ankle motion at steps of gait%
x_t =
[0;1;2;3;4;5;6;7;8;9;10;11;12;13;14;15;16;17;18;19;20;21;22;23;24;25;26;27;28
;29;30;31;32;33;34;35;36;37;38;39;40;41;42;43;44;45;46;47;48;49;50;51;52;53;5
4;55;56;57;58;59;60;61;62;63;64;65;66;67;68;69;70;71;72;73;74;75;76;77;78;79;
80;81;82;83;84;85;86;87;88;89;90;91;92;93;94;95;96;97;98;99;100];
y = [0;-0.477516174000000;-1.67968940700000;-3.21852111800000;-
4.25665473900000;-4.32913208000000;-3.62319755600000;-2.62982368500000;-
1.67413330100000;-
0.782287598000000;0.099435806000000;0.985685349000000;1.81409645100000;2.584
29336500000;3.31120872500000;3.98331451400000;4.61959266700000;5.213222504000
00;5.77194023100000;6.29441070600000;6.79639625500000;7.27902221700000;7.7605
7243300000;8.23798179600000;8.69186782800000;9.12119865400000;9.5155887600000
0;9.88392543800000;10.2285594900000;10.5462093400000;10.8406620000000;11.1411
857600000;11.4765014600000;11.8606462500000;12.2823181200000;12.7146034200000
;13.1237354300000;13.4920578000000;13.8195209500000;14.1023654900000;14.32752
60900000;14.4741735500000;14.5343284600000;14.5050144200000;14.3775663400000;
14.1387891800000;13.7616872800000;13.2047290800000;12.4308853100000;11.412815
0900000;10.1286897700000;8.51304435700000;6.52905845600000;4.10196113600000;1
.16627121000000;-2.26999473600000;-6.08051872300000;-9.97717094400000;-
13.5947132100000;-16.6714496600000;-19.1012020100000;-20.8801937100000;-
22.0682392100000;-22.6782054900000;-22.6688785600000;-21.8532199900000;-
20.1714305900000;-17.9343395200000;-15.5002880100000;-13.1852321600000;-
11.0664653800000;-9.12475395200000;-7.32392692600000;-5.55950546300000;-
3.84651374800000;-2.26599884000000;-
0.941041946000000;0.140890121000000;1.02303314200000;1.80273628200000;2.51902
580300000;3.17118835400000;3.76238060000000;4.23303985600000;4.55422782900000
;4.65722656200000;4.48135185200000;4.03348350500000;3.40388870200000;2.738933
56300000;2.13771629300000;1.59101867700000;1.09743309000000;0.647609711000000
;0.260635376000000;-0.0492153170000000;-0.270986557000000;-
0.388059616000000;-0.359869003000000;-0.186174393000000;-0.0529327390000000];


p = polyfit(x_t,y,22);
y1 = polyval(p,x_t);
plot(x_t,y)

hold on

plot(x_t,y1)
legend('Bovi et al','polynomial fit');


%%torque data points at steps of gait %
tor= [
-0.06
-0.07
-0.08
-0.09
-0.10
-0.10
-0.10
-0.09
-0.08
```

-0.07
-0.05
-0.03
-0.01
0.02
0.04
0.06
0.09
0.11
0.14
0.17
0.19
0.22
0.25
0.28
0.31
0.35
0.38
0.42
0.46
0.50
0.54
0.59
0.64
0.69
0.74
0.79
0.84
0.89
0.94
0.99
1.04
1.08
1.12
1.15
1.18
1.19
1.19
1.18
1.15
1.09
1.03
0.94
0.85
0.75
0.64
0.53
0.43
0.33
0.25
0.18
0.12
0.07
0.04
0.02
0.00
-0.01
-0.01

```
-0.01
-0.01
-0.01
-0.01
-0.01
-0.01
-0.01
-0.01
-0.01
-0.01
-0.01
-0.01
-0.01
-0.01
-0.01
-0.01
-0.01
-0.01
-0.01
-0.01
-0.01
-0.01
-0.01
-0.01
-0.01
-0.01
-0.01
0.00
0.00
0.00
-0.01
-0.01
-0.01];

p1 = polyfit(x_t,tor,22);
ytor = polyval(p1,x_t);
plot(x_t,tor)
hold on
plot(x_t,ytor)

legend('Bovi et al','polynomial fit');

%% find velocity

syms x

 f= (8.71894967772862e-33)*x^22+ ...
 (-9.01237738579973e-30)*x^21+ ...
 (4.30759477309193e-27)*x^20+ ...
 (-1.26264810080068e-24)*x^19+ ...
 (2.53804294979286e-22)*x^18+ ...
 (-3.70564405979038e-20)*x^17+ ...
 (4.05989414283323e-18)*x^16+ ...
 (-3.39904921066655e-16)*x^15+ ...
 (2.19253209280677e-14)*x^14+ ...
 (-1.08899761795044e-12)*x^13+ ...
```

```
 (4.12003873159121e-11)*x^12+ ...
 (-1.15490344366198e-09)*x^11+ ...
 (2.23909582448491e-08)*x^10+ ...
 (-2.34675876145930e-07)*x^9+ ...
 (-1.25236789117331e-06)*x^8+ ...
 (0.000100893328120719)*x^7+ ...
 (-0.00205582641706947)*x^6+ ...
 (0.0251656769975928)*x^5+ ...
 (-0.202537302377298)*x^4+ ...
 (1.03390817501017)*x^3+ ...
 (-2.76085522344150)*x^2+ ...
 (1.74004707990296)*x^1+ ...
 -0.0632265760749274;

a= diff(f)
%% velocity eqn

z =
(70085175763933693*x2.^21)/365375409332725729550921208179070754913983135744 -
...
(67530197855809689*x2.^20)/356811923176489970264571492362373784095686656 ...
+ (15009777102069605*x2.^19)/17422457186352049329324779900506532426547 2 ...
- (130615692835919651*x2.^18)/5444517870735015415413993718908291383296 ...
+ (48580383504516471*x2.^17)/106338239662793269832304564822427566 08 ...
- (104669973817108219*x2.^16)/166153499473114484112975882535043072 ...
+ (658755487619279*x2.^15)/10141204801825835211973625643008 ...
- (51705681265280895*x2.^14)/101412048018258352119736256430 08 ...
+ (48638880910657765*x2.^13)/158456325028528675187087900672 ...
- (70101915205257169*x2.^12)/49517601571415210995964968 96 ...
+ (19126353409662417*x2.^11)/38685626227668133590597632 ...
- (15358118514252987*x2.^10)/12089258196146291747061 76 ...
+ (4229532429392365*x2.^9)/18889465931478580854784 -
(79792235413171767*x2.^8)/3777893186295716170956 8 -
(5914140153498979*x2.^7)/590295810358705651712 +
(26056147636227891*x2.^6)/36893488147419103232 -
(14221238915869419*x2.^5)/1152921504606846976 +
(36267562735643265*x2.^4)/288230376151711744 -
(36485876780600 99*x2.^3)/4503599627370496 +
(13968925415133333*x2.^2)/4503599627370496 -
(6216893277757513*x2)/1125899906842624 + 3918237690329045/2251799813685248;

%% torq  eqn
torq2 = (-3.48595889041616e-34)*x2.^22 + ...
 (3.82026859542531e-31)*x2.^21 + ...
 (-1.94704761711049e-28)*x2.^20 + ...
 (6.12667292821899e-26)*x2.^19 + ...
 (-1.33259556187112e-23)*x2.^18 + ...
 (2.12565587698125e-21)*x2.^17 + ...
 (-2.57467886877804e-19)*x2.^16 + ...
 (2.41923901574977e-17)*x2.^15 + ...
 (-1.78639804611410e-15)*x2.^14 + ...
 (1.04388320279798e-13)*x2.^13 + ...
 (-4.83847122111891e-12)*x2.^12 + ...
 (1.77584289852288e-10)*x2.^11 + ...
 (-5.13237481085589e-09)*x2.^10 + ...
 (1.15676409842675e-07)*x2.^9 + ...
 (-2.00403771943446e-06)*x2.^8 + ...
 (2.61462187534707e-05)*x2.^7 + ...
```

```
(-0.000249654762213131)*x2.^6 + ...
(0.00167626220983511)*x2.^5 + ...
(-0.00748340769596308)*x2.^4 + ...
(0.0205244117320564)*x2.^3 + ...
(-0.0290143305716902)*x2.^2 + ...
(0.00318282065775520)*x2.^1 + ...
-0.0590194798510842;
```